SIEMENS

MAGNETOM Flash

The Magazine of MRI

Issue Number 2/2014 | SPR Edition

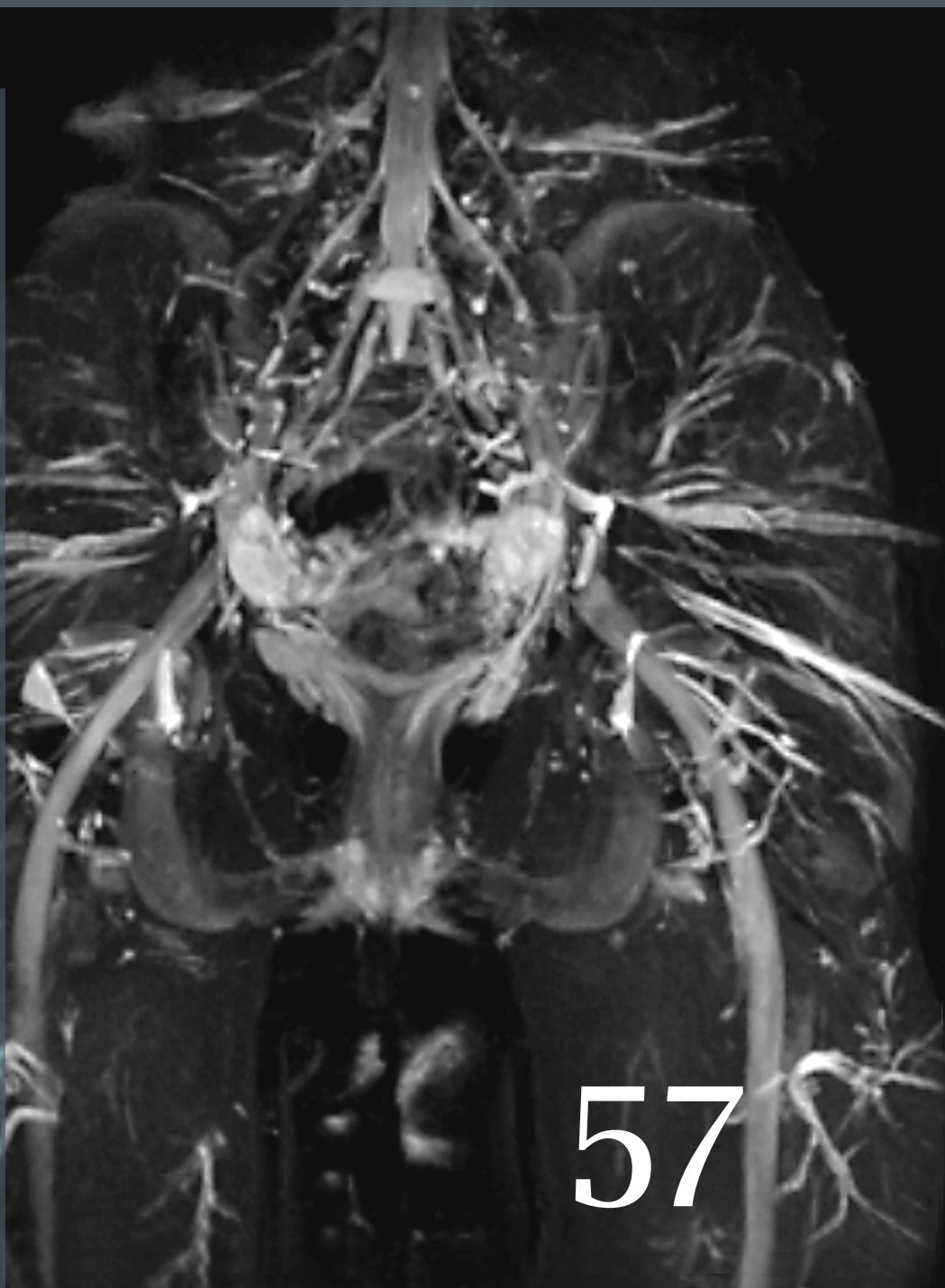

57

Editorial

Professor Michael Ditchfield is the Head of Paediatric Imaging at Monash Medical Centre and the Professor of Paediatric Imaging at Monash University (Clayton, Australia), has a conjoint appointment at the Monash Institute of Medical Research and is an Honorary Research Fellow at the Murdoch and Children's Research Institute (Melbourne, Australia). He has worked as a pediatric radiologist for 20 years and has subspecialty pediatric interests in MRI, cardiothoracic, neonatal and urinary imaging and has a strong commitment to teaching and research.

"Technological advancement has expanded the role of MRI in pediatrics from being predominantly a brain imaging technology to being a comprehensive multi-organ modality."

Professor Michael Ditchfield

Dear MAGNETOM Flash reader,

Children are intrinsically difficult to image. Their organs are small creating a high demand on spatial resolution. They have rapid heart and respiratory rates making thoracic and abdominal imaging even more challenging than in adults. In addition, they often have a very limited capacity to cooperate and the environment of the MRI unit adds to the difficulty of obtaining diagnostic images. Nevertheless, MRI provides excellent contrast resolution and does not use ionizing radiation making it a very valuable imaging tool in children*.

MRI has undergone a major revolution over recent years with higher field strength, sequences that overcome SAR issues, parallel imaging, sequences that suppress motion artifact, 3 dimensional imaging and improved coil technology combining to overcome many of these hurdles. This has enabled faster and higher resolution imaging and enabled many of the new and novel MRI applications showcased in this edition of MAGNETOM Flash.

These technological advances have developed in parallel with a better appreciation of the needs of children and how to improve their capacity to cooperate to avoid the need for general anesthesia. The recognition of the need for specialist staff to familiarize children with the procedure, the importance of information appropriate to the development of the child (picture books, MRI toys, videos and Mock MRI units) and the use of distraction with MRI compatible videos and music have expanded the availability of MRI in pediatrics. These techniques when compared to general anesthesia or deep sedation are safe and relatively inexpensive. In many centers general anesthesia or deep sedation was routinely used for most children. Embracing these techniques has expanded the use of MRI to children as young as 3 years without anesthesia.

The combination of these techniques and technological advancement has expanded the role of MRI in pediatrics from being predominantly a brain imaging technology to being a comprehensive multi-organ modality. In pediatrics it is now routinely used in thoracic, cardiac, abdominal, musculoskeletal and total body imaging. Techniques such as DWI and tractography and neurography are improving our understanding of pediatric disease processes both in and outside the brain. Safe high resolution and fast MRI techniques are creating the reality of fetal cardiac MRI. In the last 10 years there has been a revolution in the application of MRI in pediatrics, there is no reason why the next 10 years should be any different.

This issue of MAGNETOM Flash showcases many of these exciting new techniques from renowned experts and demonstrates how they have been applied both to clinical pediatric imaging and in research.

*Siemens disclaimer: MR scanning has not been established as safe for imaging fetuses and infants less than two years of age. The responsible physician must evaluate the benefits of the MR examination compared to those of other imaging procedures. This disclaimer does not represent the view of the the guest editor of this issue. It is solely for regulatory reasons.

Content

Content

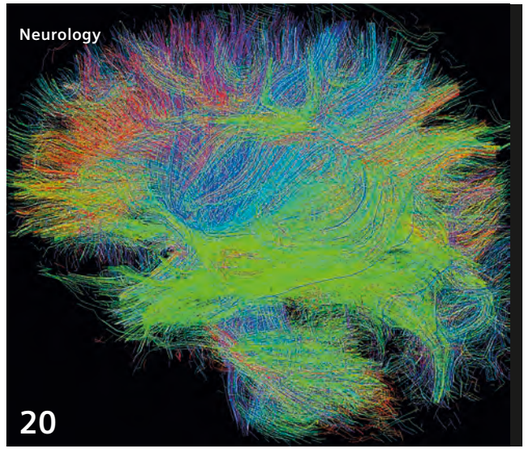

Diffusion MRI and quantitative tractography

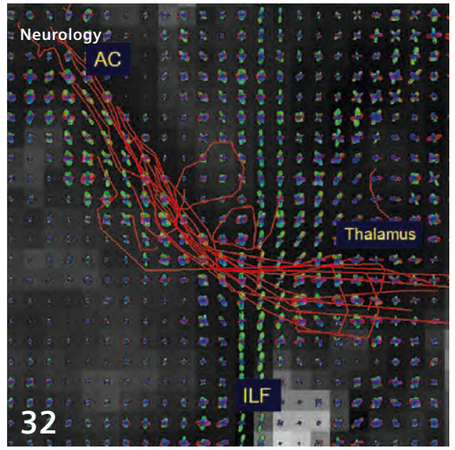

Diffusion and MRS applied to Autism

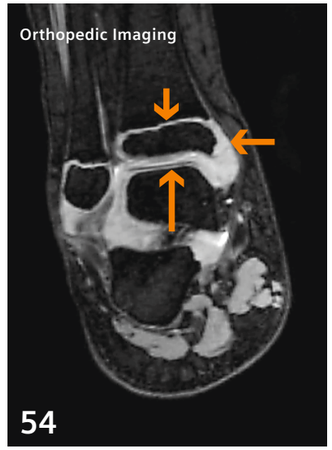

Pediatric cartilage using 3D DESS

TWIST to evaluate vascular malformations

Learn from the experience of other MAGNETOM users

The MAGNETOM World is the community of Siemens MR users worldwide, providing you with relevant clinical information. Here you will find application tips and protocols to optimize your daily work. Lectures and presentations from experts in the field will allow you to be exposed to new ideas and alternative clinical approaches.

Put the advantages of the MAGNETOM World to work for you!

www.siemens.com/magnetom-world

Abdominal Imaging

Neurology

Orthopedic Imaging

Cardiovascular Imaging

Radial 3D VIBE in the Pediatric Abdomen. A Report on Our Initial Experience

Michael Kean, FSMRT; Dr. Anna Moon, MBChB FRANZCR MBA

Children's MRI Centre, Royal Children's Hospital, Murdoch Children's Research Institute Parkville, Melbourne, Australia

The evaluation of the pediatric* abdomen and pelvis with MRI is a complex interaction of many factors but ultimately success or failure of the examination is reliant upon obtaining sequences free of motion-related artifacts.

Historically, ultrasound and CT have been the imaging modalities of choice for evaluation of the pediatric abdomen due to four main factors: Access, ease of incorporation into the clinical diagnostic profile, speed, and a greater capacity to freeze abdominal motion.

There have been numerous attempts over the years to compensate for the various types of motion within the abdomen. The earliest and most simple form of motion correction was to average out the phase-related ghosting by acquiring data with multiple averages. This method is still used today, but using more sophisticated sequences such as BLADE. The problem with this solution is scan time, which each additional average chews up. Respiratory gating / triggering have proven to be very successful in obtaining T2-weighted images of a very high diagnostic standard, but they ultimately require the patient to breathe in a regular pattern to obtain scan efficiency and motion artifact free images.

Many attempts to implement more sophisticated motion insensitive sequences have been limited by system hardware and reconstruction times. As the coils and gradients became more sophisticated, motion artifacts were reduced by obtaining scans in breath-holds: This was fine for adolescents and adults, but what about sedated infants?

So as with most things old becomes new, by opting instead for a non-cartesian sampling algorithm we can now perform image averaging in a more sophisticated form with radial sampling**. The combination of stack-of-stars radial sampling in-plane and cartesian sampling through-plane has dramatically improved T1-weighted imaging in our patients.

No advancement is without its downside, however, and, Radial VIBE acquisitions are more vulnerable than cartesian-based VIBE to off-resonant effects. Instead of the traditional chemical shift effects produced with standard imaging, the radial VIBE suffers from image blurring in the presence of strong off-resonance tissues such as fat. To mitigate these effects we must use a spectral fat suppression technique for these acquisitions: Our preference is to use SPAIR. In areas of poor homogeneity you may get a small degree of image blurring or image streaks but in our experience these have not rendered the acquisition non-diagnostic.

There is another source of potential image blurring or streaking caused by through-plane motion of the abdominal structures or concentrated volumes of contrast. To minimize the in-plane and through-plane motion of abdominal structures we administer buscopan (or glucagon) in patients who meet our institution's clinical guidelines.

Most of our experience has been gained using these sequences on the 3T MAGNETOM Trio and Verio, both operating on *syngo* MR B17 software, using either the standard body matrix coil or 32-channel cardiac coil. In cases of very small infants we may incorporate the large flex or the 15-channel transmit / receive extremity coil. The acquisition factors for the Radial VIBE sequence are usually 2.0–2.5 mm slice thickness and in-plane interpolated resolution of 0.4 × 0.4 mm with an average acquisition time of 1.75 minutes, depending on the number of slices in the imaging volume, field-of-view or coil.

The choice of 3D VIBE standard Dixon or Radial VIBE depends on the clinical indication. If a non-fat suppressed acquisition or dynamic multi-phase acquisition is required we will incorporate both standard and Radial VIBE sequences into the protocol. Current sequence developments, including the use of advanced iPAT techniques such as Caipirinha and Dixon, will increase the clinical utility of the sequence.

This sequence has become an integral part of our abdominal and pelvis protocols thanks to its higher signal-to-noise, high diagnostic sensitivity to pathology, increased spatial resolution, and consistent reduction in motion artifacts when compared to standard 3D breath-hold VIBE sequences.

*Siemens disclaimer: MR scanning has not been established as safe for imaging fetuses and infants less than two years of age. The responsible physician must evaluate the benefits of the MR examination compared to those of other imaging procedures.

**Radial VIBE is a prototype for StarVIBE. StarVIBE is available for 1.5T MAGNETOM Aera and 3T MAGNETOM Skyra. Radial VIBE is WIP, the product is currently under development and is not for sale in the US and in other countries. Its future availability cannot be ensured.

Case 1

7-month-old infant* requiring liver / spleen volumes prior to initiation of treatment for Gaucher's Disease.

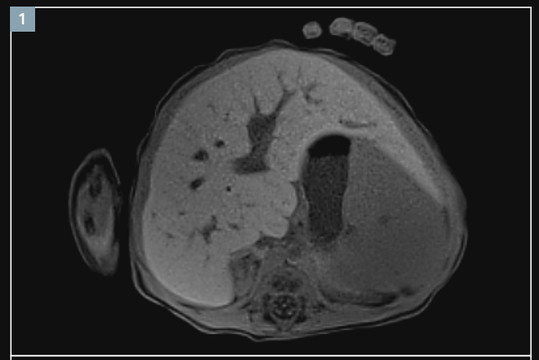

1 Radial 3D VIBE.

Case 2

7-year-old female presented with abdominal mass. Initial CT performed on admission demonstrated Paraspinal Ganglioneuroma, MRI was obtained to determine the extent of intra-spinal extension and tumor planes for surgical excision.

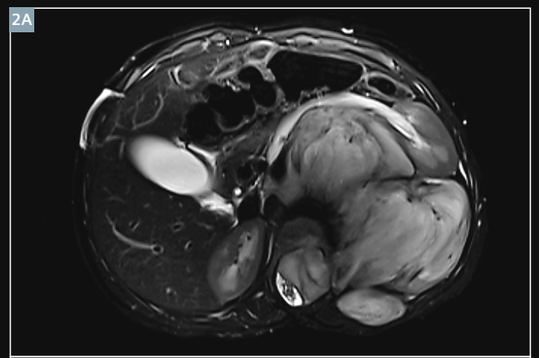

2A Transverse T2-weighted SPAIR using navigator.

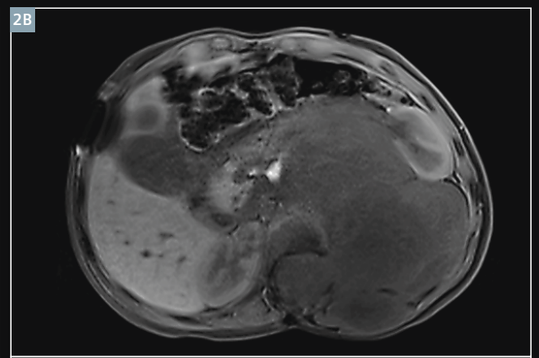

2B 3D VIBE Dixon breath-hold.

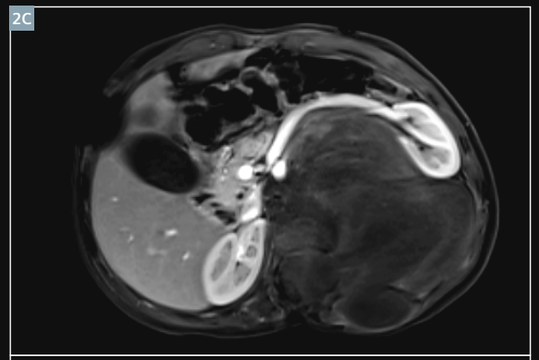

2C 3D VIBE Dixon breath-hold water image post-contrast.

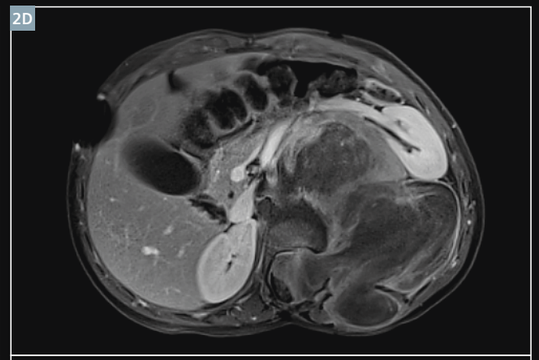

2D 3D Radial VIBE SPAIR post-contrast.

Case 3

Adolescent female presented with lower pelvic pain, refused full examination and decided to follow alternate natural pathway. Presented 2 weeks later with increasing pain. Palpable superficial enlarged lymph nodes biopsied showing disseminated disease. Due to social circumstances MRI was the initial diagnostic pathway. Post MRI biopsy Rhabdomyosarcoma.

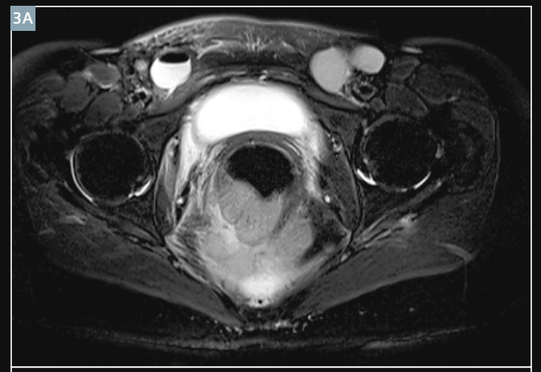

3A Transverse T2-weighted SPAIR breath-hold sequence.

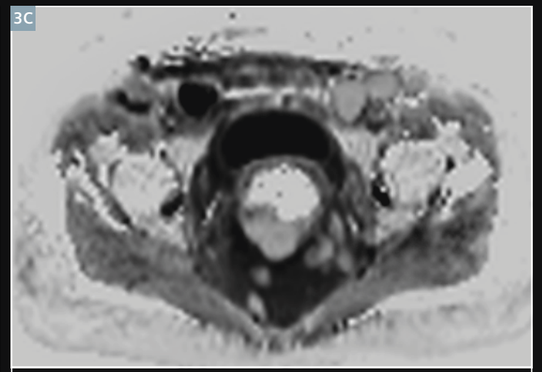

3C Transverse multi b-value DWI, inverted ADC demonstrating infiltrative tumor and lymph nodes.

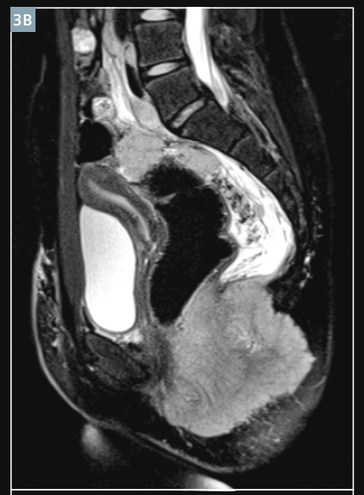

3B Sagittal SPAIR breath-hold T2-weighted TSE sequence.

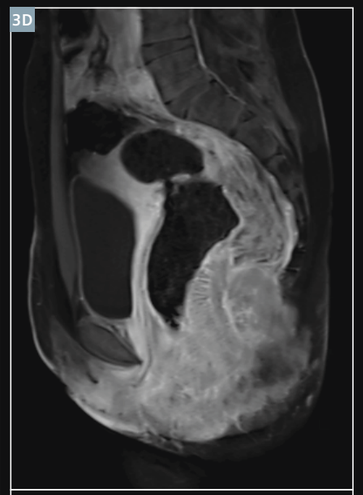

3D 3D VIBE Dixon post-contrast.

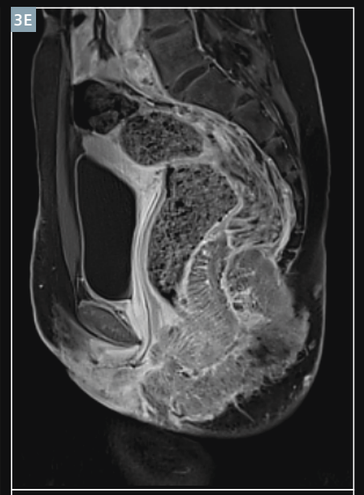

3E 3D Radial VIBE SPAIR post-contrast.

Case 4

7-month-old* male transferred from peripheral hospital with enlarging abdominal mass. CT on presentation demonstrated large enhancing mass. MRI was performed as part of staging prior to resection.

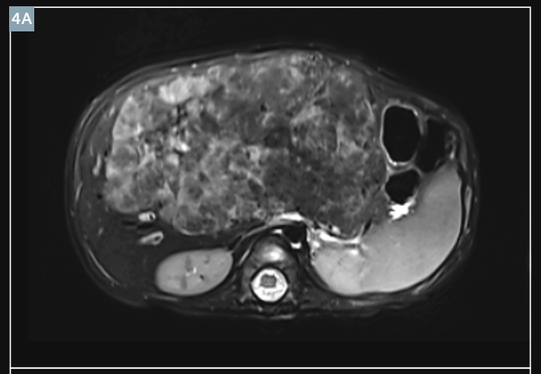

4A Navigator free breathing transverse SPAIR T2w TSE sequence.

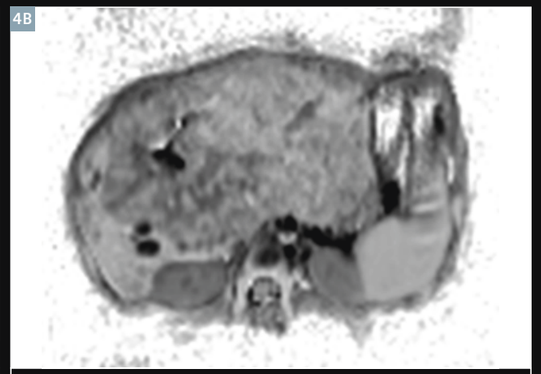

4B Multi b-value DWI, ADC inverted.

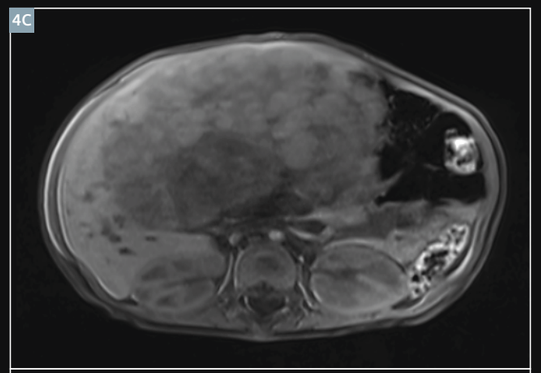

4C 3D Dixon VIBE breath-hold.

4D 3D SPAIR Radial VIBE.

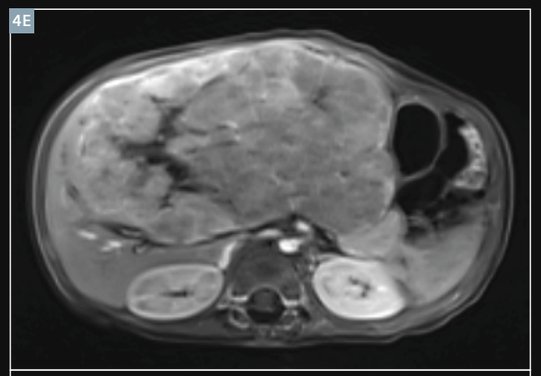

4E 3D Dixon VIBE breath-hold post-contrast.

4F 3D SPAIR Radial VIBE post-contrast.

Case 5

Patient transferred from interstate with incomplete scan showing intra-thoracic mass with probable intra-thecal extension, probably neuroblastoma. Comprehensive MRI under anesthesia demonstrated metastatic neuroblastoma.

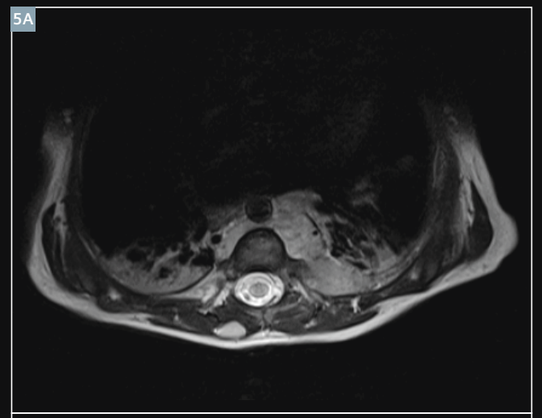

5A Transverse T2w TSE images of the thoracic spine.

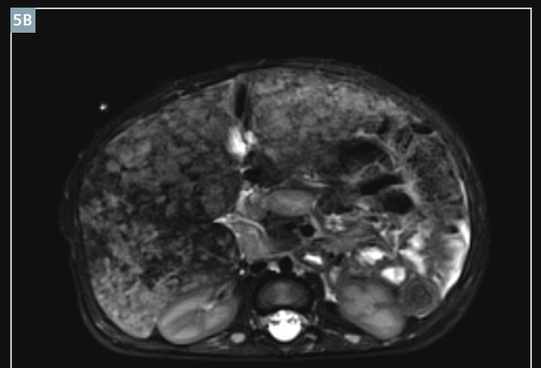

5B Transverse T2w SPAIR BLADE.

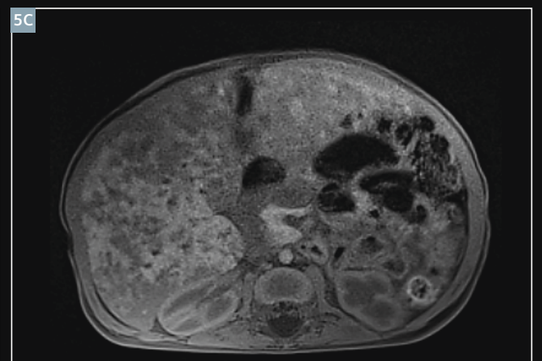

5C Transverse 3D SPAIR Radial VIBE.

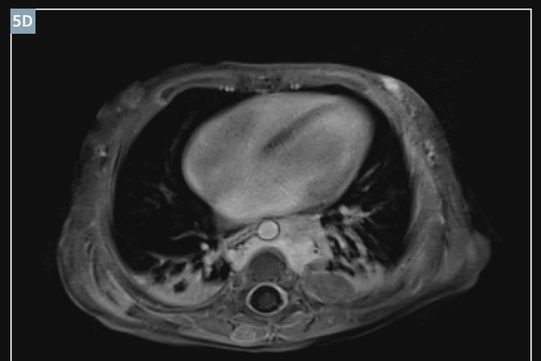

5D Transverse 3D Radial VIBE chest demonstrating tumor enhancement with no vascular or cardiac related artifacts.

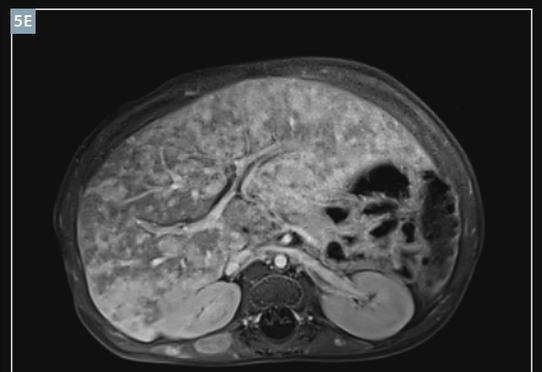

5E Transverse 3D Radial VIBE post-contrast.

Case 6

Hepatoblastoma – pre chemotherapy staging.

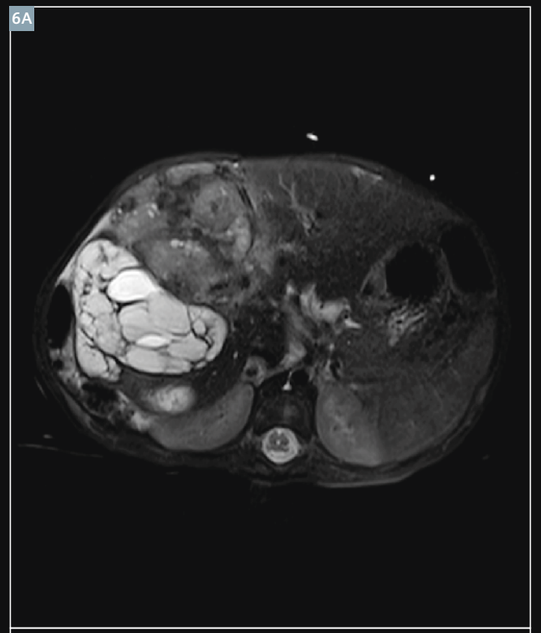

6A Transverse T2w SPAIR BLADE navigator.

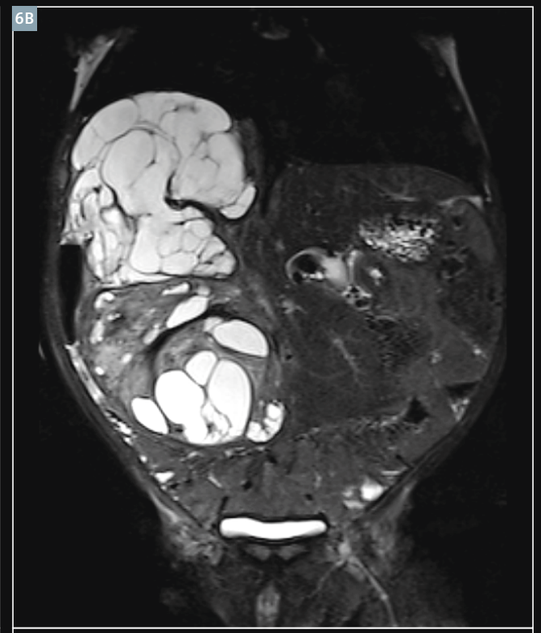

6B Coronal T2 SPAIR BLADE navigator.

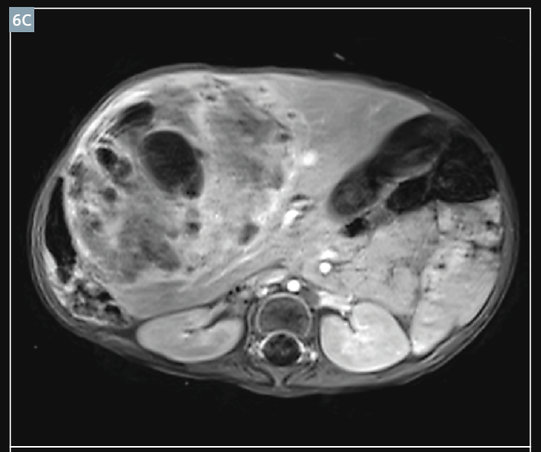

6C Transverse 3D Dixon VIBE post-contrast.

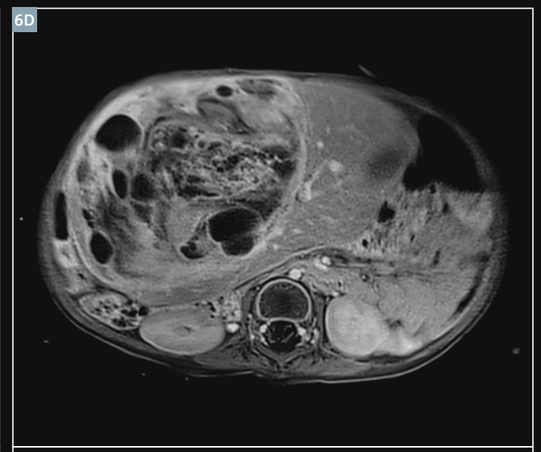

6D Transverse SPAIR 3D Radial VIBE.

Case 7

Metastatic Neuroblastoma.

7A Composed sagittal T2w FS spine demonstrating multiple metastasis.

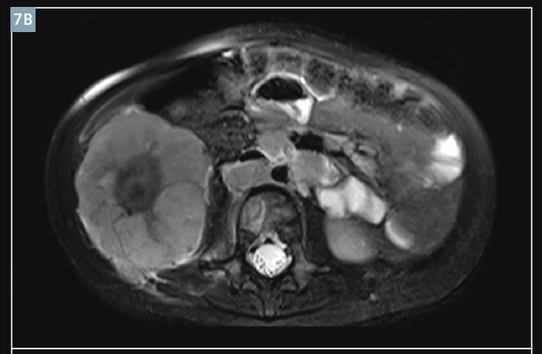

7B Transverse T2w SPAIR free breathing.

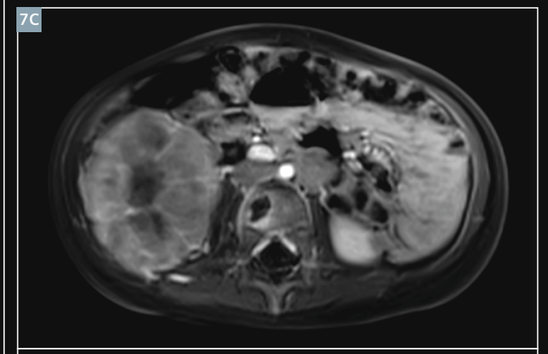

7C Breath-hold 3D Dixon VIBE.

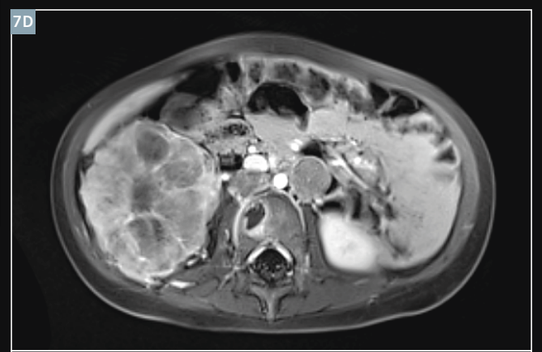

7D 3D SPAIR Radial VIBE.

Case 8

Metastatic vaginal adenocarcinoma.

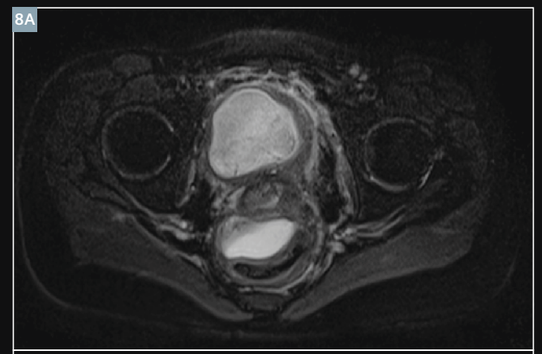

8A Transverse T2w SPAIR.

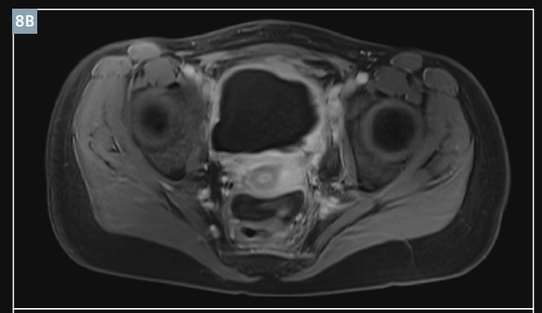

8B 3D Dixon VIBE breath-hold post-contrast.

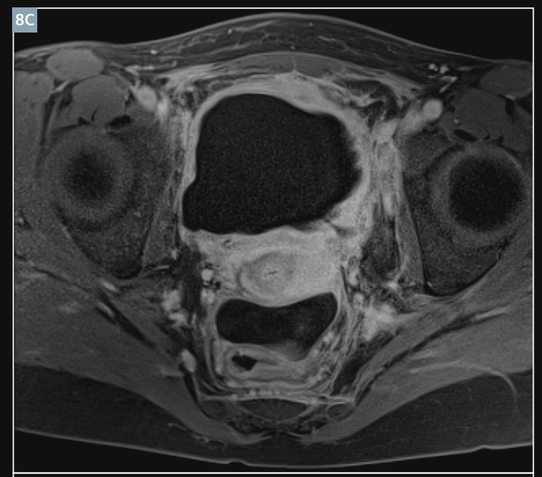

8C 3D SPAIR Radial VIBE post-contrast.

Further reading

1 Chandarana H, Block KT, Rosenkrantz AB, Lim RP, Kim D, Mossa DJ, Babb JS, Kiefer B, Lee VS. Free-breathing radial 3D fat-suppressed T1-weighted gradient echo sequence: a viable alternative for contrast-enhanced liver imaging in patients unable to suspend respiration. Invest Radiology 46(10):64853, 2011.

2 Chandarana H, Block KT, Winfeld JM, Lala SV, Mazori D, Giuffrida E, Babb JS, Milla S. Free-breathing contrast enhanced T1 weighted gradient-echo imaging with radial k-space sampling for paediatric abdominopelvic MRI. European Radiology, September 2013.

3 Block KT. Improving the robustness of clinical T1-weighted MR imaging using Radial VIBE. MAGNETOM Flash, (5); 6-12, 2013.

Acknowledgements

The authors wish to acknowledge the ongoing collaboration support from Siemens Healthcare in developing novel pediatric imaging techniques.

Contact

Michael Kean FSMRT
Chief MRI Technologist
The Royal Children's Hospital
Flemington Road, Parkville
Victoria, Australia, 3052
michael.kean@rch.org.au

Quiet Sequences for Pediatric Patients: T1-PETRA and Quiet SWI

Noriko Aida, M.D., Ph.D.

Department of Radiology, Kanagawa Children's Medical Center, Yokohama, Japan

Background

In conventional MRI examinations, fast gradient switching leads to high acoustic noise. High acoustic noise from MRI sequences may disturb sedated pediatric patients* and is one of the main reasons for patient restlessness. Not a few children who undergo an MR study without sedation say that the loud noise from MRI is dreadful, and they may hesitate to undergo an examination or to continue one until completion.

We had an opportunity to perform a pediatric clinical trial of two quiet sequences: A T1-weighted prototype PETRA (T1-PETRA) sequence**, and a prototype quiet Susceptibility-weighted imaging (qSWI) sequence**.

For pediatric patients who underwent routine brain MRI under sedation, we attempted to run T1-PETRA and qSWI without applying additional sedative drugs after examinations that included MPRAGE and conventional SWI (cSWI). Our Institutional Review Board approved this prospective study, and written consent was obtained from parents.

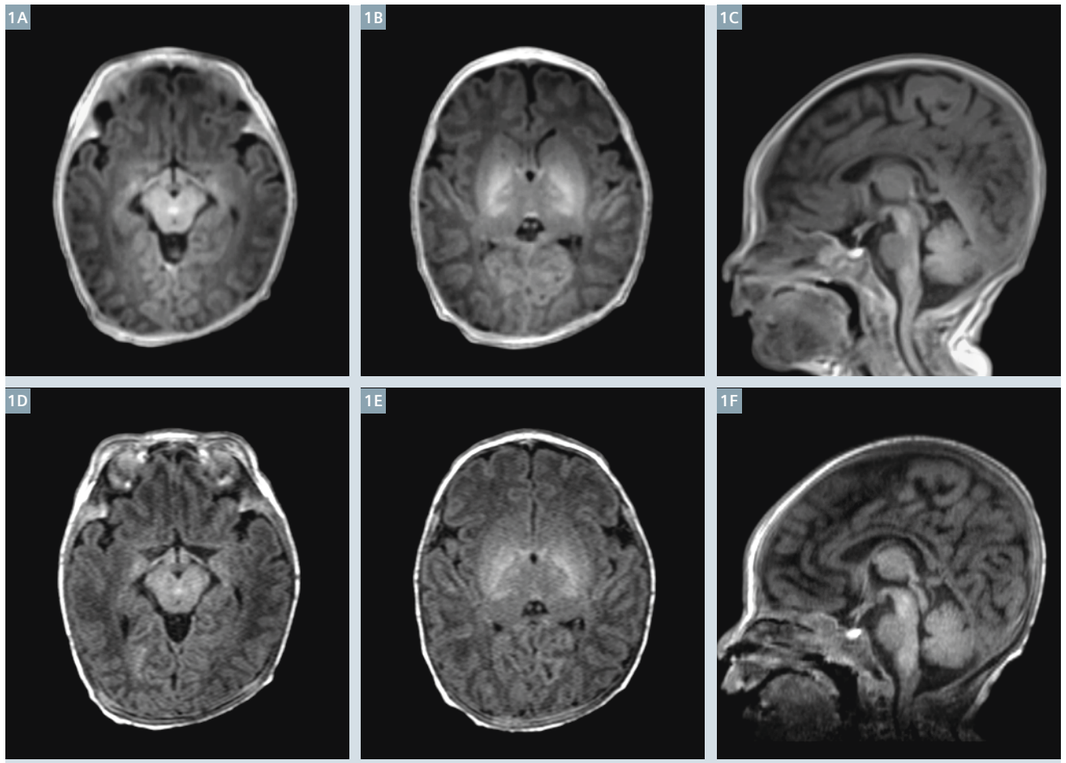

1 Images of a 9-day-old neonate*. **(1A–C)** T1-PETRA, **(1D–F)** MPRAGE.

All studies were performed on a 3T clinical scanner (MAGNETOM Verio, Siemens, Erlangen) using a 32-channel head coil.

Here we introduce our protocols and demonstrate the image quality of quiet sequences by showing their images.

T1-PETRA

The PETRA sequence [1] only requires very limited gradient activity and allows for inaudible scanning. However, contrast in PETRA is limited unless pre-pulses are used. In the T1-PETRA sequence, the timing of inversion pulses has been optimized for T1-weighted head scanning [2]. The *k*-space center is measured after the very first inversion pulse. Since the brains of developing infants have a longer T1 value than those of older patients, a longer first TI was used for them (measured brain T1 value x 0.7). In our trial, the scan time of T1-PETRA was adjusted to be as short as possible while maintaining sufficient spatial resolution. Our routine MPRAGE and T1-PETRA protocols are shown in Table 1. We measured the acoustic noise levels of each sequence in the MR examination room. The mean acoustic noise levels of MPRAGE and PETRA were, respectively, 34.0 dB_A and 4.8 dB_A higher than the baseline noise level of 53.4 dB_A; i.e., the noise levels without subtracting the baseline were 87.4 dB_A and 58.2 dB_A at a distance of 2.5 m from the front panel of the magnet.

We were able to perform both T1-PETRA and MPRAGE imaging in about 60 children, from neonates* to 14 years of age. Although each sequence had different effective spatial resolutions, we were able to judge the degree of myelination on T1-PETRA images with accuracy equivalent to that of MPRAGE, and we believe PETRA provides T1-weighted images of sufficient quality for routine diagnostic use in pediatric neuroradiology as shown in Figures 1 and 2.

The acoustic noise of PETRA was only 4.8 dB_A above the background and was nearly silent, in contrast with MPRAGE which had a noise level that was 34.8 dB_A above the background. Children seldom woke up during the PETRA sequence.

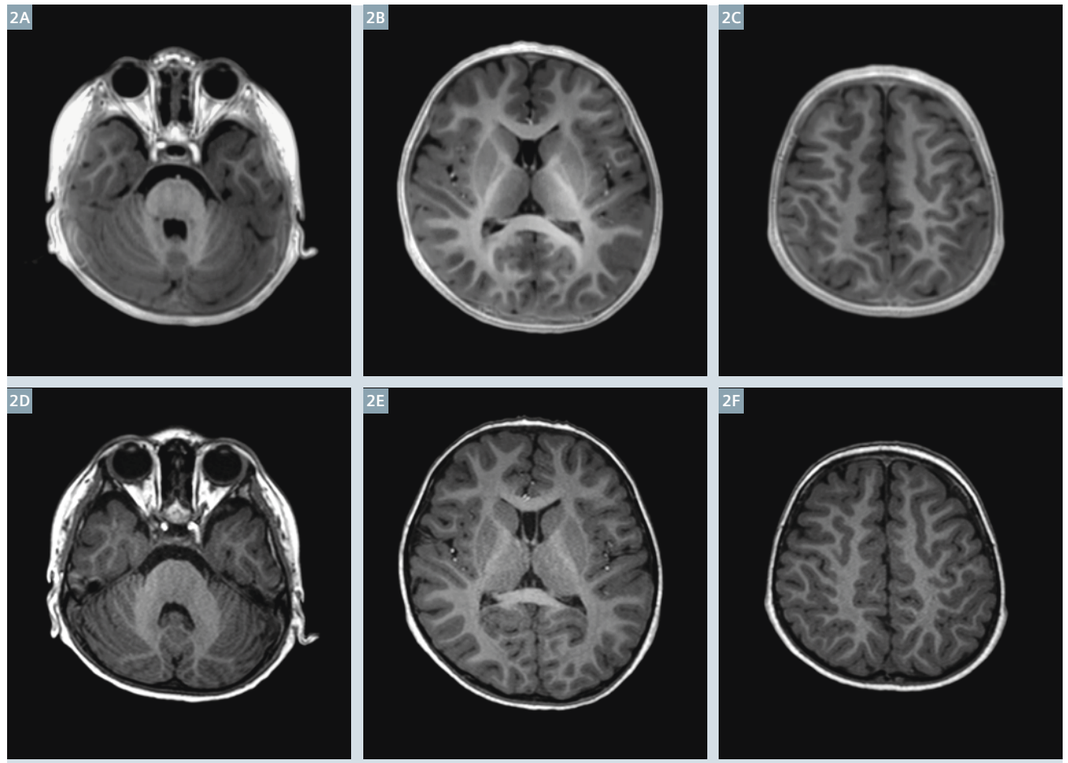

2 Images of a 27-month-old girl*. **(2A–C)** T1-PETRA, **2(D–F)** MPRAGE.

Table 1: Parameters for conventional and quiet T1-weighted sequences

	MPRAGE			PETRA
Orientation	Transverse	Transverse	Transverse	Sagittal
FOV (mm)	150	200	240	285
TI (ms)	800	800	800	700
TR (ms)	1570	1570	1570	2350
TE (ms)	2.14	2.79	2.77	0.07
Echo space	5.2	5.2	5.2	3.75
Slice thickness (mm)	1	1	1	0.8
FOV Phase	100%	87.50%	87.50%	100%
Slice oversampling	100%	36.40%	25.00%	0%
Slice per slab	128	176	192	352
Flip angle (degrees)	9	9	9	6
Matrix	154 x 192	168 x 192	224 x 256	352 x 352
Scan time (min:sec)	3:27	3:05	3:05	4:20

Table 2: Parameters for conventional and quiet SWI sequences

FOV (mm)	150		200		240	
	cSWI	qSWI	cSWI	qSWI	cSWI	qSWI
TR (ms)	38	39	38	39	38	39
TE (ms)	30	30	30	30	30	30
Slice thickness (mm)	1.5	1.5	1.5	1.5	1.5	1.5
FOV Phase	87.5%	87.5%	87.5%	87.5%	87.5%	87.5%
Slice oversampling	14.3%	14.3%	22.2%	22.2%	22.2%	22.2%
Slice per slab	56	56	72	72	72	72
Flip angle (degrees)	15	15	15	15	15	15
Matrix	168 x 256	168 x 256	235 x 320	235 x 320	258 x 320	258 x 320
PAT	3	3	4	4	4	4
Scan time (min:sec)	3:09	3:14	4:53	5:01	4:50	5:20

qSWI

Recently SWI has become widely used in brain MRI, even for pediatric patients [3, 4]. However, the continuously high acoustic noise from conventional SWI (cSWI) over several minutes may disturb sedated pediatric patients. A prototype qSWI sequence with optimized gradients was used in order to reduce acoustic noise. The parameters of qSWI and cSWI were nearly identical. Within the qSWI sequence, an automated algorithm optimized the gradient objects to allow for the lowest possible slew rates. Our routine cSWI and qSWI protocols are shown in Table 2.

We measured the acoustic noise levels of each sequence in the MR examination room. The mean acoustic noise levels of cSWI and qSWI were, respectively, 30.7 dB_A and 21.9 dB_A higher than the baseline noise level of 53.4 dB_A; i.e., the noise levels without subtracting the baseline were 84.1 dB_A and 75.3 dB_A, respectively, at a distance of 2.5 m from the front panel of the magnet.

We were able to perform both cSWI and qSWI scans in over 50 children, from neonates to 18 years of age. All cSWI and qSWI images were of sufficient quality for radiological interpretation, and it was difficult to differentiate between cSWI and qSWI images as shown in Figure 3.

Furthermore, qSWI with a setting of 'fast mode' for RF pulses resulted in about 5 dB_A lower acoustic noise than that of 'normal mode' which was used for qSWI in this study, and provided

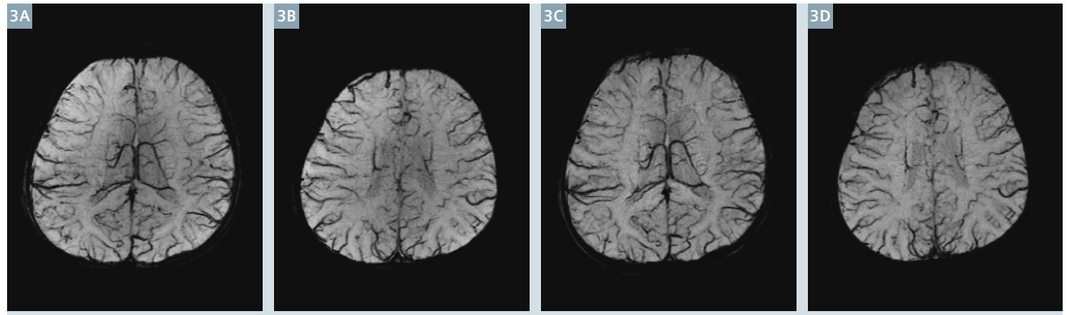

3 Images of a 5-month-old boy*. **(3A, B)** qSWI, **(3C, D)** cSWI.

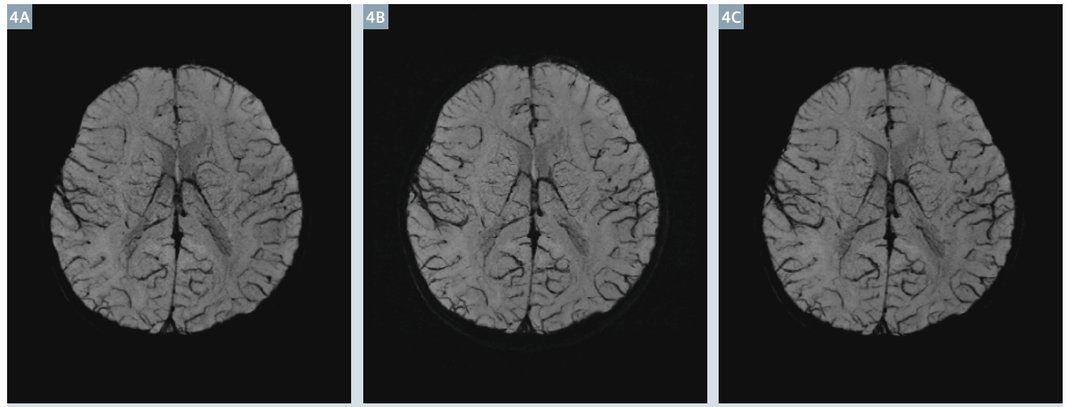

4 Images of a 3-year-old boy. **(4A)** cSWI, **(4B)** qSWI with RF fast mode, **(4C)** qSWI with RF normal mode.

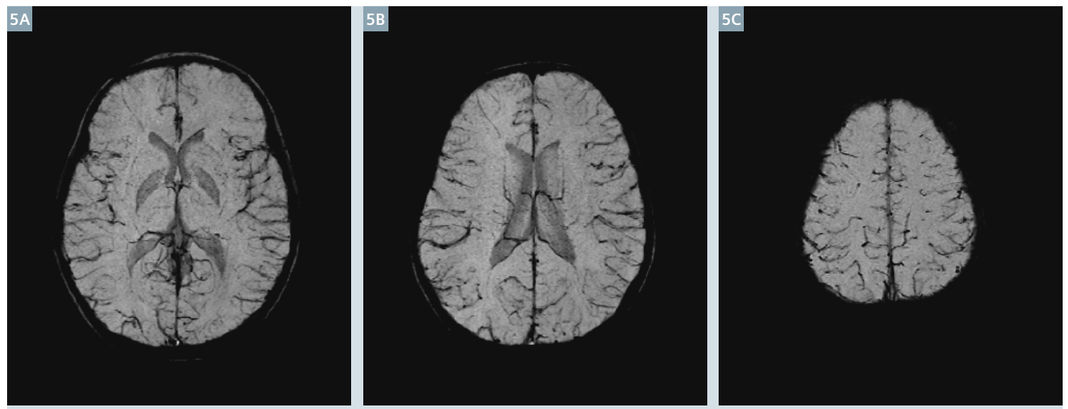

5 qSWI of an 8-year-old girl acquired on a 1.5T MAGNETOM Avanto.

almost identical image quality (Fig. 4). Therefore, following the study reported here, we decided to use fast mode for qSWI in our routine brain MRI, resulting in about 14 dB_A lower acoustic noise than that of cSWI. Moreover, qSWI can be used on a 1.5T clinical scanner (MAGNETOM Avanto, Siemens, Erlangen) with a 12-channel head coil, and may be substituted for cSWI in clinical diagnostic use at 1.5T in order to reduce acoustic noise (Fig. 5). On MAGNETOM Avanto, the mean acoustic noise levels of cSWI and qSWI were, respectively, 24.8 dB_A and 11.2 dB_A higher than the baseline noise level of 49.6 dB_A; i.e., the noise levels without subtracting the baseline were 74.4 dB_A and 60.8 dB_A, respectively, at a distance of 2.5 m from the front panel of the magnet.

*Siemens disclaimer: MR scanning has not been established as safe for imaging fetuses and infants under two years of age. The responsible physician must evaluate the benefit of the MRI examination in comparison to other imaging procedures.

**WIP, the product is currently under development and is not for sale in the US and other countries. Its future availability cannot be ensured.

Clinical application of quiet sequences and a patient's reaction

Quiet sequences are therefore a useful way to avoid disturbing sedated pediatric patients, and also to provide more comfortable scans to children who undergo MR examinations without sedation. An 8-year-old boy who was included in our study refused to undergo MR examination without sedation because of the loud acoustic noise. After he awoke, we ran cSWI, qSWI and T1-PETRA scans for a few seconds each, and we asked him about the acoustic noise of each sequence. He answered that he could not bear the acoustic noise of cSWI, so we stopped the scan immediately. Next he said that the qSWI scan noise was better though he did not like it. Finally, he commented that the acoustic noise of T1-PETRA caused no problem for him.

Conclusion

We conclude that T1-weighted PETRA is almost silent and can be a reliable substitute for MPRAGE, since it is a much gentler experience to pediatric patients with or without sedation, even though the scan time is approximately one minute longer. The qSWI sequence produced less acoustic noise by using slightly more scan time, and can be substituted for cSWI on both 3T and 1.5T scanners in order to provide gentler scans to pediatric patients.

References

1 Grodzki DM, Jakob PM, Heismann B. Ultrashort echo time imaging using pointwise encoding time reduction with radial acquisition (PETRA). Magn Reson Med. 2012 Feb; 67(2):510-8.
2 Grodzki et al. Proceedings. ISMRM 2013.
3 Tong KA, Ashwal S, Obenaus A, et al. Susceptibility-weighted imaging: a review of clinical application in children. AJNR 2008; 29:9-17.
4 Niwa T, Aida N, Kawaguchi H, et al. Anatomic dependency of phase shifts in the cerebral venous system of neonates at susceptibility-weighted MRI. JMRI 2011; 34:1031-6.

Contact

Noriko Aida, M.D., Ph.D.
Chief Radiologist
Department of Radiology
Kanagawa Children's Medical Center
2-138-4 Mutsukawa, Minami-ku
Yokohama, Japan 232-8555
Phone: +81 45-711-2351
naida@kcmc.jp

Using Diffusion MRI and Quantitative Tractography to Investigate Gender Specific Effects on the Development of White Matter after Preterm Birth at 3T

Mark E. Bastin[1]; Devasuda Anblagan[2]; Sarah Sparrow[2]; Emma Moore[2]; Rozi Pataky[3]; Chinthika Piyasena[4]; Graham Wilkinson[5]; Thorsten Feiweier[6]; Scott I. K. Semple[4,7]; James P. Boardman[2]

[1]Centre for Clinical Brain Sciences, University of Edinburgh, UK
[2]MRC Centre for Reproductive Health, University of Edinburgh, UK
[3]NHS Lothian, UK
[4]Centre for Cardiovascular Sciences, University of Edinburgh, UK
[5]Department of Paediatric Radiology, NHS Lothian, UK
[6]Siemens Healthcare, Erlangen, Germany
[7]Clinical Research Imaging Centre, University of Edinburgh, UK

Introduction

Preterm birth is a leading cause of cognitive impairment in childhood and is associated with alterations in brain development that are apparent in the neonatal period. Brain structural changes associated with preterm birth include enlargement of the ventricular system, reduced cortical complexity and diffuse white matter signal abnormalities on structural MRI (see Figure 1 and Reference [2]). However, some of the adverse neurodevelopmental sequelae of preterm birth are gender-specific, with preterm males having a worse neurodevelopmental outcome than preterm females [6, 7, 9] and some neuroprotective strategies appearing to have gender specific effects [10]. Connectivity of developing white matter tracts is altered in association with preterm birth but the neural basis for differential gender effects is unknown. Diffusion MRI (dMRI) and tractography may provide further insights into the cerebral microstructural changes that accompany preterm birth by supplying quantitative biomarkers of white matter integrity in specific tracts of interest (see Figures 2 and 3, and Reference [1]). We therefore present the first application of an automatic single seed point tractography-based segmentation method, probabilistic neighbourhood tractography (PNT) [3-5], to study gender specific effects in developing white matter tracts in preterm infants*. PNT, which can segment the same fasciculus across groups of subjects and provide quantitative measures of tract integrity and shape, works by placing seed points in a neighbourhood surrounding a seed point transferred from standard space, with the tract that best matches a predefined reference tract in terms of length and shape chosen from this group of 'candidate' tracts [4].

1 T2-weighted axial images at the level of the lateral ventricles from: **(1A)** A healthy infant* born at 39^{+1} weeks with images acquired at 41^{+3} weeks post menstrual age (PMA); **(1B)** An infant born at 25^{+0} weeks with image acquisition at 42^{+4} weeks PMA; and **(1C)** An infant born at 26^{+0} weeks, with images acquired at 39^{+3} weeks PMA. **Figure 1B** shows features that are common among preterm infants at term equivalent age including enlargement of the ventricular system and extra cerebral space reduced cortical complexity and diffuse excessive high signal intensity in the white mattter (arrows) compared with (1A). **Figure 1C** shows areas of cystic periventricular leucomalacia (long arrows) distinct from the lateral ventricles (short arrows).

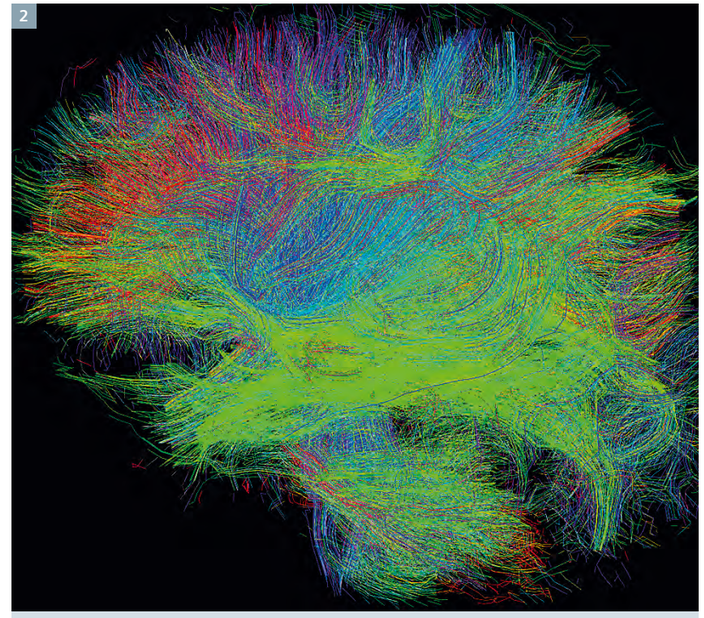

2 Sagittal view of whole brain white matter obtained using dMRI from a healthy neonate.

Methods

Following ethics committee approval, 49 preterm infants born at post-menstrual age (PMA) of 29 ± 6 weeks were scanned on a MAGNETOM Verio 3T clinical scanner (Siemens Healthcare, Erlangen, Germany) at term equivalent age (PMA 40 ± 3 weeks) without sedation. All infants were scanned axially using a dMRI protocol consisting of 11 T2- and 64 diffusion-weighted ($b = 750$ s/mm^2) single-shot, spin-echo, echo planar imaging volumes acquired with 2 mm isotropic voxels (field-of-view 256 × 256 mm, imaging matrix 128 × 128, 50 contiguous interleaved slices with 2 mm thickness) using the 'Works-in-Progress Package for Advanced EPI Diffusion Imaging (WIP 511 E)'**. To reduce eddy current induced artefacts and shimming errors to a minimum, the bipolar+ gradient pulse scheme was selected, with manual shimming and shim box covering a region extending from the top of the head to several centimetres below the chin.

Ten fasciculi-of-interest (FOI) were identified using PNT from the dMRI data (http://www.tractor-mri.org.uk): Genu and splenium of corpus callosum, right and left projections of the arcuate, cingulum cingulate gyri (CCG), corticospinal tract and inferior longitudinal fasciculi. Using a 7 × 7 × 7 neighbourhood of seed voxels, the seed point that produced the best matching tract to the reference (defined in Montreal Neurological Institute standard space; http://www.mni.mcgill.ca) was determined using tract shape models produced from a group of adult volunteers aged 25–65 years [3]. Streamlines that did not resemble the median path of the best-matched tract were pruned automatically [5]. An experienced rater then visually assessed all best matched tracts and subjects with aberrant or truncated pathways that were not anatomically plausible representations of the FOI were excluded from further analysis. For anatomically acceptable tracts, the resulting tractography masks were applied to each subject's mean diffusivity (MD) and fractional anistropy (FA) maps to provide tract-averaged measures of these biomarkers for the 10 FOI.

Results

Figure 3 shows an example of the tract segmentation for a subset of 12 subjects for genu and splenium of corpus callosum, and indicates the close spatial correspondence of the segmented pathways for these two tracts.

The gender effect for tract-averaged FA and MD for the 10 FOI in each subject were assessed using an independent samples t-test. Tract-averaged FA values of the left CCG were significantly increased in male infants ($p = 0.05$), while MD of the left CCG were significantly increased in female infants ($p < 0.04$). To assess the effect of PMA at birth and PMA at scanning on these dMRI biomarkers, a general linear univariate model based on one between-subject variable was performed for FA and MD in the 10 FOI. Two important covariates were included in all analyses: PMA at birth and PMA at scanning. Track averaged MD of the left CCG was significantly increased ($p < 0.03$) in female infants (1551 ± 285 μm^2/s) compared to male infants (1397 ± 858 μm^2/s).

Discussion

These pilot data show for the first time that quantitative measurements of dMRI biomarkers can be made in the preterm brain from high angular resolution dMRI data using PNT at 3T. These values are comparable to other studies using tractography methods, and demonstrate increased MD and reduced FA in the CCG of female preterm infants compared with male equivalents. Of particular interest is the fact that the method is able to identify successfully a range of fasciculi using reference tracts obtained from the adult brain. This approach may be useful for studying sexual dimorphism early in human development. We are currently investigating whether the use of reference tracts from infants further improves this study, and whether the tract shape parameter R (the absolute goodness-of-fit of the best match tract to the reference) provides additional useful information about brain structure that can be used to assess cerebral development in preterm birth and potential therapeutic interventions.

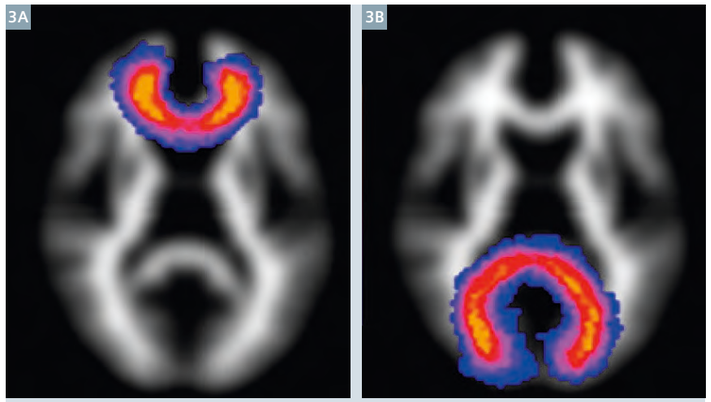

3 Group maps of **(3A)** genu and **(3B)** splenium generated by transforming the best match tract for each subject into MNI standard space.

Acknowledgements

This work was funded by Theirworld and was carried out in collaboration with Siemens Healthcare. The authors would like to thank Craig Buckley for his valuable participation and support.

* Siemens disclaimer: MR scanning has not been established as safe for imaging fetuses and infants less than two years of age. The responsible physician must evaluate the benefits of the MR examination compared to those of other imaging procedures. This disclaimer does not represent the view of the authors, nor the view of the guest editor of this issue. It is solely for regulatory reasons.

** WIP, the product is currently under development and is not for sale in the US and other countries. Its future availability cannot be ensured.

References

1 Ball G, et al. Cortex. 2013 Jun; 49(6): 1711-21.
2 Boardman JP, et al. (2010) Neuroimage 52:409-414.
3 Bastin ME, et al. (2010) Neuroimage 51:1-10.
4 Clayden JD, et al. (2007), IEEE Trans Med Imaging 26: 1555-1561.
5 Clayden JD, et al. (2011), J Stat Software 44 (8): 1-18.
6 Edwards D. (2004) J Pediatr 145(6):723-724.
7 Kapellou O, et al. (2006) PLoS Med 3(8): e265.
8 Mackay DF, et al. (2010) PLoS Med 7(6): e1000289.
9 Marlow N, et al. (2005) N Engl J Med 352: 9-19.
10 Ment LR, et al. (2004), J Pediatr 145 (6): 832-834.

Contact

Mark Bastin, DPhil
Reader in Medical Imaging
Centre for Clinical Brain Sciences
University of Edinburgh
Western General Hospital
Crewe Road, Edinburgh,
EH4 2XU, UK
Phone: +44 (0) 131 537 2511
Mark.Bastin@ed.ac.uk

Insights in Tuberous Sclerosis Complex from Novel Diffusion-Weighted Imaging Models

Jurriaan M. Peters[1,2,*]; Maxime Taquet[2*]; Benoit Scherrer[2]; Jolene M. Singh[2]; Anna K. Prohl[1]; Sanjay P. Prabhu[2]; Mustafa Sahin[1]; Simon K. Warfield[2]

*These authors contributed equally
[1] Division of Epilepsy and Clinical Neurophysiology, Department of Neurology, Boston Children's Hospital & Harvard Medical School, Boston, MA, USA
[2] Computational Radiology Laboratory, Department of Radiology, Boston Children's Hospital & Harvard Medical School, Boston, MA, USA

Background

Tuberous Sclerosis Complex (TSC) is a genetic neurocutaneous syndrome with an incidence of about 1:6000, and more than one million people affected worldwide. It is associated with significant comorbidity as benign lesions called hamartomas can develop in multiple organ systems including the kidneys, lungs, heart, brain and eyes. Neurologically, the presentation of TSC is highly variable, and manifests with intellectual disability, behavioral problems, autism spectrum disorder, and often-intractable epilepsy [1]. These symptoms are particularly burdensome as they frequently occur early in life, and impact development and long-term neurological outcome.

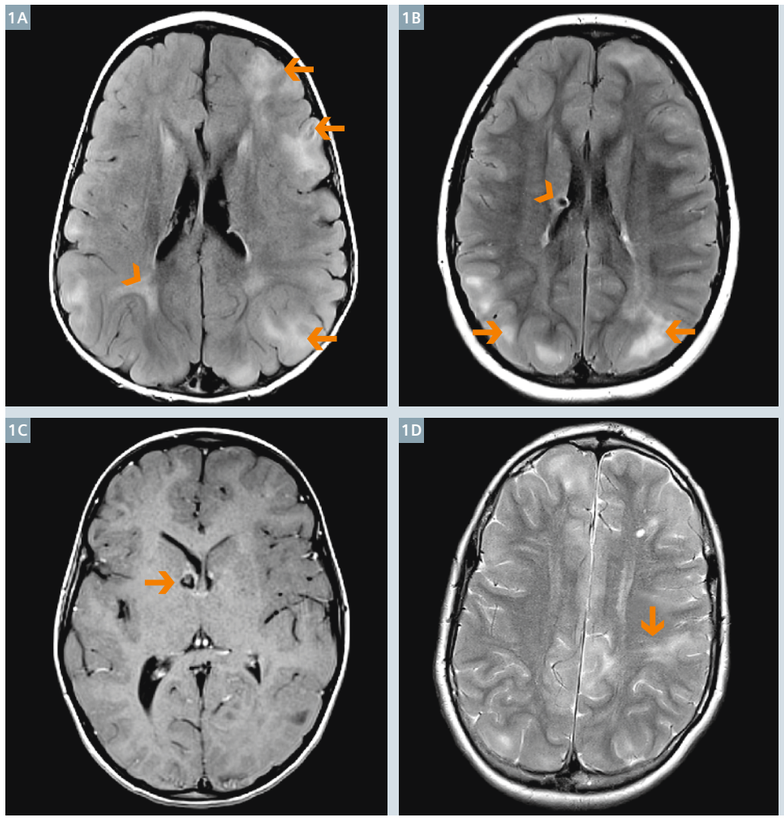

1

Conventional MR imaging findings in Tuberous Sclerosis Complex. All images are in the axial plane. **(1A)** Fluid-Attenuation Inversion Recovery (FLAIR) image reveals multiple hyperintense subcortical tubers (arrows). Some follow the gyral pattern (arrowhead). **(1B)** FLAIR image with posterior tubers (arrows) and a subependymal nodule (SEN; arrowhead). **(1C)** T1-weighted MPRAGE image with gadolinium contrast reveals a partially enhancing subependymal giant cell astrocytoma (SEGA) close to the foramen of Monro, posing a hydrocephalus risk. **(1D)** FLAIR image with linear T2-hyperintensities traveling from cortex towards the ventricle, reflecting radial migration lines (RML; arrow).

The correlation between genotype and phenotype is limited, and on an individual level does not allow for predicting neurological prognosis. Clinical determinants of neurological and cognitive outcome are the presence of seizures in early life (specifically, infantile spasms), age at onset and severity of epilepsy [2, 3]. While there is emerging evidence that seizure control in early life may lead to better neurological outcome [4, 5], there are no clinical or genetic early predictors of neurological outcome.

Neuroimaging reveals several abnormalities, and brain imaging** is routinely used for both diagnosis and monitoring of the disorder (Fig. 1). Tubers are juxtacortical cerebral and cerebellar hamartomas, which consist of abnormally differentiated and migrated cells. Subependymal nodules (SEN) line the ventricular ependyma, and when larger than 1 cm are referred to as subependymal giant cell astrocytoma (SEGA). Finally, radial migration lines (RML) represent gliosis and aberrant centrifugal migration of glia and neurons en route to the cortex. Quantification (and perhaps localization) of each of these lesions reflects to some extent the cerebral burden of the disease [6], but the correlation with overall outcome is not sufficient on an individual level to prognosticate. In short, there is no robust imaging biomarker for reliably predicting neurological outcome in TSC patients. And, conventional MRI cannot be used for early institution or monitoring of therapeutic interventions regarding autism spectrum disorder, epilepsy and cognitive impairment related to TSC.

Diffusion Tensor Imaging (DTI) offers the possibility of a putative biomarker for neurological outcome in TSC, essentially through modeling the underlying microstructural neuropathology of TSC. In this article, we will review DTI and the TSC phenotype, the limitations of the single tensor model, and the promise of novel diffusion acquisition and modeling techniques. The basics of diffusion-weighted imaging and detailed conventional imaging and clinical aspects of tuberous sclerosis complex can be found in a prior review by this group [7].

Aberrant neural connectivity in TSC

The TSC1 and TSC2 genes encode the proteins TSC1 (hamartin) and TSC2 (tuberin), respectively. TSC1 and TSC2 form a heterodimer, and regulate the mammalian target of rapamycin (mTOR), to form a protein complex responsible for protein synthesis, cell proliferation, and cell size regulation. In patients with TSC, the inhibition of the mTOR signaling pathway fails and uncontrolled growth occurs on multiple cellular levels [1].

Several rodent models of TSC exist, and are reviewed elsewhere [8]. Of importance, while none of the rodent models is able to replicate SEN, SEGA, RML or tubers, phenotypically they can have cognitive impairment and deficiencies in learning, behavioral and social deficits, seizures and early mortality. This suggests a role for non-tuber pathology in the pathogenesis of neurological symptoms in TSC, and the structural correlate of neurological deficits in animal models of TSC may lie in the microstructural neuroanatomy. Indeed, microstructurally, TSC knockout mice have been shown to have deficits in myelination, and in neuronal connectivity – specifically neuronal polarity, axon formation and guidance [9-11].

Indirectly, several lines of evidence suggest a similar abnormal neural connectivity in human patients with TSC. Cytoarchitectural abnormalities have been reported throughout the cerebral cortex, outside of the classic lesions, suggesting widespread microstructural pathology [12]. Through the use of depth electrodes in patients with TSC undergoing epilepsy surgery, epileptic activity adjacent to the conventionally described tubers has been found [13, 14]. Anecdotally, TSC patients without tubers can have epilepsy and conversely, patients with tuber pathology can have (near-) normal intelligence. Finally, in non-syndromic (idiopathic) autism, decreased cortico-cortical connectivity has been described using various conventional, diffusion and functional imaging modalities [15]. The high prevalence of (syndromic) autism in TSC may also reflect abnormal neuronal connectivity, which would be consistent with the current view of autism as a disconnection syndrome [15, 16].

Diffusion tensor imaging

The first reports of abnormal diffusion in TSC, starting in 2001, focused on tubers, which appear as areas of decreased FA and increased MD, consistent with pathological findings of poorly organized collections of dysplastic and abnormally enlarged cells [17]. While tubers appear discrete and well-delineated on fluid attenuation inversion recovery (FLAIR), diffusion imaging revealed an abnormal *perituber* white matter and a more gradual transition to the white matter, suggesting that pathology is more widespread than the tubers alone. Moreover, even the white matter only *appears* normal, as a growing body of work describes increased MD and decreased FA, compared to controls, in the conventionally normal appearing white matter (NAWM) – summarized in [18]. Thus, diffusion tensor imaging supports diffusely present deficits in migration, myelination and differentiation beyond tuber and perituber regions.

Both in imaging and in pathological studies patches of truly normal white matter have been described, resulting in a scientific debate about whether abnormalities in connectivity are omnipresent (TSC as a connectopathy) or multifocal (TSC as a cortical dysplasia syndrome) [6]. Different imaging parameters and analysis techniques have hampered comparison across different institutions, but now a large, NIH-funded multicenter Autism Center of Excellence (ACE) study is acquiring prospective imaging and neuropsychological data in a goal sample of 150 patients with TSC in 5 US centers (clinicaltrials.gov: NCT01780441).

**Siemens disclaimer: MR scanning has not been established as safe for imaging fetuses and infants less than two years of age. The responsible physician must evaluate the benefits of the MR examination compared to those of other imaging procedures.

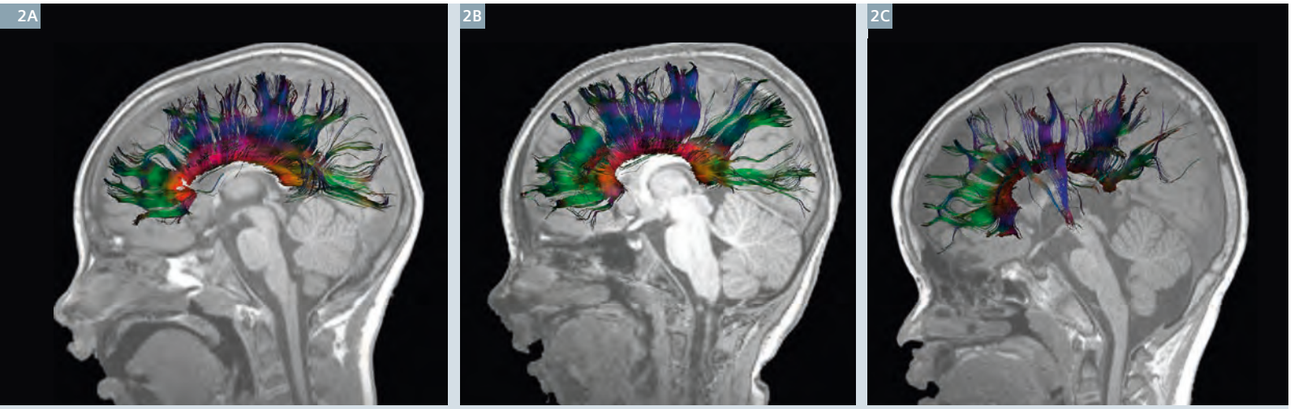

2 **Example of the relationship between diffusion measures and neurological phenotype in Tuberous Sclerosis Complex.** Three-dimensional projections of the corpus callosum are superimposed on sagittal T1-weighted MPRAGE images in three 5-year-old subjects: control **(2A)** FA 0.53; tuberous sclerosis without autism **(2B)** FA 0.54; tuberous sclerosis with autism **(2C)** FA 0.34. Images adapted from [18].

Early studies were limited by small sample size, poor magnet strength, or few diffusion directions, and were able to make comparisons between TSC patients and controls only in certain 2D defined areas of interest. Our group was the first to study a population sufficiently large enough to allow for correlation with neurological phenotype [18]. Using a 3T magnet, and 35 diffusion directions, with a stochastic tractography algorithm developed in-house, we analyzed 40 patients with TSC and 29 age-matched controls. The corpus callosum was analyzed, as it represents a major white matter tract and has been implicated in autism. To include all tracts of the 3-dimensional white matter structure, we introduced a novel analysis method[§] that adjusts for partial volume averaging in the calculation of DTI measures. On a group level, patients with TSC and autism had a higher MD and lower FA in the corpus callosum, as compared to patients with TSC without autism and as compared to controls (Fig. 2). This difference was seen early in the course of the developmental trajectory of white matter maturation. An extension of this work revealed that language pathways also differ in TSC patients with autism [19].

The relation between aberrant connectivity and the neurological and behavioral phenotype of TSC has also been demonstrated with other modalities. A globally reduced EEG connectivity was found in 42 patients with TSC, and network analysis showed an increased resilience to network disruption in patients with TSC and autism. The same was found in autism without TSC, suggesting a common mechanism, or at least validating the use of TSC as a model for autism spectrum disorders [20].

Epilepsy is refractory in over a third of patients with TSC, and infantile spasms or early onset refractory seizures may predict poor neurological outcome in TSC. In TSC, epileptogenic tubers have an increased MD and decreased FA as compared to silent tubers [21]. Whether this diffusion change is secondary to focal seizures (excitotoxic edema, axonal injury, maladaptive developmental changes, etc.) or represents the primary deficit in microstructural organization responsible for increased epileptogenicity is not yet clear. A relationship has been described between poorly controlled epilepsy and the predominance of poorly organized tubers. The study based tuber classification on conventional imaging findings, but an additional analysis of ADC values of the dominant tuber type was also performed. This showed differences in ADC values of the dominant tubers between the three epilepsy severity subgroups [22]. The prospective collection of serial imaging and EEG recordings combined with epilepsy and neuropsychological variables (ACE/P20-study) will provide an opportunity to further elucidate the relation between EEG markers, DTI measures and clinical epilepsy (clinicaltrials.gov: NCT01780441; NCT01767779).

Finally, everolimus and sirolimus are pharmacological inhibitors of the mTOR pathway, and almost directly target the molecular deficit of TSC. These drugs have demonstrated efficacy for multiple complications of TSC related lesions, including pulmonary lymphangioleiomyomatosis [23], renal angiomyolipoma [24], and SEGAs [25]. The imaging data from the SEGA study revealed a compelling improvement of NAWM in patients treated with mTOR inhibitors [26]. Preclinical data, case reports, and secondary outcome measures regarding seizures, cognition and behavior suggested beneficial effects of mTOR inhibitors, and have led to prospective, randomized, double blind and placebo controlled trials of the use of these drugs to improve epilepsy (EXIST-II and III) and neurocognition (NCT01289912). Given the relation between NAWM integrity and autism, and the report of improved NAWM DTI measures with the use of mTOR inhibitors, DTI can be considered a candidate biomarker in TSC. It will be critical to investigate whether DTI measures parallel the anticipated clinical changes in the abovementioned trials. If DTI indeed becomes a robust and biologically plausible biomarker, it will facilitate future trials through early patient stratification and quantitative assessment of treatment response.

[§] WIP, the product is currently under development and is not for sale in the US and other countries. Its future availability cannot be ensured.

Limitations of the single tensor model

The diffusion tensor model relies on the assumption that the water molecules in one voxel all follow the same diffusion process, and are equally constrained by the brain tissues. Each voxel, however, is subjected to the presence of heterogeneous fascicle orientations and partial volumes of different tissues [27]. In this section, we discuss these fundamental limitations of the diffusion tensor model to represent the brain microstructure.

Heterogeneous Fascicle Orientations
The DTI model assumes that, at each voxel, the diffusion is Gaussian with either no preferential direction (isotropic diffusion) or one preferential direction. This assumption is reasonable only when all axons in the voxel are aligned together and contained in one fascicle with a specific orientation. However, owing to the presence of complex fascicle organizations, heterogeneous fascicle orientations can be present in one voxel. In the corona radiata, for instance, corticospinal tracts (vertical tracts connecting the cortex to the spinal cord) cross fascicles of the corpus callosum (horizontal tracts connecting the left and right hemispheres) and the superior longitudinal fasciculus [27]. Recent studies estimate the prevalence of those heterogeneities to range between 60% and 90% of voxels in the white matter at typical DWI resolution [28]. When fascicles are crossing, interpretation of the DTI-based measures (MD and FA) is unreliable [29]. For instance, in the presence of two crossing fascicles, a single overly wide tensor would be estimated resulting in decreased FA. This decreased FA is not related to a property of the fascicle and, if interpreted this way and without knowledge of the underlying neuroanatomy, may incorrectly lead to the assumption that the myelination or microstructure is altered for that fascicle [30].

Partial Volume Effect
Voxels that are at the interface between different tissues (gray and white matter), between adjacent fiber bundles or between a tissue and cerebrospinal fluid (CSF) suffer another problem called *partial voluming*. The diffusion signal arising from protons in the different compartments (CSF, gray or white matter) will be averaged into a single value that is observed in DWI. Because DTI assumes that the diffusion of water molecules is either purely unrestricted or purely restricted within a single fascicle in the voxel, influences of different compartments will conflate, resulting in an inflated tensor with a lower FA [31]. As with heterogeneous fascicle orientations, this decreased FA may be misleadingly interpreted as altered myelin.

Even in voxels that are not at the interface between tissues, some fraction of the water molecules will diffuse in the extra-axonal space (either within other cells or in the extracellular lattice). Their diffusion process is different from the diffusion within axons and results in a different diffusion signal. The partial volume effect therefore also applies within a fascicle, between molecules inside and outside axons [32]. The partial volume effect is essentially a resolution limitation.

Multi-fascicle models

The problems related to heterogeneous fascicle orientations and partial voluming of other tissues may naturally be solved by providing different representations of the signal arising from water molecules in different compartments [31]. Such a representation is the gist of multi-fascicle models. Multi-fascicle models focus on modeling the signal arising from each important compartment. In particular, the diffusion signal is modeled as a mixture of sources of isotropic diffusion, and sources of diffusion in each fascicle, that are identified, modeled and parameterized. We have utilized a multi-fascicle model in which isotropic diffusion of extra-axonal water is modeled with one or more isotropic diffusion tensors (that is, diffusion tensors in which diffusion is the same in all directions), and one or more potentially anisotropic tensors (with anisotropy determined by the imaging data), modeling restricted and hindered diffusion associated with each fascicle.

Figure 3 illustrates the resolution of two crossing tracts with the single tensor model and a multi-fascicle model.

CUbe and SPhere (CUSP) imaging

The estimation of a multi-fascicle model from diffusion-weighted imaging poses additional challenges. When only DWI at a single non-zero b-value are available, the problem of estimating a multi-fascicle model is mathematically ill-posed [31, 33]. This means that an infinite number of models are equally compatible with the DWI measurements and none of these equivalent models can reliably be selected.

To reliably estimate a multi-fascicle model, diffusion-weighted imaging must be acquired at multiple different non-zero b-values to disambiguate the overlapping diffusion decay curves of each compartment. A popular acquisition to do so has been the multi-shell HARDI, which provides uniform angular coverage in q-space. A multi-shell HARDI, however, requires setting the nominal b-value to the largest imaged b-value, leading to a long duration echo time (TE) and therefore a low SNR due to T2 relaxation.

By contrast, Cube and Sphere (CUSP) imaging combines both spherical and cubic sampling in q-space, leading to a large number of non-zero b-values with short TE, high SNR and

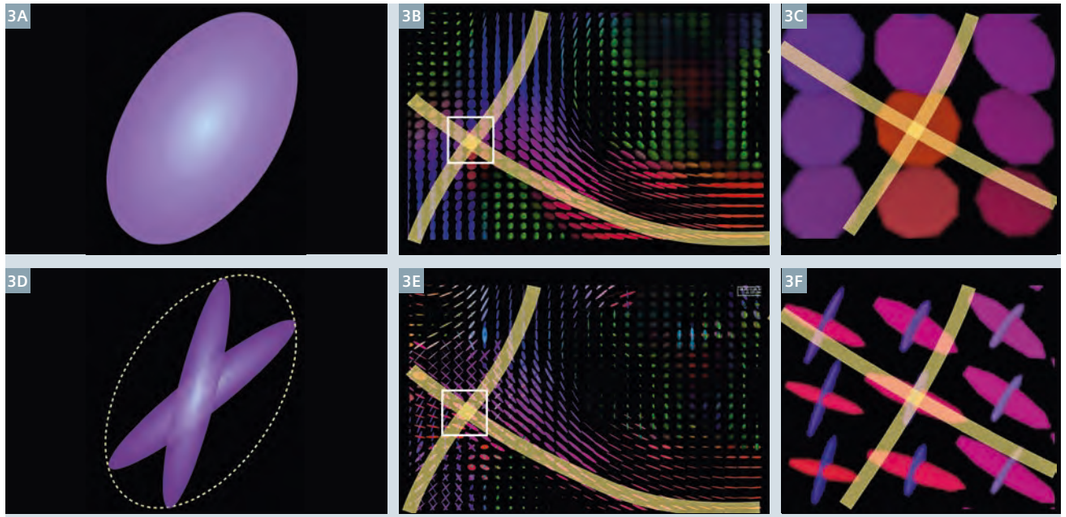

3 **Illustration of crossing fibers in the single tensor DTI model and in a multiple fascicle model. (3A–C)** The diffusion tensor imaging (DTI) model assumes that at most one fascicle is present within each voxel. This assumption does not hold in regions where fascicles cross, such as **(3B)** the corona radiata. In those regions, the DTI model results in abnormally inflated tensors that conflates the signal from each fascicle, resulting in an artificially lower fractional anisotropy that may lead to misinterpretations. In contrast, **(3D–F)** multi-fascicle models provide a separate representation for the signal arising from each fascicle and are, therefore, able to characterize and resolve regions with crossing fascicles. Modified from [7], with permission.

4

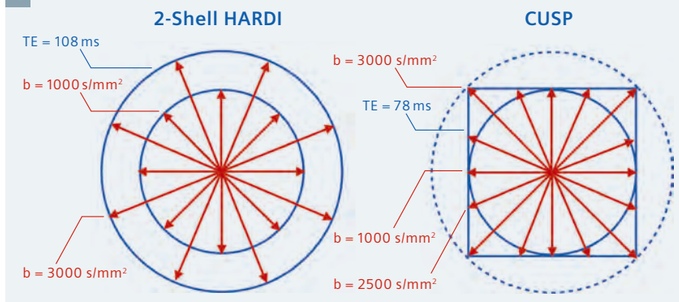

4 **CUbe and SPhere (CUSP) acquisition scheme.** In the 2-shell HARDI acquisition, DWI are acquired by setting gradients on two different spheres in q-space. In this acquisition scheme, the TE is determined by the outermost sphere, which leads to an overall decrease in SNR due to T2 decay. By contrast, in the CUSP acquisition scheme, the TE is determined by the innermost sphere and multiple b-values are achieved by setting extra gradients on the cube of constant TE, which achieve b-values up to three times larger than the b-values obtained on the sphere.

high angular coverage [31]. CUSP is based on the modification of a 2-shell HARDI. In contrast to a multi-shell HARDI, the pulse duration and separation, δ and Δ, of the PGSE sequence are fixed to achieve the b-value of the inner shell, which requires a shorter TE and provides a significant SNR boost. The gradients of the outer shell are reduced in strength to lie on the cube enclosing the inner shell. This cube is a cube of constant TE in q-space. Since the b-value is proportional to the squared norm of the encoding gradient and since gradients in the corner of the cube have a squared norm three times that of the gradient lying on the sphere, images with b-value up to three times the original (nominal) b-values can be achieved in CUSP, without modifying the TE (Fig. 4), and therefore without any cost in SNR.

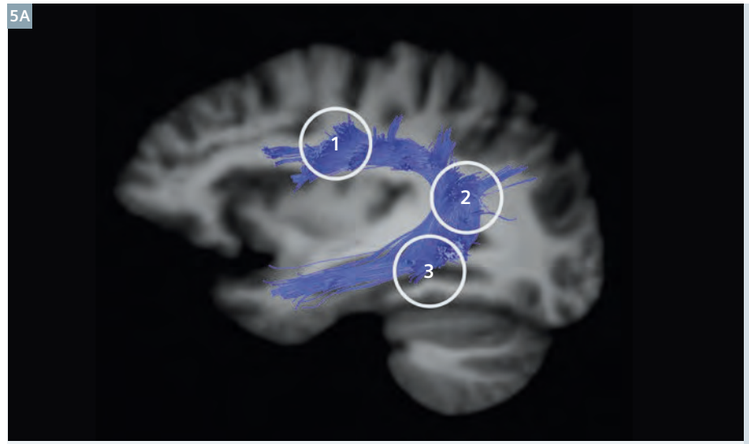

5 **Improved detection of group differences with the multi-fascicle model.**
(5A) The dorsal language network is thought to connect Broca's area in the frontal lobe, Geschwind's territory and Wernicke's area in the posterior temporo-parietal areas. Streamlines were selected based on passing through certain regions of interest (inclusion regions-of-interest (ROIs)), and excluded when passing through other regions (exclusion ROIs) using a method that has been previously validated for perisylvian language areas [36]. Rather than gray matter areas to define endpoints, we defined 3 regions in the white matter adjacent to Broca's, Wernicke's and Geswchind's territory as described in our earlier work [19].
(5B–D) Fascicle-based spatial statistics (FBSS) of multi-fascicle models reveal local differences in the fascicle properties that single tensor DTI cannot. Curves show the mean FA along the median tract of the dorsal language circuit in each group. Shaded areas along the curves represent two standard errors. Grey rectangles indicate regions where the FA is significantly different between the groups. The top row investigates differences between patients with tuberous sclerosis complex (TSC) and healthy controls. The bottom row further investigates differences between TSC patients with (TSC+ASD) and without autism (TSC-ASD).

Analyzing multi-fascicle models

Multi-fascicle models provide a variety of information about the brain microstructure. Each of the tensors representing a fascicle can be analyzed along a particular fascicle of interest using Fascicle-Based Spatial Statistics (FBSS) [34], enabling the identification of abnormalities or group differences that pertain to a particular fascicle. The statistical power is increased, allowing the detection of differences not visible with the single-tensor model (Fig. 5).

Furthermore, the isotropic diffusion of water molecules in the extra-axonal space can be analyzed separately using Isotropic Diffusion Analysis (IDA) [34]. The latter method enables the detection of an excess in the volume of water molecules that are freely diffusing, which is thought to indicate

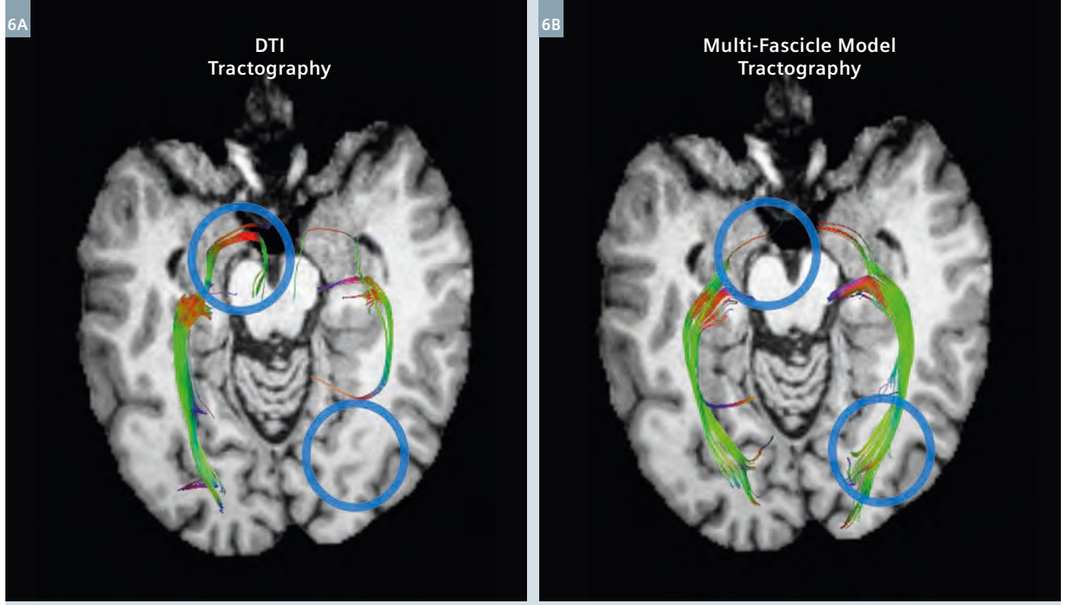

6 **DTI tractography and multiple fascicle model of the geniculocalcarine tracts, using a common region-of-interest (ROI) schema.** This white matter pathway links the lateral geniculate nucleus (LGN) of the thalamus to the occipital lobe via the stratum sagittal. The white matter adjacent to the LGN was used as a ROI for seeding tracts and the stratum sagittal waypoint was used as a selection ROI [37]. DTI tractography **(6A)** produced asymmetric tracts, which failed to reach the occipital lobe in the left hemisphere (posterior blue circles). Additionally, the fibers in the LGN are in an area of crossing fibers, resulting in tracts that extend far forward of the expected termination site (anterior blue circles). Multi-fascicle model tractography **(6B)** exhibits several key improvements. The tracts appear symmetric and reach the occipital lobe in both hemispheres. Though fibers in the LGN still extend forward, there is a sizeable reduction in the number of spurious streamlines and a much smaller angle of deviation between these fibers and those terminating in the LGN.

the presence of edema or neuroinflammation [35].

Figure 6 shows how the application of multiple-fascicle models to tractography can lead to the improved identification of fascicles, consistent with known anatomy.

Conclusions

Diffusion-weighted imaging allows for non-invasive probing of microstructural tissue properties, and may directly represent underlying neuropathology in tuberous sclerosis complex. Moreover, preliminary evidence suggests diffusion abnormalities in the normal appearing white matter (NAWM) correspond to the neurological phenotype in TSC. Changes in white matter diffusion have been reported in patients treated with mTOR inhibitors [26], but whether such changes parallel clinical improvements in cognition, autism and epilepsy requires further study.

Single tensor models are limited by partial volume effects and cannot resolve crossing fibers. Multi-fascicle models address these limitations by modeling isotropic and anisotropic diffusion sources arising from each fascicle present at each voxel. However, single shell HARDI provides insufficient imaging data to identify the signal from each fascicle. More than two b-value diffusion images must be acquired in order to find all the parameters of a multi-fascicle model. CUSP imaging provides multiple non-zero b-values at high SNR. As the multiple-fascicle model better explains the diffusion signal, group differences can be more reliably detected and complex fiber streamlines modeled more accurately.

As white matter integrity in TSC may parallel neurological symptoms, and improves with treatment, the current developments in multiple fascicle models can further the potential for diffusion imaging to become a reliable biomarker in TSC.

References

1 Curatolo P, Bombardieri R, Jozwiak S. Tuberous sclerosis. Lancet. 2008; 372(9639):657–668.
2 Jansen FE, Vincken KL, Algra A, et al. Cognitive impairment in tuberous sclerosis complex is a multifactorial condition. Neurology. 2008;70(12):916–923.
3 Numis AL, Major P, Montenegro MA, Muzykewicz DA, Pulsifer MB, Thiele EA. Identification of risk factors for autism spectrum disorders in tuberous sclerosis complex. Neurology. 2011;76(11):981–987.
4 Jozwiak S, Kotulska K, Domanska-Pakiela D, et al. Antiepileptic treatment before the onset of seizures reduces epilepsy severity and risk of mental retardation in infants with tuberous sclerosis complex. Eur J Paediatr Neurol. 2011;15(5):424–431.
5 Bombardieri R, Pinci M, Moavero R, Cerminara C, Curatolo P. Early control of seizures improves long-term outcome in children with tuberous sclerosis complex. Eur J Paediatr Neurol. 2010;14(2):146–149.
6 Van Eeghen AM, Teran LO, Johnson J, Pulsifer MB, Thiele EA, Caruso P. The neuroanatomical phenotype of tuberous sclerosis complex: focus on radial migration lines. Neuroradiology. 2013;55(8):1007-14.
7 Peters JM, Taquet M, Prohl AK, et al. Diffusion tensor imaging and related techniques in tuberous sclerosis complex: review and future directions. Future Neurol. 2013 Sep 28;8(5):583–597.
8 Tsai P, Sahin M. Mechanisms of neurocognitive dysfunction and therapeutic considerations in tuberous sclerosis complex. Curr Opin Neurol. 2011;24(2):106–113.
9 Meikle L, Talos DM, Onda H, et al. A mouse model of tuberous sclerosis: neuronal loss of Tsc1 causes dysplastic and ectopic neurons, reduced myelination, seizure activity, and limited survival. J Neurosci. 2007;27(21):5546–5558.
10 Nie D, Di Nardo A, Han JM, et al. Tsc2-Rheb signaling regulates EphA-mediated axon guidance. Nat Neurosci. 2010;13(2): 163–172.
11 Choi YJ, Di Nardo A, Kramvis I, et al. Tuberous sclerosis complex proteins control axon formation. Genes Dev. 2008;22(18): 2485–2495.
12 Marcotte L, Aronica E, Baybis M, Crino PB. Cytoarchitectural alterations are widespread in cerebral cortex in tuberous sclerosis complex. Acta Neuropathol. 2012; 123(5):685–693.
13 Ma TS, Elliott RE, Ruppe V, et al. Electro corticographic evidence of perituberal cortex epileptogenicity in tuberous sclerosis complex. J Neurosurg Pediatr. 2012; 10(5):376–382.
14 Major P, Rakowski S, Simon M V, et al. Are cortical tubers epileptogenic? Evidence from electrocorticography. Epilepsia. 2009;50(1):147–154.
15 Geschwind DH, Levitt P. Autism spectrum disorders: developmental disconnection syndromes. Curr Opin Neurobiol. 2007; 17(1):103–111.
16 Minshew NJ, Williams DL. The new neurobiology of autism: cortex, connectivity, and neuronal organization. Arch Neurol. 2007;64(7):945–950.
17 Sener RN. Tuberous sclerosis: diffusion MRI findings in the brain. Eur Radiol. 2002;12(1):138–143.
18 Peters JM, Sahin M, Vogel-Farley VK, et al. Loss of white matter microstructural integrity is associated with adverse neurological outcome in tuberous sclerosis complex. Acad Radiol. 2012;19(1):17–25.
19 Lewis WW, Sahin M, Scherrer B, et al. Impaired Language Pathways in Tuberous Sclerosis Complex Patients with Autism Spectrum Disorders. Cereb Cortex. 2013;23(7):1526-32.
20 Peters JM, Taquet M, Vega C, et al. Brain functional networks in syndromic and non-syndromic autism: a graph theoretical study of EEG connectivity. BMC Med. 2013;11(1):54.
21 Jansen FE, Braun KP, van Nieuwenhuizen O, et al. Diffusion-weighted magnetic resonance imaging and identification of the epileptogenic tuber in patients with tuberous sclerosis. Arch Neurol. 2003; 60(11):1580–1584.
22 Gallagher A, Grant EP, Madan N, Jarrett DY, Lyczkowski DA, Thiele EA. MRI findings reveal three different types of tubers in patients with tuberous sclerosis complex. J Neurol. 2010;257(8): 1373–1381.
23 McCormack FX, Inoue Y, Moss J, et al. Efficacy and safety of sirolimus in lymphangioleiomyomatosis. N Engl J Med. 2011;364(17):1595–1606.
24 Bissler JJ, Kingswood JC, Radzikowska E, et al. Everolimus for angiomyolipoma associated with tuberous sclerosis complex or sporadic lymphangioleiomyomatosis (EXIST-2): a multicentre, randomised, double-blind, placebo-controlled trial. Lancet. 2013; 381(9869):817–824.
25 Krueger DA, Care MM, Holland K, et al. Everolimus for subependymal giant-cell astrocytomas in tuberous sclerosis. N Engl J Med. 363(19):1801–1811.
26 Tillema JM, Leach JL, Krueger DA, Franz DN. Everolimus alters white matter diffusion in tuberous sclerosis complex. Neurology. 2012;78(8):526–531.
27 Tournier JD, Mori S, Leemans A. Diffusion tensor imaging and beyond. Magn Reson Med. 2011;65(6): 1532–1556.
28 Jeurissen B, Leemans A, Tournier JD, Jones DK, Sijbers J. Investigating the prevalence of complex fiber configurations in white matter tissue with diffusion magnetic resonance imaging. Hum Brain Mapp. 2013;34(11):2747-66.
29 Vos SB, Jones DK, Jeurissen B, Viergever MA, Leemans A. The influence of complex white matter architecture on the mean diffusivity in diffusion tensor MRI of the human brain. Neuroimage. 2011;59(3):2208–2216.
30 Douaud G, Jbabdi S, Behrens TEJ, et al. DTI measures in crossing-fibre areas: increased diffusion anisotropy reveals early white matter alteration in MCI and mild Alzheimer's disease. Neuroimage. 2011;55(3):880–890.
31 Scherrer B, Warfield SK. Parametric representation of multiple white matter fascicles from cube and sphere diffusion MRI. PLoS One. 2012; 7(11):e48232.
32 Scherrer B, Schwartzman A, Taquet M, et al. Characterizing the DIstribution of Anisotropic MicrO-structural eNvironments with Diffusion-weighted imaging (DIAMOND). Proc 16th Int Conf Med Image Comput Comput Assist Interv. 2013. p. 518–526.
33 Taquet M, Scherrer B, Boumal N, Macq B, Warfield SK. Estimation of a Multi-Fascicle Model from Single B-Value Data with a Population-Informed Prior. Med Image Comput Comput Interv MICCAI. 2013.
34 Taquet M, Scherrer B, Commowick O, et al. A Mathematical Framework for the Registration and Analysis of Multi-Fascicle Models for Population Studies of the Brain Microstructure. Med Imaging, IEEE Trans. 2013, in press.
35 Pasternak O, Westin CF, Bouix S, et al. Excessive extracellular volume reveals a neurodegenerative pattern in schizophrenia onset. J Neurosci. 2012/12/01 ed. 2012;32(48):17365–17372.
36 Catani M, Jones DK, ffytche DH. Perisylvian language networks of the human brain. Ann Neurol. 2005 Jan;57(1):8–16.
37 Benjamin CFA, Singh JM, Prabhu SP, Warfield SK. Optimization of tractography of the optic radiations. Hum Brain Mapp. 2014 Feb;35(2):683–697.

Jurriaan M. Peters, M.D.

Maxime Taquet, Ph.D.

Contact

Correspondence Tuberous Sclerosis Complex:
Jurriaan M. Peters, M.D.
Division of Epilepsy
and Clinical Neurophysiology
Boston Children's Hospital
300 Longwood Ave – Fegan9
Boston, MA 02115
USA
Phone: +1 617 355 5606
Fax: +1 617 730 0463
jurriaan.peters@childrens.harvard.edu

Correspondence image acquisition, multi-fascicle models:
Maxime Taquet, Ph.D.
Computational Radiology Laboratory,
Department of Radiology
Boston Children's Hospital
300 Longwood Ave – Main2
Boston, MA 02115
USA
Phone: +1 857 218 5172
Fax: +1 617 730 4644
maxime.taquet@childrens.harvard.edu

Advanced Diffusion and Spectroscopic MR Applied to Autism

Jeffrey Berman, Ph.D.; William Gaetz, Ph.D.; Timothy Roberts, Ph.D.

Children's Hospital of Philadelphia, Department of Radiology, Philadelphia, PA, USA

Overview

Children with autism spectrum disorder (ASD) typically present with a number of symptoms, including poor social skills, impaired communication and language skills, and stereotypic behaviors. There is no known structural, functional, or genetic abnormality that singularly causes autism. However, there is increasing evidence of alterations to the brain's anatomy and physiology which may be linked to the symptoms of autism. In terms of brain abnormalities, there is evidence of altered white matter structure and abnormal cortical activity [1, 2]. Specifically, delayed auditory evoked cortical response latencies have been observed with magnetoencephalography (MEG) in ASD [3]. A primary goal of our research center is to examine the auditory radiation and auditory cortex, as functional and structural abnormalities of the auditory system are associated with autism spectrum disorders (ASD). Given that there is not a singular cause of ASD, it is advantageous to assess multiple structural and chemical biomarkers to better understand the biological basis of autism and dysfunction of the auditory system.

Our laboratory uses diffusion-weighted MRI and GABA MR spectroscopy to examine the microstructure and chemical environment in the auditory system. The combination of diffusion and spectroscopic MR provides a window into the structural and neurochemical abnormalities in ASD. This review will outline our imaging methods, post processing strategy, initial results and future outlook.

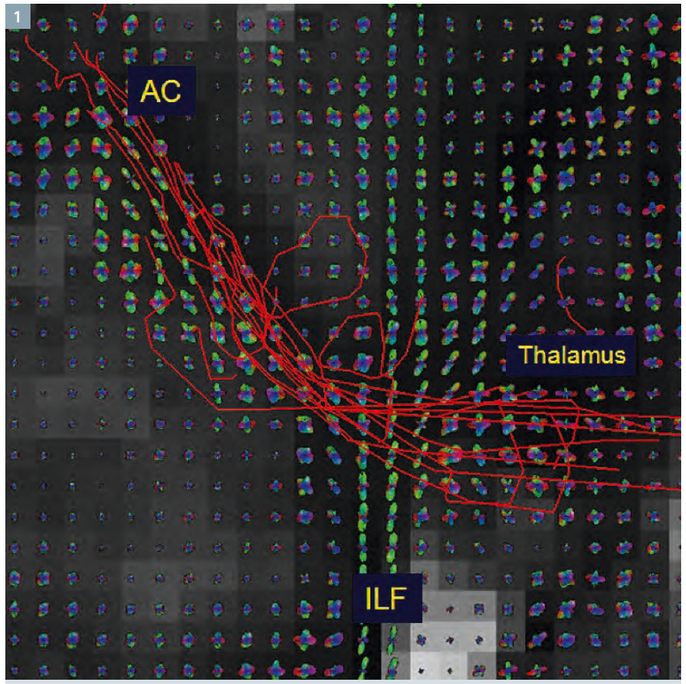

1 HARDI probabalistic fiber tracking of the auditory radiation from the auditory cortex (AC) to the thalamus. The fiber tracks are the red streamlines. The underlying HARDI reconstructrions are shown. The inferior longitudinal fasciculus (ILF) intersects the auditory radiation and is visible within the HARDI reconstructions as green peaks.

Background

Water in the brain undergoes constant Brownian motion. Diffusion MR uses this random motion of water as a probe for the presence of barriers to mobility of water. The 3D pattern of water diffusion can be used to infer brain tissue architecture, microstructure, and orientation of coherent axonal bundles [4]. Diffusion fiber tracking can be used to delineate specific white matter pathways in 3D by following the estimated fiber orientation from voxel to voxel [5]. Diffusion tensor imaging (DTI) has become the clinical standard for acquiring diffusion-weighted images and modeling tissue microstructure. DTI can be acquired with a minimum of 6 gradient directions and DTI fiber tracking is commercially available. A limitation, however, is that the diffusion tensor model fails to accurately represent the complex architecture of crossing white matter fibers. For this reason, DTI fiber tracking fails to accurately follow white matter pathways through tract intersections. One such pathway is the auditory radiation, which intersects other white matter tracts coursing anterior-posterior. The auditory radiations are an important sensory pathway which relays acoustic information from the medial geniculate nucleus of the thalamus to primary auditory cortex and its conduction velocity could be hypothesized to mediate in part cortical response time. Although the auditory radiation is a functionally important sensory input pathway, it cannot be reliably examined with DTI.

High angular resolution diffusion imaging (HARDI) is capable of discriminating multiple fiber populations crossing within the same voxel [6]. HARDI requires the acquisition of over 50 gradient directions at typically high b-values, while DTI only requires 6 directions at lower b-values. The higher angular resolution provides a more accurate representation of the 3D pattern of water diffusion within a voxel. Fiber tracking with HARDI can follow white matter tracts through regions of crossing fibers whereas DTI fiber tracking would terminate or provide erroneous results in these same areas. This project uses HARDI fiber tracking to robustly delineate the complex architecture of the auditory radiation.

White matter structural abnormalities are not the only potential mechanism for auditory latency delays; latency delays could be produced by synaptic and/or local circuit dysfunction. The concept of synaptic/local circuit dysfunction has been posited as a pathogenic mechanism for ASD, arising from an imbalance of excitation and inhibition. Altered inhibitory cell count, cell intrinsic excitability, network excitability and lower seizure thresholds have all been demonstrated in animal models that recapitulate key phenotypes of ASD. GABA is a neurotransmitter with an inhibitory function which regulates the oscillatory behavior of local circuitry comprising inhibitory interneurons and excitatory pyramidal neurons. Prior studies have indicated GABAergic dysfunction in autism [7]. Our center has used GABA spectroscopy to examine chemical abnormalities in the synapses of the auditory system.

Proton magnetic resonance spectroscopy (MRS) is capable of estimating the concentrations of specific metabolites and neurotransmitters. MRS can be performed within a defined region-of-interest to provide spatially-specific spectra. MEGA-PRESS is a spectral editing technique which allows GABA to be separated from overlapping metabolites, particularly creatine [8]. MEGA-PRESS subtracts two spectra with different evolutions of the J-coupled GABA CH2 resonance.

Table 1: Imaging protocols

Sequence	Duration	Measure
Scout (localizer)	1 min	–
MPRAGE (1 mm isotropic)	8 min	–
HARDI (64 direction, b = 3000 s/mm², 2 mm isotropic resolution) reconstruction using solid angle q-ball model, and probabilistic tractography to reconstruct acoustic radiations	16 min	**FA, MD, GFA, and eigenvalues** integrated along acoustic radiation
MEGA-PRESS – 128 paired transients, TE 68 ms, 40 × 30 × 20 mm single voxel placed in right and left hemisphere STG	2 × 7 min	**GABA+/Cr**

Practical implementation

Platform

Imaging is performed on a 3T Siemens MAGNETOM Verio (software version *syngo* MR B17), dedicated to research, using a 32-channel receive only head RF coil. A 3D MPRAGE anatomic scan is routinely obtained axially with FOV 256 × 256 × 192 mm and matrix 256 × 256 × 192 to yield 1 mm isotropic resolution, TR 1900 ms, TE 2.9 ms, TI 1100 ms, flip angle 9°.

Diffusion MR

HARDI acquisition includes 64 diffusion gradient directions at b=3000 s/mm², TR 16.9 s, TE 110 ms, parallel acceleration 2, voxel size 2 × 2 × 2 mm, and acquisition time of approximately 16 min. This scan has proven feasible in children 6 –15 years old (success rate > 80%). For comparison, a standard DTI acquisition includes 30 gradient directions at b=1000 s/mm², TR 14 s, TE 75 ms, and voxel size 2 × 2 × 2 mm. The DTI data is similar to the diffusion sequence used routinely in clinical practice. Both acquisitions use the 511C works in progress (WIP) spin-echo echo planar sequence* with monopolar Stejskal-Tanner diffusion encoding scheme and a parallel acceleration factor of 2. The solid angle q-ball reconstruction is used with a probabilistic HARDI fiber tracking algorithm. The q-ball reconstruction of HARDI has been chosen because it does not rely on a model and the recently developed solid angle correction provides an accurate estimate of the orientation distribution function (ODF). The fiber tracking algorithm uses the residual bootstrap to estimate the uncertainty in the orientation distribution function.

*Work in progress. The product is still under development and not commercially available in the US and in other countries yet. Its future availability cannot be ensured.

**Siemens disclaimer: MR scanning has not been established as safe for imaging fetuses and infants less than two years of age. The responsible physician must evaluate the benefits of the MR examination compared to those of other imaging procedures.

2

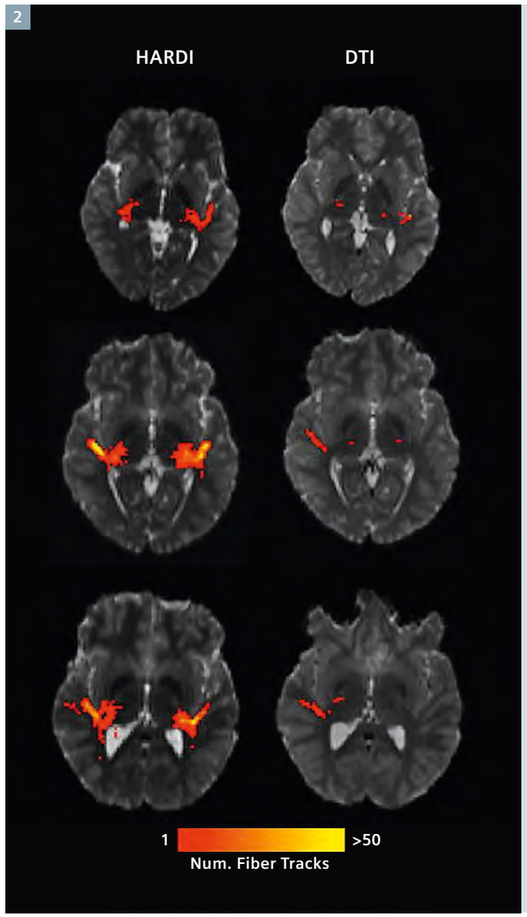

2

HARDI and DTI fiber tracking of the auditory radiation are shown in 3 subjects. DTI fiber tracking is not able to robustly delineate the pathway from the thalamus to the auditory cortex.

3

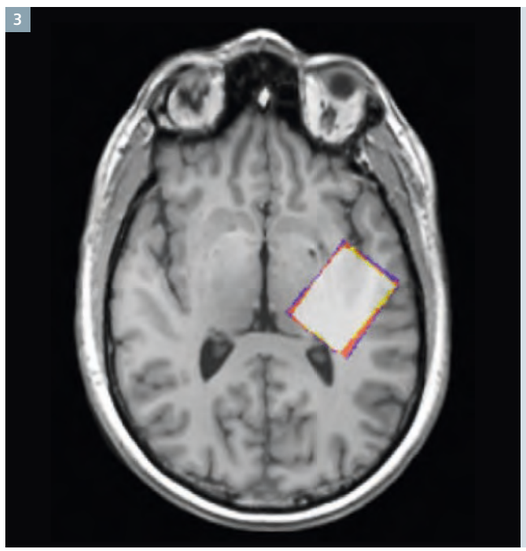

3

The region-of-interest over the auditory cortex for MEGA-PRESS magnetic resonance spectroscopy.

Spectroscopic imaging

Single voxel (40 × 30 × 20 mm) MRS is obtained using the MEGA-PRESS spectral editing sequence, with TE 68 ms (< 7 min). The Siemens work-in-progress package (#529) is used*. MRS voxels are centered on the superior temporal gyrus. In the coronal plane, voxels are rotated to best match adjacent scalp surface and avoid CSF/bone/fat contamination. Local high-order shimming provides FWHM linewidths < 10 Hz for the unsuppressed water peak. After Fourier transformation, phase correction is applied to the unsubtracted creatine (Cr) resonance. The integral under the GABA resonance (at 3 ppm) is obtained by spectral peak-fitting using a (pseudo-) doublet Gaussian resonance. GABA levels are estimated with respect to the unsubtracted Cr resonance (averaged over both raw transients) and reported as GABA+/Cr. The measurement is notated as 'GABA+' to indicate the known contributions from other macromolecules in the MEGA-PRESS experiment.

Results

HARDI

Figure 1 shows an example set of HARDI fiber tracks (red streamlines) crossing the inferior longitudinal fasciculus (ILF) and connecting the auditory cortex (AC) to the thalamus. The q-ball orientation density functions show the crossing anterior-posterior ILF (green peaks) and the smaller left-right peaks representing the auditory radiation. HARDI fiber tracking successfully delineated the auditory radiation at a rate of 98% which was significantly higher than the 50% success rate of DTI fiber tracking ($p < 0.001$)[9]. The success rate of 30-direction and 64-direction DTI fiber tracking were not significantly different from each other. The success rates of HARDI fiber tracking for the left and right hemisphere auditory radiations were not significantly different. In contrast, the left auditory radiation was successfully delineated with DTI fiber tracking at a higher rate than the right auditory radiation ($p < 0.03$). The effect of hemisphere on DTI fiber performance tracking indicates a possible difference in the level of fiber crossings between the left and right hemispheres.

The DTI cases classified as successful often contained very few fiber trajectories which did not accurately delineate the entire volume of the acoustic radiation. DTI fiber tracks tended to emerge from Heschl's gyrus and incorrectly follow the dominant anterior-posterior coursing ILF. HARDI data can reliably delineate the entire auditory radiation and enables tract-specific measurements not feasible with standard DTI techniques.

GABA

Regional alterations in GABA concentration were detected in ASD using single-voxel MEGA-PRESS magnetic resonance spectroscopy (MRS)[10]. The study included 13 children with ASD and 11 age matched typically developing children. GABA+/Cr ratios obtained from single voxels in the superior temporal gyrus of children with ASD are significantly reduced compared to age-matched TD controls ($p < 0.01$). Significant deficiency of GABA was also detected in the central sulcus (motor) ($p < 0.05$), but not the visual cortex. The GABA levels in ASD were 22% lower in the auditory system, and 11% lower in the motor system.

Future outlook

Our advanced imaging results in ASD demonstrate the feasibility of using spectroscopic and diffusion MR to assess the auditory system in ASD. Diffusion methods such as HARDI enable reliable quantitative measures of the auditory radiation. HARDI can discriminate the complex white matter pathways at the junction of the auditory radiation and the inferior longitudinal fasciculus. Future studies in ASD will utilize HARDI to perform a detailed assessment of the auditory system's microstructure and geometry. The HARDI acquisition is significantly longer than a conventional DTI sequence. However, slice accelerated single shot spin-echo echo-planar sequences can significantly decrease HARDI acquisition times, enabling integration of HARDI into a routine clinical sequence [11]. Figure 6 demonstrates the feasibility of using a 9 minute slice-accelerated sequence to perform HARDI tractography of the auditory radiation.

GABA levels in the auditory system were observed to be significantly

4

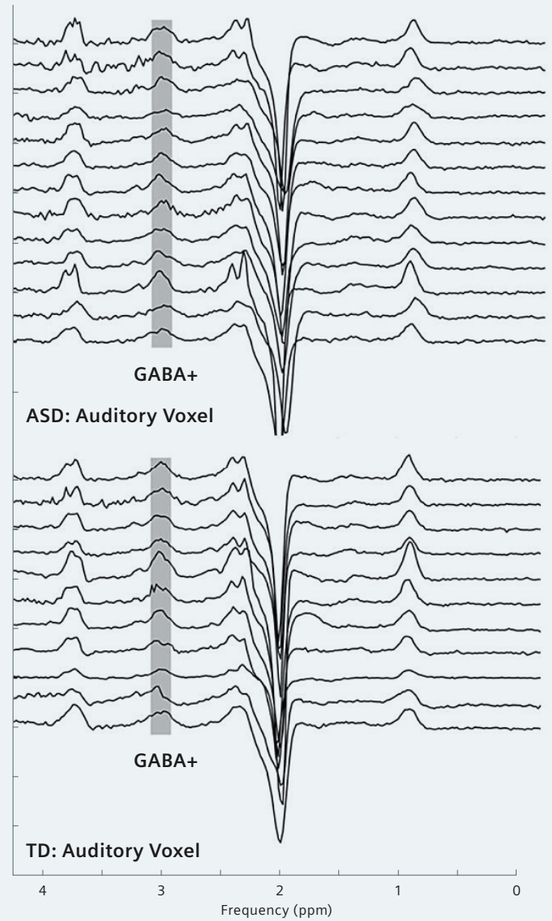

4 Stacked MEGA-PRESS spectra are shown for all Auditory ROI measures (N = 13 ASD, N = 11 TD). The GABA peak at 3 ppm is within the gray bar.

5

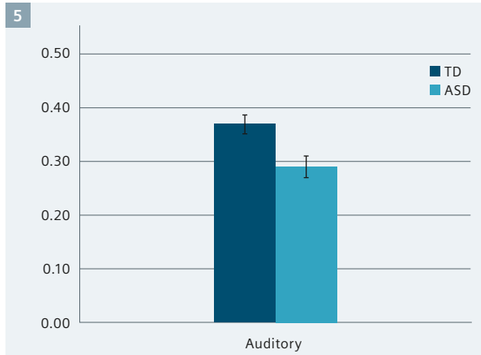

5

GABA+/Cr ratios were significantly reduced in the Auditory ROI in subjects with ASD ($p < 0.01$).

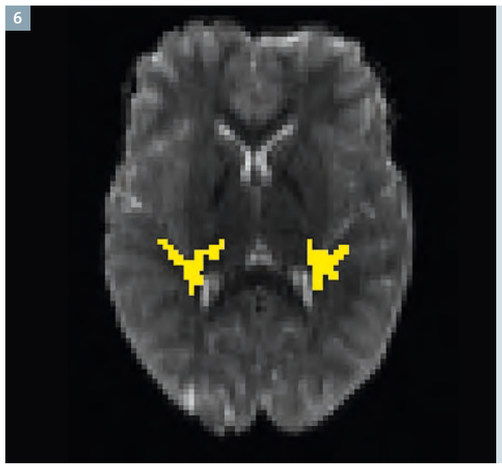

6

HARDI fiber-tracking of the auditory radiation using slice accelerated diffusion acquisition with b = 3000 s/mm², 64 gradient directions, and acquisition time of under 10 minutes.

lower in ASD. This alteration of the brain's chemistry may cause auditory dysfunction in ASD, such as the delayed auditory evoked response. Over the last several months we have worked to develop methods that provide optimal measures of auditory cortex GABA. In particular, although the methodologies proposed represent the state-of-the-art in clinical application of GABA assessment, a relevant potential confound exists in signal contamination from co-edited macromolecules (MM). Future technical developments may further eliminate the contribution from these macromolecules.

Functional and structural abnormalities of the auditory system can be assessed with MRS and diffusion MR. By examining anatomical and physiological aspects of the auditory system, we seek to expand our understanding of the biological basis of autism. We also anticipate that the methods described in this review can also be applied to other neuropsychiatric disorders.

Acknowledgements

We gratefully acknowledge the authors of the GABA spectral editing WIP 529, Dr. Keith Heberlein and Dr. Mark A. Brown. We also gratefully acknowledge the author of the diffusion WIP 511, Dr. Thorsten Feiweier. In addition, we acknowledge the support of Dr. Tiejun Zhao.

References

1 Redcay E, Courchesne E. When Is the Brain Enlarged in Autism? A Meta-Analysis of All Brain Size Reports. Biological Psychiatry 2005;58:1-9.
2 Lee JE, Bigler ED, Alexander AL, et al. Diffusion tensor imaging of white matter in the superior temporal gyrus and temporal stem in autism. Neuroscience Letters 2007;424:127-132.
3 Roberts TPL, Khan SY, Rey M, et al. MEG detection of delayed auditory evoked responses in autism spectrum disorders: towards an imaging biomarker for autism. Autism Research 2010;3:8-18.
4 Basser PJ, Pierpaoli C. A simplified method to measure the diffusion tensor from seven MR images. Magn Reson Med 1998;39: 928-934.
5 Mukherjee P, Berman JI, Chung SW, et al. Diffusion tensor MR imaging and fiber tractography: theoretic underpinnings. AJNR Am J Neuroradiol 2008;29:632-641.
6 Tuch DS. Q-ball imaging. Magn Reson Med 2004;52:1358-1372.
7 Pizzarelli R, Cherubini E. Alterations of GABAergic signaling in autism spectrum disorders. Neural plasticity 2011;2011: 297153.
8 Mescher M, Merkle H, Kirsch J, et al. Simultaneous in vivo spectral editing and water suppression. NMR Biomed 1998; 11:266-272.
9 Berman J, Lanza M, Blaskey L, et al. High Angular Resolution Diffusion Imaging Probabilistic Tractography of the Auditory Radiation. American Journal of Neuroradiology 2013.
10 Gaetz W, Bloy L, Wang DJ, et al. GABA estimation in the brains of children on the autism spectrum: Measurement precision and regional cortical variation. Neuroimage 2014;86:1-9.
11 Xu J, Moeller S, Auerbach EJ, et al. Evaluation of slice accelerations using multiband echo planar imaging at 3.0;T. NeuroImage 2013;83:991-1001.

Contact

Jeffrey Berman, Ph.D.
Children's Hospital of Philadelphia
Department of Radiology
3401 Civic Center Blvd,
Philadelphia, PA 19104
USA
BermanJ@email.chop.edu

RESOLVE: A Powerful Tool for Imaging the Pediatric Spine

Laura L. Hayes[1]; David A. Porter[2]; Richard A. Jones[1, 3]; Susan Palasis[1]; J. Damien Grattan-Smith[1]

[1]Department of Radiology, Children's Healthcare of Atlanta at Scottish Rite, Atlanta, GA, USA
[2]Siemens AG, Healthcare Sector, Erlangen, Germany
[3]Department of Radiology, Emory University, Atlanta, GA, USA

Introduction

Diffusion-weighted imaging (DWI) is one of the most powerful imaging tools available to radiologists today. DWI of the brain revolutionized neuroimaging when it was introduced in the mid-1990s. Until recently, clinically useful DWI of the spine has not been possible using standard single shot EPI techniques due to susceptibility artifacts and the need for higher spatial resolution. The novel 2D-navigator-corrected readout-segmented EPI sequence known as RESOLVE (REadout Segmentation Of Long Variable Echo trains) can obtain images with higher spatial resolution and reduced distortion of the spine related to susceptibility, pulsations, respiration, and motion [1]. This is especially helpful when imaging children where the small size of their spine/cord, prominent CSF and arterial pulsations, and higher pulse and respiratory rates compared to adults can pose significant limitations on the quality of the images obtained. Motion artifacts that notoriously plague every facet of pediatric imaging are also reduced with RESOLVE. RESOLVE is proving to be a valuable sequence for the evaluation of numerous pathological states of the pediatric spine.

Sequence description

RESOLVE [1, 2] is a multi-shot, diffusion-weighted sequence, which is based on the readout-segmented echo-planar imaging (rs-EPI) sampling scheme [3]. The sequence incorporates a 2D non-linear correction for motion-induced phase errors [4] and supports iPAT using GRAPPA [5]. The rs-EPI method only samples a subset of raw data points in the readout direction, making it possible to use a very short EPI echo spacing with a typical value of 360 µs. This is significantly shorter than the echo spacing used for single-shot EPI (ss-EPI), which reduces the level of susceptibility and blurring artifacts and makes it possible to acquire images with a higher spatial resolution.

In general, multi-shot, diffusion-weighted sequences are susceptible to image artifacts that arise from motion during the diffusion preparation, resulting in shot-to-shot phase errors. Navigator phase correction [6, 7] can address this problem by sampling data from the center of *k*-space at each shot; these data are then used to monitor and correct the phase variation between shots. CSF pulsation around the brain and spinal cord causes non-rigid-body motion, resulting in a 2D non-linear phase variation in image space, which requires 2D navigator data to perform a correction [4]. The rs-EPI sampling scheme is particularly well-suited to this type of correction because, unlike the more commonly used interleaved EPI sequence, the Nyquist sampling condition is fulfilled at each shot and there are no aliased signal contributions in the image domain to interfere with the phase correction procedure.

As shown in figure 1, following a spin excitation and diffusion preparation, the RESOLVE sequence uses two EPI readouts to acquire data from two spin echoes respectively at each shot. The first spin echo is used to sample a region of *k*-space, known as a readout segment, in which contiguous data samples are collected for all phase-encoding (k_y) points and for a subset of readout (k_x) points. A variable pre-phase gradient is applied along the readout (*x*) axis before the EPI readout to control an offset along k_x, so that a different readout segment is sampled at each shot. As shown in the *k*-space trajectory in figure 2, data from multiple readout segments are combined to provide full *k*-space coverage; typical protocols require 5, 7 or 9 shots to acquire the full data set, depending on the spatial resolution. The second spin echo shown in figure 1 is used to sample the central readout segment at each shot, thereby providing data for the 2D non-linear navigator correction. This is performed as a complex multiplication in the image domain before the data from the individual segments are combined to form the final image.

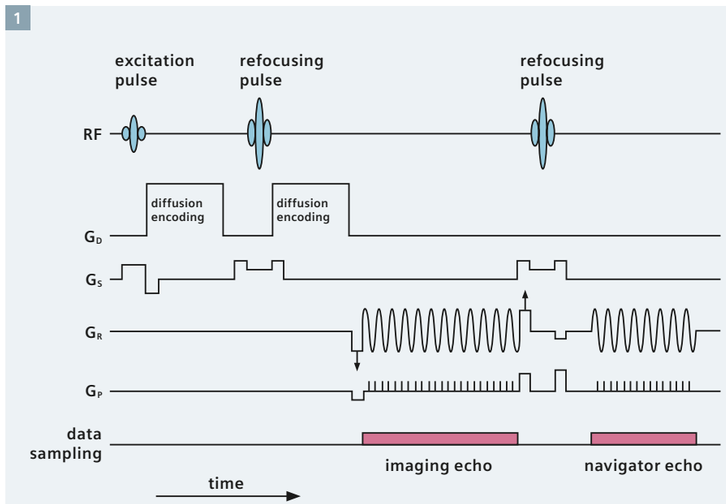

1 Pulse diagram for the RESOLVE sequence. The figure shows radiofrequency (RF) pulses and magnetic field gradient pulses for diffusion-encoding (G_D) and for spatial encoding along slice (G_S), readout (G_R) and phase-encoding (G_P) directions. The gradients with the ↑ symbol have an amplitude that is varied at each spin excitation to control an offset in the k_x direction, so that a different readout segment is sampled by the imaging echo at each shot. In contrast, the navigator echo always samples a fixed 2D region at the centre of *k*-space.

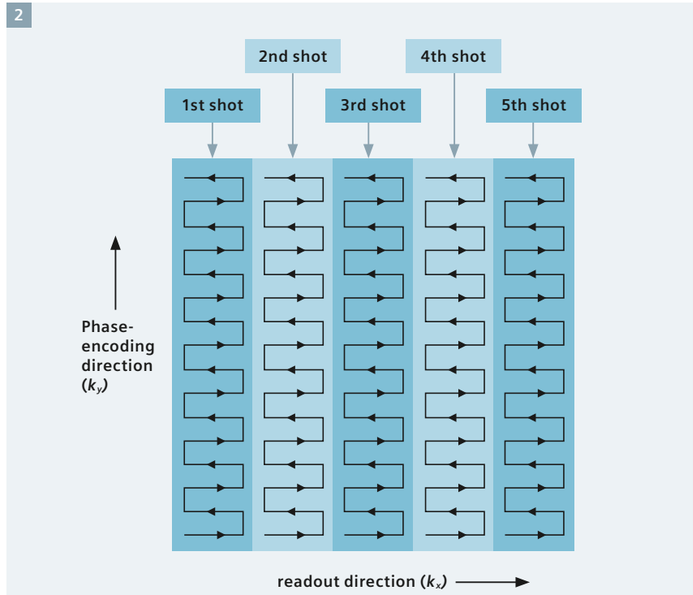

2 Diagram showing the *k*-space sampling scheme used for the imaging echo in the RESOLVE sequence. In this example, a five shot acquisition is used which divides *k*-space into five segments along the readout direction. Within each shot, an EPI readout is used to sample all phase-encoding (k_y) points and a subset of readout (k_x) points. The second (navigator) echo is always used to sample the central readout segment, providing 2D reference data from the center of *k*-space, which are used to perform a non-linear phase correction.

To further reduce the effect of motion-induced phase errors, the RESOLVE sequence uses a reacquisition scheme [8], which has been adapted to the case of a 2D navigator [9]. This ensures that readout segments with severe phase errors, which cannot be removed by the 2D navigator correction, are discarded and replaced by reacquired data.

Currently useful applications:
1. Tumor
a. Intradural
i. Drop metastases

DWI of the brain has revolutionized the sensitivity of MR in diagnosis, staging, and follow-up of children with central nervous system (CNS) tumors [10]. Likewise DWI of the spine is demonstrating the ability to reveal spinal disease that may not be visible on conventional MR sequences in children with primary brain tumors [11] (Figs. 3–5). Many of the primary CNS tumors that metastasize to the spine have a hypercellular tumor matrix. Primitive neuro-ectodermal tumors (PNETs) consist of small, round cells with scanty cytoplasm and have an extremely high cellular density with a high nuclear-to-cytoplasmic index. The total water content of these tumors is low, and their densely packed cellular nature results in restricted diffusion. The physical characteristics of these tumors render them sensitive to detection by DWI. Due to their high grade and often high degree of necrosis, they may not exhibit enhancement on conventional imaging sequences that currently are the standard imaging method for detection of drop metastasis. Medulloblastoma, a PNET, is the second most common neoplasm of the CNS in children and has pathologic features that make it optimal for

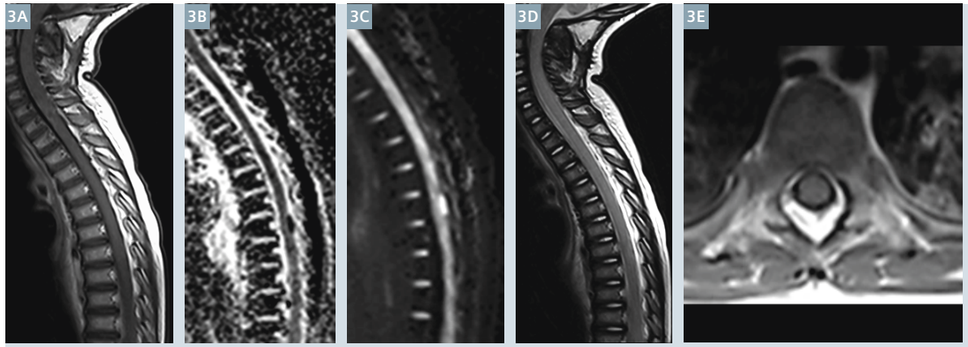

3 2-year-old girl* with ataxia and vomiting found to have a large posterior fossa tumor that restricted diffusion and demonstrated minimal enhancement, consistent with an atypical rhabdoid teratoid tumor (ATRT). Initial MRI scan of the spine: Sagittal T1 post-contrast **(3A)**, ADC map **(3B)**, isotropic DWI **(3C)**, sagital T2 **(3D)**, and axial T1 post-contrast image at the level of interest **(3E)** demonstrate the lack of any abnormal signal or enhancement **(3A, D, E)** at the location of the nodular diffusion abnormality at the dorsal aspect of the thoracic cord **(3B, C)**.

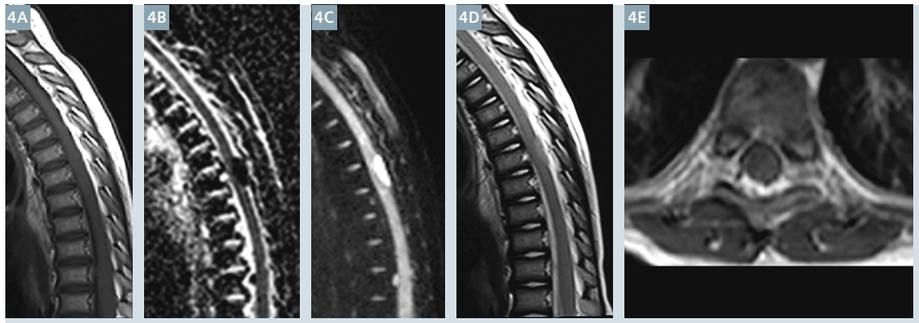

4 Follow up scan two months later. Sagittal T1 post-contrast **(4A)**, ADC map **(4B)**, isotropic DWI **(4C)**, sagittal T2 **(4D)**, and axial T1 post-contrast image at the level of interest **(4E)** demonstrate interval increase in the size of the previously visualized nodular diffusion abnormality, now also seen on the T2 image as well. Another nodular diffusion abnormality along the ventral aspect of the lower thoracic cord is now clearly visible. Note the continued lack of conspicuity on the T1 post-contrast images **(4A, E)**.

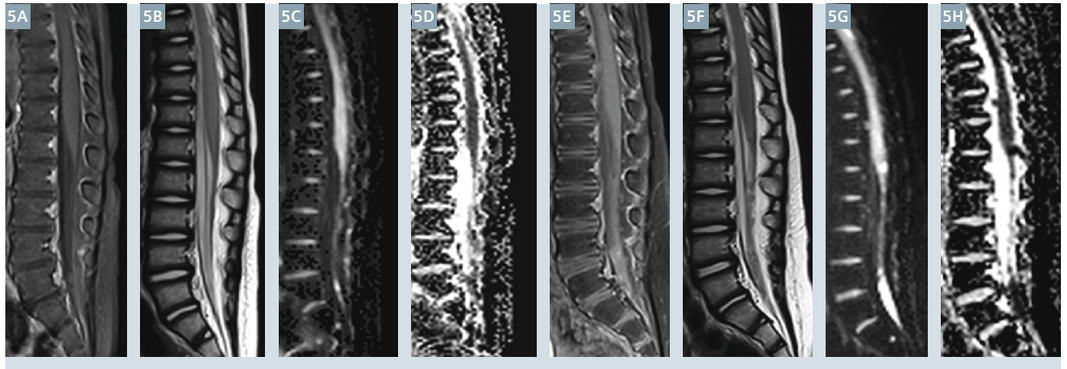

5 Images of the thoracolumbar spine from initial scan **(5A–D)** and follow-up scan two months later **(5E–H)**. Initially negative T1 post-contrast **(5A)** and T2 image **(5B)** with possible tiny, nodular diffusion abnormality along the distal cauda equina on isotropic DWI **(5C)** and ADC map **(5D)**. Follow-up T1 post-contrast image demonstrates enhancement within the distal thecal sac **(5E)**; T2 image demonstrates nodularity along the cauda equina and within the distal thecal sac **(5F)**; isotropic DWI **(5G)** and ADC map **(5H)** demonstrate nodular and clumpy areas of restricted diffusion consistent with drop metastases.

evaluation with DWI. Other CNS tumors that can restrict diffusion and spread to the spine include other PNETs such as atypical teratoid rhabdoid tumor (ATRT), as well as ependymoma, glioblastoma multiforme, germinoma, and choroid plexus carcinoma.

ii. Primary cord tumor

Just as in the brain, DWI is helpful in narrowing the differential diagnosis of primary spinal tumors (Fig. 6). Diffusion tensor imaging (DTI) can be used to visualize ordered white matter tracts of the spinal cord in an effort to further characterize a mass. It is helpful to determine whether the lesion displaces the tracts or infiltrates between them. Identification of white matter tracts can ultimately assist in surgical planning as well [12].

iii. Epidermoid

Restricted diffusion within a solitary intradural cyst is essentially pathognomonic for an epidermoid cyst (Fig. 7). The restricted diffusion within these cysts is related to their squamous epithelial contents. Epidermoids are often congenital and can be related to tethered cords, a common indication for spine MRI in children. Arachnoid cysts and epidermoid cysts can be easily differentiated with DWI [13].

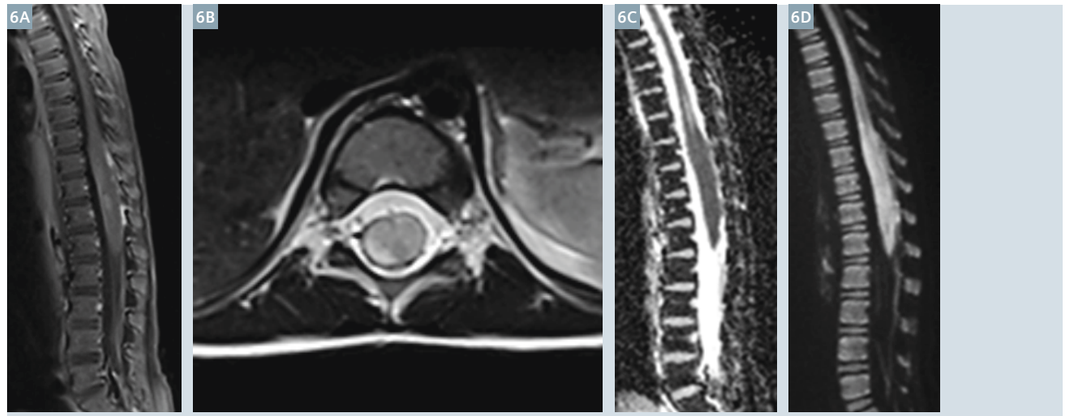

6 2-year-old boy* with limping and back pain. Sagittal T1 post-contrast **(6A)** and axial T2 images **(6B)** demonstrate an intramedullary mass involving the conus medullaris. There is mild enhancement of the lesion, and the mass is iso- to hyperintense on T2. ADC map **(6C)** reveals isointensity of the mass with the normal cord, corresponding to an iso- to hyperintense appearance on the isotropic DWI image **(6D)**. This excludes a densely cellular lesion such as PNET, and is consistent with a lower grade lesion such as a diffuse leptomeningeal neuroepithelial tumor (DLNT) as in this case.

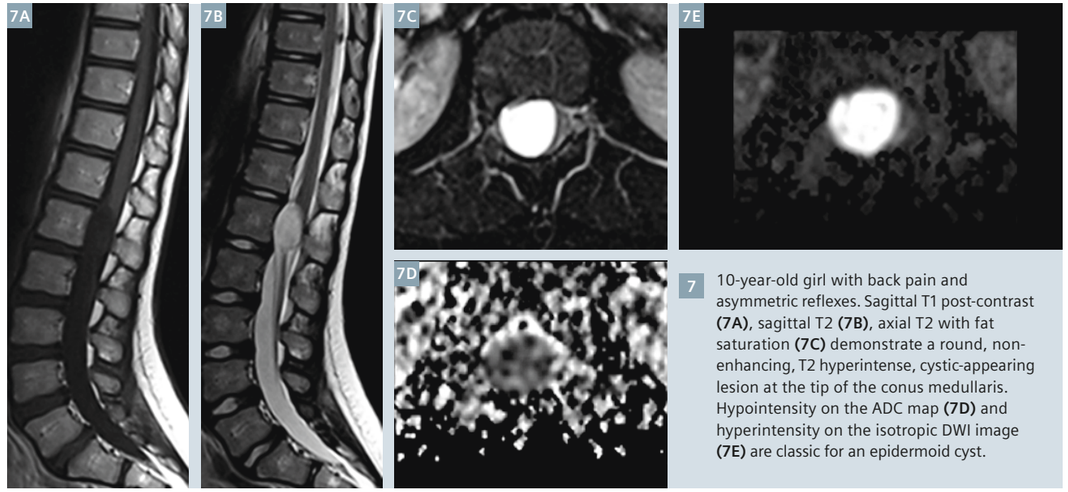

7 10-year-old girl with back pain and asymmetric reflexes. Sagittal T1 post-contrast **(7A)**, sagittal T2 **(7B)**, axial T2 with fat saturation **(7C)** demonstrate a round, non-enhancing, T2 hyperintense, cystic-appearing lesion at the tip of the conus medullaris. Hypointensity on the ADC map **(7D)** and hyperintensity on the isotropic DWI image **(7E)** are classic for an epidermoid cyst.

b. Extradural

i. Vertebral/paravertebral/ metastatic tumors

As previously discussed, spine DWI is particularly well-suited to pediatric oncologic imaging due to the high frequency of densely cellular tumors that occur in children. These tumors can be found both intra- and extradurally within the spine. Pediatric extradural tumors that lend themselves to DWI detection include neuroblastoma, leukemia, lymphoma, rhabdomyosarcoma, and Ewing sarcoma (Fig. 8). The unifying pathologic feature of these tumors is that they are comprised of small, round, blue cells. In the case of primary vertebral Ewing sarcoma, DWI not only assists with tumor detection but also in differentiation from other vertebral lesions that can have a similar appearance on conventional imaging sequences such as eosinophilic granuloma and chordoma (Fig. 9).

Diffusion-weighted imaging can also be a useful tool for distinguishing acute benign osteoporotic from malignant vertebral compression fractures. Increased water motion is typically present in post-traumatic benign compression fractures resulting in low or iso-intense signal on DWI and high ADC values on ADC maps [14]. In contrast, pathologic compression fractures related to densely cellular tumors such as lymphoma have restricted diffusion with hyperintensity on DWI and hypointensity on ADC maps [15] (Fig. 10).

2. Infarction

DWI is a powerful tool in the identification of spinal cord infarction, sometimes revealing restricted diffusion in the cord even before changes on the T1 or T2-weighted images develop [16]. Spinal cord infarctions in children are rare, but can occur in such settings as spinal arteriovenous malformations (AVMs) and fibrocartilaginous emboli. The latter are caused by retrograde migration of nucleus pulposis from the intervertebral disk into the spinal microcirculation [17]. This is usually caused by a minor physical trauma or a physical effort in conjunction with Valsalva [16]. Acute spinal cord infarcts present with severe pain followed by a rapidly progressive paraplegia/tetraplegia and loss of reflexes. MR images reveal cord swelling, increased T2 signal, and

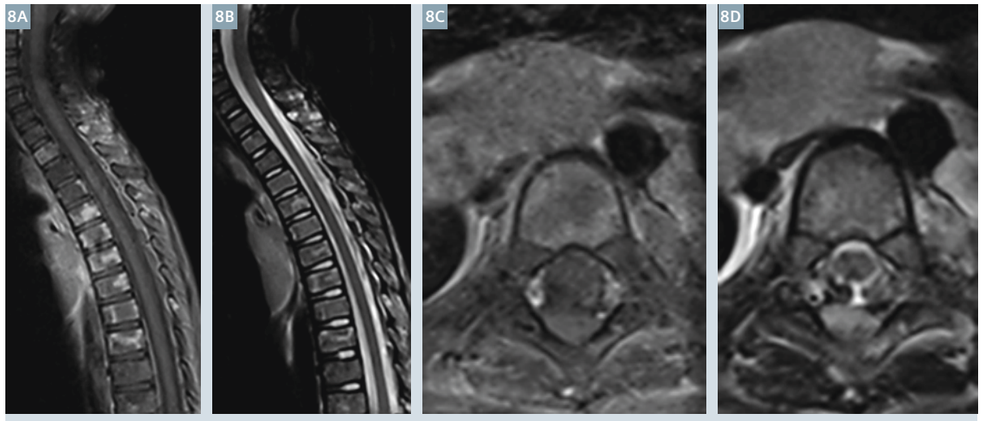

8 6-year-old boy with intermittent fevers, bilateral leg pain, and abdominal mass. Sagittal T1 post-contrast with fat saturation **(8A)**, sagittal T2 **(8B)**, axial T1 post-contrast with fat-saturation **(8C)**, axial T2 with fat-saturation **(8D)**, sagittal ADC map **(8E)** and isotropic DWI **(8F)** images demonstrate a large paraspinal mass invading the central spinal canal. Restricted diffusion within the mass is consistent with neuroblastoma. Note the epidural involvement at the dorsal aspect of T5, well delineated on the isotropic DWI sequence. Extensive metastatic disease involving the vertebral bodies is also apparent.

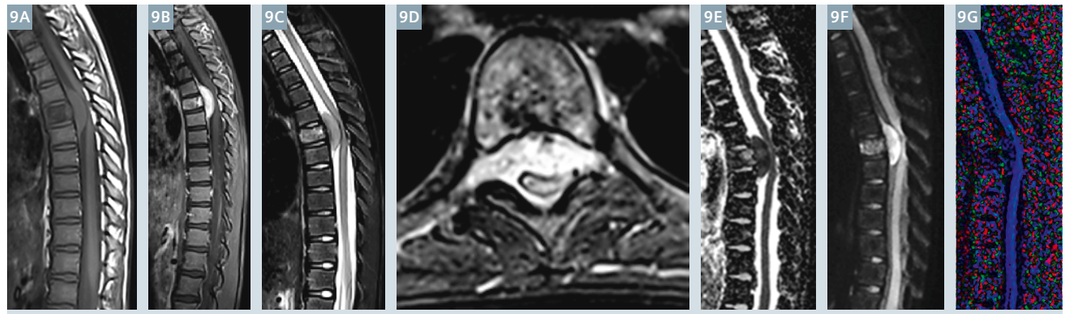

9 8-year-old boy with ataxia. Sagittal pre-contrast T1 **(9A)** and post-contrast T1 with fat saturation **(9B)**, sagittal and axial T2 with fat saturation **(9C, D)**, sagittal ADC **(9E)**, isotropic DWI **(9F)**, and color FA (fractional anisotropy) map **(9G)** reveal a large, enhancing epidural mass involving the T6 vertebral body producing cord compression. Restricted diffusion in the mass **(9E, F)** is typical for Ewing sarcoma.

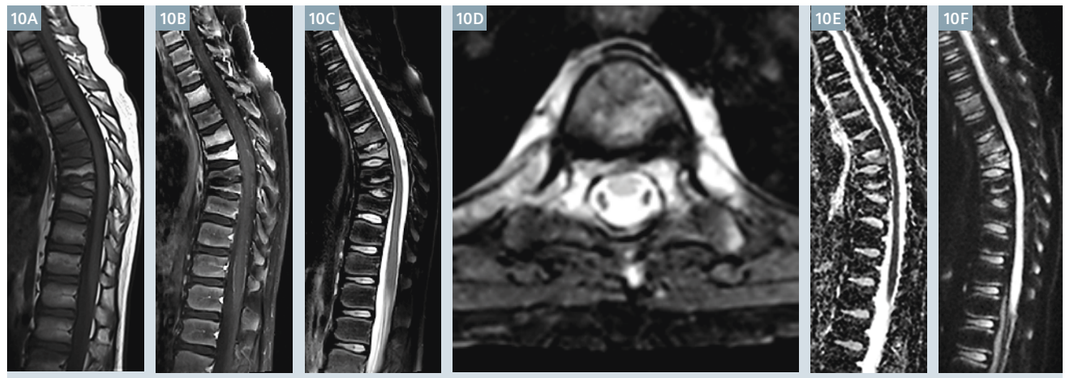

10 10-year-old boy with back pain. Sagittal pre-contrast T1 **(10A)**, post-contrast T1 with fat saturation **(10B)**, sagittal and axial T2 with fat saturation **(10C, D)**, ADC map **(10E)** and isotropic DWI **(10F)** images demonstrate multilevel compression fractures with enhancement of the involved vertebral bodies, low signal on ADC maps, and marked hyperintensity on DWI. Findings are consistent with leukemia/lymphoma. Chronic relapsing multifocal osteomyelitis is one differential consideration.

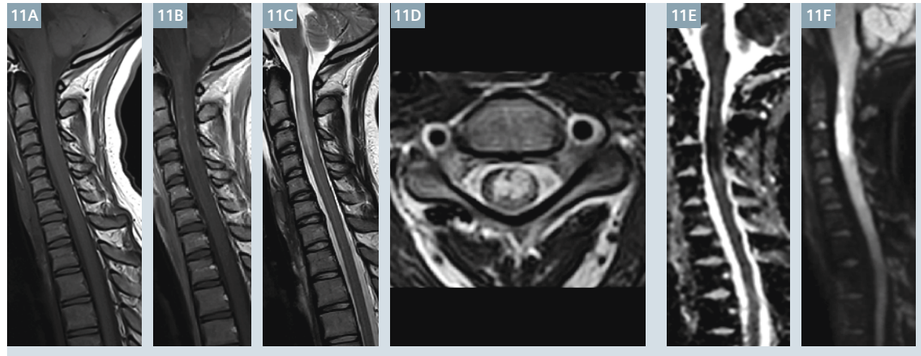

11 17-year-old girl with acute onset of neck pain followed by flaccid tetraparesis. Sagittal pre- and post-contrast T1 **(11A, B)** and sagittal and axial T2 **(11C, D)** images demonstrate intrinsic T2 hyperintensity within the cord from the level of the cervicomedullary junction to the level of C4. There is corresponding hypointensity with minimal enhancement on T1. Sagittal ADC map **(11E)** demonstrates marked hypointensity within the cord at these levels, and isotropic DWI image **(11F)** demonstrates hyperintensity consistent with acute cord infarction.

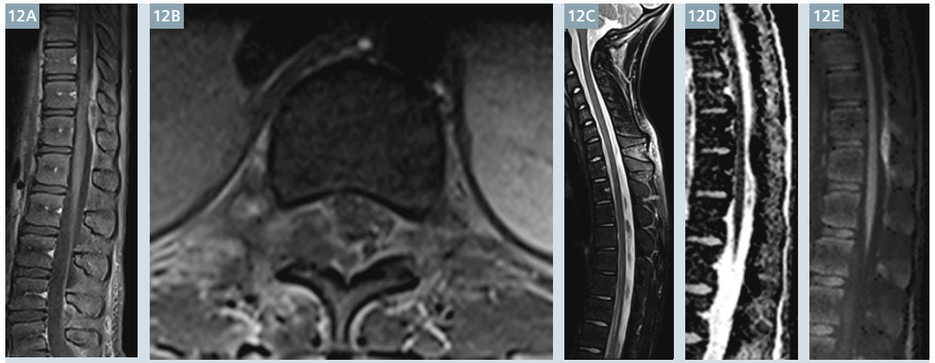

12 12-year-old girl with back pain, fever, and CSF pleocytosis. Sagittal and axial T1 post-contrast with fat saturation **(12A, B)**, sagittal T2 with fat saturation **(12C)**, sagittal ADC map **(12D)**, and isotropic DWI **(12E)** images reveal an epidural collection with irregular enhancement with associated paraspinal soft tissue edema. There is corresponding hypointensity on the ADC map with well-defined hyperintensity on isotropic DWI in keeping with restricted diffusion in an abscess.

markedly restricted diffusion [18] (Fig. 11). Spinal cord infarcts secondary to fibrocartilaginous emboli can demonstrate loss of expected T2-hyperintensity in the disk and loss of disk height.

DWI can aid in the differentiation of acute infarction from inflammatory conditions such as transverse myelitis, a condition not uncommon in children. While restricted diffusion can be seen with transverse myelitis once vasogenic edema becomes cytotoxic, the ADC values are typically not as low as those seen with acute infarction. Further studies are needed to evaluate these differences.

3. Infection

Infection involving the spine is frequently encountered in children. Osteomyelitis, diskitis, and epidural abscesses are common ailments, caused by hematological seeding of bacteria and often manifested with fever, pain, and/or limp. Abscesses can be surgical emergencies due to their potential for cord compression that requires emergent surgical intervention before permanent cord damage ensues. Prompt and accurate imaging detection is critical, and can be assisted by the use of spine DWI. Both osseous and epidural/intradural abscesses restrict diffusion, appearing markedly hyperintense on isotropic trace images and dark on ADC maps [19]. Polymorphonuclear leukocytes and necrotic debris in abscesses restricts water motion, a characteristic that can help differentiate abscesses from simple or mildly proteinaceous fluid collections. Abscess formation is often more conspicuous on DWI than on conventional images. DWI can also identify the extent of the abscess and assist in identifying multifocal disease that may not otherwise be apparent (Fig. 12).

Future directions

DWI shows promise in the evaluation of numerous pathological states of the pediatric spine. More research is needed in regards to demyelinating disease such as multiple sclerosis and spinal cord trauma such as SCIWORA (Spinal Cord Injury Without Radiographic Abnormality) in an effort to improve lesion detection and contribute to a prompt and accurate prognosis.

Several technical developments could further improve the quality of spine DWI images, specifically the use of coils with larger numbers of elements (which has improved diffusion imaging of the brain in recent years) and the use of multi-band to improve the efficiency of the image acquisition [20, 21]. Work also needs to be done to determine the optimum b-values for spine imaging as a range of values has been used in the literature.

As RESOLVE becomes more readily available in the community, it should serve to revolutionize spine imaging just as DWI did when it was introduced into routine MR imaging of the brain. DWI of the brain is currently standard-of-care in MR imaging, and we expect that DWI of the spine will become part of the standard of care for spine imaging in the near future.

Conclusions

RESOLVE DWI is a powerful imaging tool for evaluation of spinal pathology. Images presented in this article demonstrate that this technique is exquisitely helpful in the work-up of numerous pathological conditions of the spine affecting children, including tumor, infarction, and infection.

*Siemens Disclaimer: MR scanning has not been established as safe for imaging fetuses and infants less than two years of age. The responsible physician must evaluate the benefits of the MR examination compared to those of other imaging procedures.

References

1 Porter DA, Heidemann RM. High resolution diffusion weighted imaging using readout segmented echo planar imaging, parallel imaging and a two dimensional navigator based reacquisition. Magn Reson Med 2009;62:468-475.

2 Porter DA, Mueller E. Multi-shot diffusion-weighted EPI with readout mosaic segmentation and 2D navigator correction. In: Proceedings of the 12th Annual Meeting of ISMRM, Kyoto, Japan, 2004. p442.

3 Robson MD, Anderson AW, Gore JC. Diffusion-weighted multiple-shot echo planar imaging of humans without navigation. Magn Reson Med 1997; 38:82-88.

4 Miller KL, Pauly JP. Nonlinear phase correction for navigated diffusion imaging. Magn Reson Med 2003;50:343–353.

5 Griswold MA, Jakob PM, Heidemann RM, Nittka M, Jellus V, Wang J, Kiefer B, Haase A. GeneRalized Autocalibrating Partially Parallel Acquisitions (GRAPPA). Magn Reson Med 2002;47:1202-1210.

6 Ordidge RJ, Helpern JA, Qing ZX, Knight RA, Nagesh V. Correction of motional artefacts in diffusion-weighted MR images using navigator echoes. Magn Reson Imag 1994; 12:455-460.

7 Anderson AW, Gore JC. Analysis and correction of motion artifacts in diffusion weighted imaging. Magn Reson Med 1994;32:379-387.

8 Nguyen Q, Clemence M, Thornton J, Ordidge RJ, Isotropic diffusion-weighted multishot imaging using automatic reacquisition. In: Proceedings of the 7th Annual Meeting of ISMRM, Philadelphia, USA, 1999. p 559.

9 Porter DA. 2D-navigator-based re-acquisition for motion artefact suppression in multi-Shot, diffusion-weighted Imaging. In: Proceedings of the 14th Annual Meeting of ISMRM, Seattle, USA, 2006. p1047.

10 Moffat BA, Chenevert TL, Lawrence TS et al. Functional diffusion map: a noninvasive MRI biomarker for early stratification of clinical brain tumor response. PNAS 2005; 102(15): 5524-5529.

11 Hayes LL, Jones RA, Palasis S, Aguilera D, Porter DA. Drop metastases to the pediatric spine revealed with diffusion-weighted MR imaging. Pediatr Radiol 2012;42(8): 1009-13.

12 Tanenbaum LN. Clinical applications of diffusion imaging in the spine. Magn Reson Imaging Clin N Am 2013;21(2): 229-320.

13 Kukreja K, Manzano G, Ragheb J, Medina LS. Differentiation between pediatric spinal arachnoid cyst and epidermoid-dermoid cysts: is diffusion-weighted MRI useful? Pediatr Radiol 2007;37(6):556-60

14 Rumpel H, Chong Y, Porter DA, Chan LL. Benign versus metastatic vertebral compression fractures: combined diffusion-weighted MRI and MR spectroscopy aids differentiation. Eur Radiol 2013;23(2):541-50.

15 Baur A, Stäbler A, Brüning R, Bartl R, Krödel A, Reiser M, Deimling M. Diffusion-weighted MR imaging of bone marrow: differentiation of benign versus pathologic compression fractures. Radiology 1998;207(2):349-56.

16 Manara R, Calderone M, Severino MS, Citton V, Toldo I, Laverda AM, Sartori S. Spinal cord infarction due to fibrocartilaginous embolism: the role of diffusion weighted imaging and short-tau inversion recovery sequences. J Child Neurol 2010;25(8):1024-8.

17 Reisner A, Gary MF, Chern JJ, Grattan-Smith JD. Spinal cord infarction following minor trauma in children: fibrocartilaginous embolism as a putative cause. J Neurosurg Pediatr 2013;11(4):445-50.

18 Tsang BK, Foster E, Kam A, Storey E. Diffusion weighted imaging with trace diffusion weighted imaging, the apparent diffusion coefficient and exponential images in the diagnosis of spinal cord infarction. J Clin Neurosci 2013;20(11): 1630-2.

19 Eastwood JD, Vollmer RT, Provenzale JM. Diffusion-weighted imaging in a patient with vertebral and epidural abscesses. AJNR 2002;(23): 496-498.

20 Setsompop K, Gagoski BA, Polimeni JR, Witzel T, Wedeen VJ, Wald LL. Blipped-controlled aliasing in parallel imaging for simultaneous multislice echo planar imaging with reduced g-factor penalty. Magn Reson Med 2012;67:1210–1224.

21 Frost R, Porter DA, Douaud G, Jezzard P, Miller KL. Reduction of diffusion-weighted readout-segmented EPI scan time using a blipped-CAIPI modification. In: Proceedings of the 20th Annual Meeting of ISMRM, 2012 (abstract 116).

Contact

Laura L. Hayes, M.D.
Children's Healthcare of Atlanta at Scottish Rite
1001 Johnson Ferry Road NE
Atlanta, GA 30342
USA
laura.hayes@choa.org

Magnetic Resonance Neurography Evaluation in Children

Avneesh Chhabra, M.D.[1, 2]; Vibhor Wadhwa, MBBS[2]; Sahar J. Farahani, M.D., MPH[2]; Gaurav K. Thawait, M.D.[2]; John A. Carrino, M.D., MPH[2]

[1] University of Texas Southwestern Medical Center, Dallas, TX, USA
[2] The Russel H. Morgan Department of Radiology and Radiological Science, Johns Hopkins University School of Medicine, Baltimore, MD, USA

Abstract

Magnetic Resonance Neurography has proven to be an excellent technique for the evaluation of peripheral neuropathies. However, its use in pediatric age group has been less well described. In this article, the authors discuss the technical considerations, various common causes of peripheral neuropathies in children* and the role of magnetic resonance neurography in their diagnosis and management.

Introduction

A wide spectrum of peripheral nerve pathologies are encountered in children, including hereditary neuropathy, traumatic birth injury and motor vehicle accident, neoplasm, infection and inflammation. Clinical features in these cases are often nonspecific and invasive electrodiagnostic tests, such as nerve conduction studies are usually uncomfortable and not feasible in the pediatric age group. Peripheral nerve imaging can therefore, be very useful in small children with strong clinical suspicion in whom the diagnosis cannot be firmly established. However, small size of the nerves and the relative lack of specific clinical features makes imaging of the nerves challenging and requires high technical skill for performance and interpretation. There is a paucity of literature describing the diagnostic role of peripheral nerve imaging in children [1-3]. Magnetic Resonance Neurography (MRN) is a non-invasive imaging technique, which enables direct visualization of the anatomy and pathology of the peripheral nerves and regional muscles, thereby aids in localizing the site of injury or tumor. It can not only help in confirming and localizing the neuropathy, but also in ruling out neuropathy by showing normal appearing nerves and regional muscles. The authors describe the MRN technique used in pediatric age group and discuss a spectrum of peripheral nerve pathologies that can be observed in children using relevant case examples.

MR Neurography technique

The currently available 3 Tesla scanners (MAGNETOM Skyra, Verio and Trio, Siemens Healthcare, Erlangen, Germany) are preferred over 1.5T systems (MAGNETOM Aera and Avanto) due to higher signal-to-noise ratio (SNR) and short imaging times on the higher field scanners. Additionally 3D imaging with fat suppression is better obtained on 3T scanners. 2D imaging can be obtained similarly on both types of scanners, although it takes a little longer on 1.5T scanners, especially when one tries to attain similar image quality on thin section (2–3 mm) scans. High resolution imaging with combined 2D and 3D isotropic spin echo type imaging is essential for optimal assessment of small peripheral nerves. The inability to stay still for infants and small children makes imaging more challenging, frequently requiring sedation or general anesthesia for adequate results and to avoid repeat acquisition [1].

1 Normal LS plexus and sciatics in a young girl. MIP image from coronal 3D STIR SPACE sequence shows normal symmetrical appearance of the LS plexus nerve roots (short arrows) and bilateral sciatic nerves (long arrows).

One should use dedicated coils as far as possible. For MRN imaging around the joints, use joint specific coils, such as wrist, elbow, ankle etc. If a joint specific coil is not available, use the smallest possible flex coil to cover the expected anatomy. For contiguous imaging of the joint and extremity, e.g. wrist and forearm, use wrist coil and flex coil separately in the adolescent child to avoid excess blank (air) space around the extremity. In a child or infant, a single flex coil can suffice for such imaging due to the relatively small size of the extremity. During plexus imaging, use a combination of body array on the front and spine elements on the back to attain uniformity of magnetic signal in the field-of-view.

High resolution 2D (dimensional) axial T1-weighted (T1w) and T2 SPAIR (Spectral Adiabatic Inversion Recovery) sequences are useful for demonstrating regional anatomy of the nerve fascicles. Fascicular architecture of nerves is consistently seen with T2 SPAIR images in larger branches, such as femoral nerves and sciatic nerves, as well as in smaller nerves that are affected and enlarged due to neuropathy, such as lateral femoral cutaneous and genitofemoral nerves [4, 5]. Fluid sensitive sequences such as STIR (short tau inversion recovery) images have more uniform fat suppression and higher T2 contrast, especially in the presence of metal or in off-center areas [6], however STIR imaging is often marred by low SNR, pulsation artifacts and increased baseline nerve signal intensity. SPAIR produces higher SNR images and are less prone to blood flow artifacts than STIR imaging, which could be disadvantageous as peripheral nerves travel in neurovascular bundles. Use a TR/TE/TF of ~ 3800–4000/60–65/15–25 for T2 SPAIR imaging. Sagittal STIR imaging is particularly useful in brachial plexus imaging to obtain uniform fat suppression in a difficult neck area and to tease out asymmetrical or individual nerve signal intensity and caliber alterations. Dixon type fat suppression is also useful in generating uniform fat suppression.

3D images complement information generated from 2D imaging by showing nerves in longitudinal planes. The imaging can be obtained using isotropic 3D SPACE (Sampling Perfection with Application optimized Contrasts using variable flip angle Evolutions) technique. A variety of contrasts are available on SPACE sequence, including T1, T2, PD, STIR and SPAIR. Non-fat suppressed T2 SPACE (TR/TE/TF ~ 1500–1700/110–120/42–50) is used for spine imaging, which is necessary in plexus evaluation. One can routinely obtain 0.8–0.9 mm isotropic images through the cervical or lumbar spine. In cases of suspected nerve root avulsions, one should also obtain 3D CISS imaging focused at spine for high resolution (0.6–0.65 mm isotropic) evaluation of preganglionic nerve rootlets. For post ganglionic nerve assessment in plexuses, fat suppressed 3D imaging using STIR SPACE (TR/TE/TF/SL ~ 2000–2200/70–80/50–60/1.3–1.5 mm isotropic) is most useful. There is virtually no pulsation artifact on the 3D imaging and once thick slab (8–15 mm) maximum intensity projections (MIPs) are created, the image looks smoothened and shows the high intensity nerves along their long axis or in any desired arbitrary plane, e.g. oblique sagittal planes are useful to depict femoral and sciatic nerves along their long axes (Fig. 1). SPAIR SPACE (0.9–1.0 mm isotropic) is very useful in extremity imaging due to higher SNR and similar uniform fat suppression. The nerve perpendicular plane shows cross-sectional appearance of the fascicular anatomy of the nerve. The longitudinal plane along the long axis of the nerve shows focal or diffuse nerve enlargement and mass effect of regional perineural lesions [1]. 3D imaging is helpful in localizing the lesions along the axis of the nerve, course deviations, focal neuroma, neurotmesis, etc. and for better preoperative planning. In extremities, another 3D imaging, i.e. 3D DW PSIF (diffusion-weighted reversed steady state in free precession) is extremely useful to create nerve specific isotropic images due to effective fat and vascular suppression (TR/TE/SL ~ 12/3/0.9, b-value for diffusion~60–80 ms and water selective fat suppression). Additional coronal T1w, STIR/PD SPAIR images aid in detection of lesions along the long axis of the nerves as well as allow assessment of regional joints and musculotendinous structures. These also serve as fall back sequences, in case the subject moves during the scan or if there is failure of 3D imaging for any reason. IV gadolinium contrast is not routinely used in injury cases, however is useful for differentiating types of neural hypertrophy such as suspected neoplasm, infection, inflammation, diffuse polyneuropathy, neurocutaneous syndromes, or post-operative complication [7, 8].

Normal and abnormal peripheral nerves

Normal peripheral nerves show isointense signal on T1w and T2w images. On T2 SPAIR images, minimal hyperintensity is normal, especially where the nerves curve around the joints. On 3D STIR SPACE images, the nerves appear uniformly hyperintense in the plexuses due to increased sensitivity to the endoneurial fluid. Most hyperintensity is seen at the dorsal nerve root ganglion level and the signal fades distally along the course of the nerves. Pathological nerves show one or a combination of findings, such as increasing hyperintensity approaching the signal of the regional vessels and encompassing a long segment of the nerve; focal or diffuse caliber enlargement (more than adjacent regional nerves, contralateral counterpart nerve or artery in the neurovascular bundle); internal fascicular

*MR scanning has not been established as safe for imaging fetuses and infants less than two years of age. The responsible physician must evaluate the benefits of the MR examination compared to those of other imaging procedures.

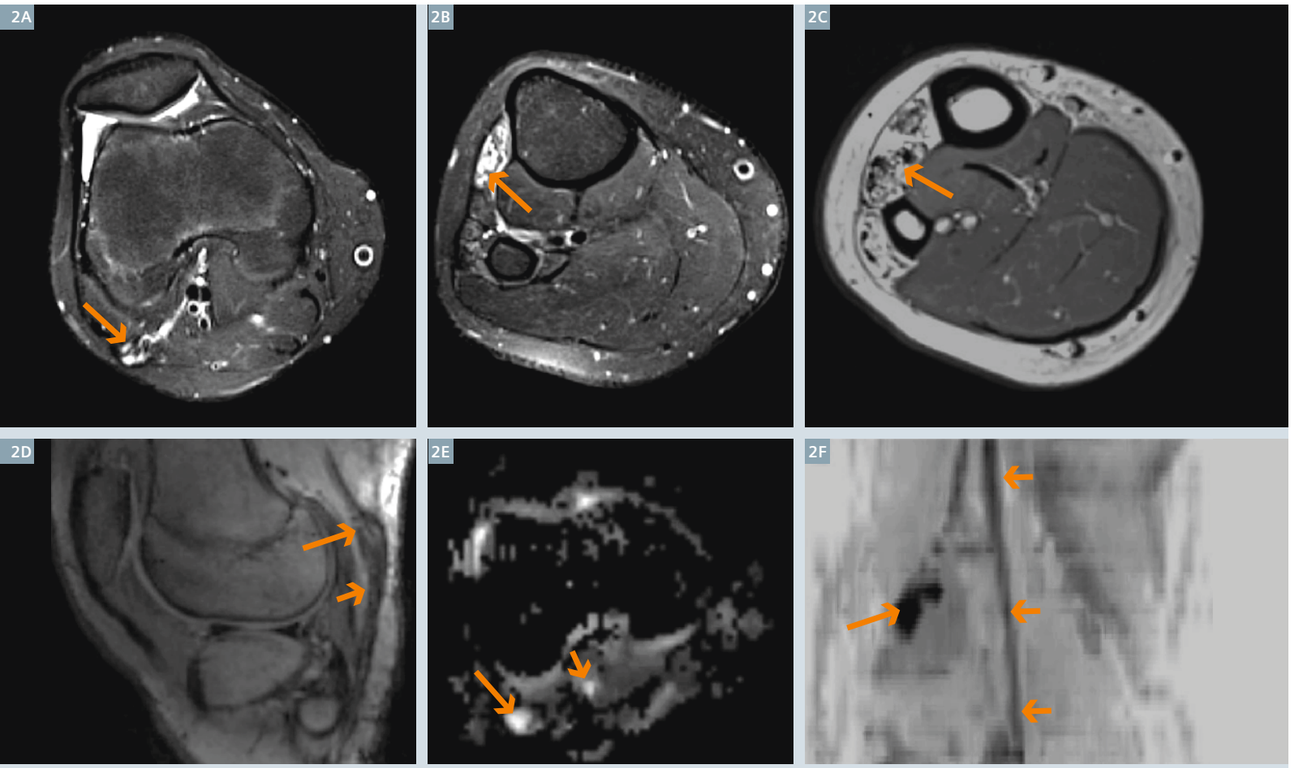

2 Surgical failure. Axial T2 SPAIR **(2A)** image shows enlarged neuromatous common peroneal nerve (CPN) (arrow) following placement of nerve tube to bridge the resected mass of the CPN. Axial T2 SPAIR image and T1w images **(2B, C)** distally show edema like signal and fatty replacement of the muscles (arrows). Oblique sagittal 3D DW PSIF reconstructed image **(2D)** shows the findings in the long axis with neuromatous proximal nerve (long arrow) and empty nerve tube (short arrow). DTI tensor image **(2E)** and corresponding inverted scale MIP image **(2F)** show the normal continuous normal tibial nerve (small arrows) and discontinuous CPN with end bulb neuromas (long arrows).

enlargement, effacement or atrophy; intra-epineural fat deposition; epineurial or perineurial thickening; perineural fibrosis with or without nerve entanglement; nerve displacement due to mass lesion; heterogeneous nerve thickening suggesting a neuroma in continuity or end bulb neuroma from complete rupture or failure of nerve regeneration (Fig. 2); and finally, regional muscle denervation changes, which by definition are distal to the site of the entrapment [2, 4-6].

Indications

Hereditary neuropathy is the most common etiology in children. Acquired cases can be seen due to infection, inflammation, neoplastic and trauma causes. On the other hand, adults usually suffer from neuropathies secondary to entrapment, toxic insult or systemic disease, such as diabetes. It is thus important to understand the differing etiology in adults and children in order to make a proper diagnostic plan for evaluation of peripheral neuropathies in pediatric age group. MR Neurography is indicated in children with suspected but unclear underlying hereditary or acquired pathology that may cause neuropathy, known neuropathy without any identifiable underlying cause, and to characterize neuropathy in cases of infection, inflammation or trauma.

Advantages of MRN

MRN is particularly useful in children due to frequent inability of electrodiagnostic studies (EDS) to yield diagnostic information. Moreover, MRN is not operator dependent and can localize the exact site of nerve pathology. It provides useful data for preoperative planning and postoperative response to surgical treatment even before clinical and functional improvement is noticeable [1]. The EDS give vital physiologic information about the nerve pathology by evaluating nerve conduction velocity or muscle action potentials using electromyography [9]. On the other hand, imaging studies primarily evaluate the anatomy and results of nerve pathology. Both these modalities are used to complement information gained from one another to reach a correct diagnosis. Although ED tests are good for systemic conditions causing peripheral neuropathies, they are highly dependent on clinical and technical expertise of the examiner and are not practical in infants or small children, since patient cooperation is imperative to their success [10]. Imaging of the nerves as such is of vital importance in children for evaluation of neuropathies.

Non-invasive imaging of nerves can be done using ultrasonography (US) or MRN. US is cost effective, portable and allows dynamic assessment of the extremity nerves. Large segments of the nerves can be seen along their entire course in the extremities. It does require considerable technical skill and cannot depict subtle changes in signal intensity as with MRN in cases with mild neuropathy without fascicular enlargement. Deep nerves are difficult to interrogate using US and muscle denervation changes are not apparent till late stage. MRN can evaluate the nerves, their innervated muscles and regional soft tissue structures. With its combined 2D and 3D imaging capabilities, it can illustrate neuromuscular anatomy and pathology in multiple planes for better interpretation by the radiologist and localize the pathology for preoperative planning for the referring physician.

Spectrum of peripheral neuropathies in children

The causes of neuropathies differ between adults and children. More than 70% of neuropathies in children are related to inherited causes, while most cases of neuropathy in adults are acquired (60%). Adults with acquired neuropathy are mostly related to trauma, entrapment or chronic injury from sports or occupation. In children, acquired neuropathies are more likely secondary to infection and inflammation [11]. Clinically, neuropathy results in numbness, pain, paresthesia and weakness of the innervated muscles. In small children these symptoms may be less noticeable, and thus reflex testing is of vital importance. Following is a discussion of various common causes of peripheral neuropathies.

Hereditary Neuropathies

Inherited Neuropathies are a heterogeneous group of pathologies in which neuropathy is either the primary presentation of the disease (such as Charcot Marie Tooth disease; CMT) or a part of a more generalized or systemic disorder. The latter group encompasses a large group of rare disorders such as familial amyloid polyneuropathy (FAP), porphyria, ataxia telangiectasia and many other syndromes. The most common of hereditary neuropathies is CMT, which is classified into various types based on pathogenesis – demyelination or axonal degeneration. Clinical features include muscle denervation changes (weakness, atrophy), high plantar arches, impaired sensation and diminished deep tendon reflexes [12, 13]. The most common form of CMT is autosomal dominant demyelinating CMT (CMT type 1A), which is seen in 70% cases. MR imaging is a useful adjunct to clinical and electrodiagnostic suspicion of the neuropathy. One would see diffuse enlargement of bilateral peripheral nerves with abnormally increased signal intensity and/or fascicular prominence in a symmetric fashion. Most enlargement is observed in CMT type 1A. No significant enhancement is seen on post-contrast imaging. Whole-body MR Neurography (WBMRN) is likely to be useful in future to assess the disease burden in these diffuse polyneuropathy cases [14]. Nerve biopsy is the most accurate test to diagnose CMT, however it is rarely necessary these days.

Neoplastic

The most common peripheral nerve sheath tumors (PNSTs) in children are neurofibromas (NF) and schwannomas [15]. These are benign tumors arising from the Schwann cells, with additional non-neoplastic cells including neurons, perineurial cells and endoneurial fibroblasts [16]. NFs may be described as localized, diffuse or plexiform. Most of NFs are of localized variant seen as small (< 5 cm) fusiform masses involving a superficial or major peripheral nerve. Plexiform NF, on the other hand, comprises proliferation of cells in the nerve sheath spreading along the length of the nerve and involving multiple nerve fascicles. They are more commonly associated with neurofibromatosis type 1 (NF-1; 90% cases) than localized variants and have a higher propensity to develop malignant PNSTs later in life. Schwannomas are commonly solitary slow-growing subcutaneous lesions < 5 cm in size. They can occasionally be multiple and associated with several hereditary neurocutaneous syndromes, most well defined of these being neurofibromatosis type 2 (NF-2) and Schwannomatosis [17].

On MR imaging, the lesions appear isointense on T1w images and show homogenous to heterogenous increased signal intensity to muscle on T2w images. PNSTs have classically been described using several imaging signs on MRI. The 'tail sign' describes a tail forming at the superior and/or inferior margin of the nerve lesion. The 'target sign' is central hypointense tissue due to collagenous stroma with peripheral increased signal intensity on T2w images due to more myxomatous tissue. It is observed in NF more commonly than Schwannoma. The 'split fat sign' means prominent fat around the slowly growing lesion. The 'fascicular sign' depicts prominent fascicular neurogenic appearance within the margin of the lesion. The 'bag of worms' sign is seen in superficial plexiform NFs [17, 18]. While NF may show multifascicular involvement of the nerves, schwannoma shows one or two fascicular continuity with the mass lesion. It is difficult to differentiate between benign and malignant PNSTs on conventional MRI. Diffusion tensor imaging showing low minimum apparent diffusion coefficient (ADC) value ($< 1.1 \times 10^{-3}$ mm^2/s) is useful to find most cellular areas that may suggest malignancy and can be directed for biopsy. In underlying neurofibromatosis, there is increased chance of malignancy and it may develop at an earlier age in life as compared to the isolated forms of malignant peripheral nerve sheath tumors. New onset of severe pain, neurologic deficit, rapid increase in size, heterogeneous appearance and low ADC value can

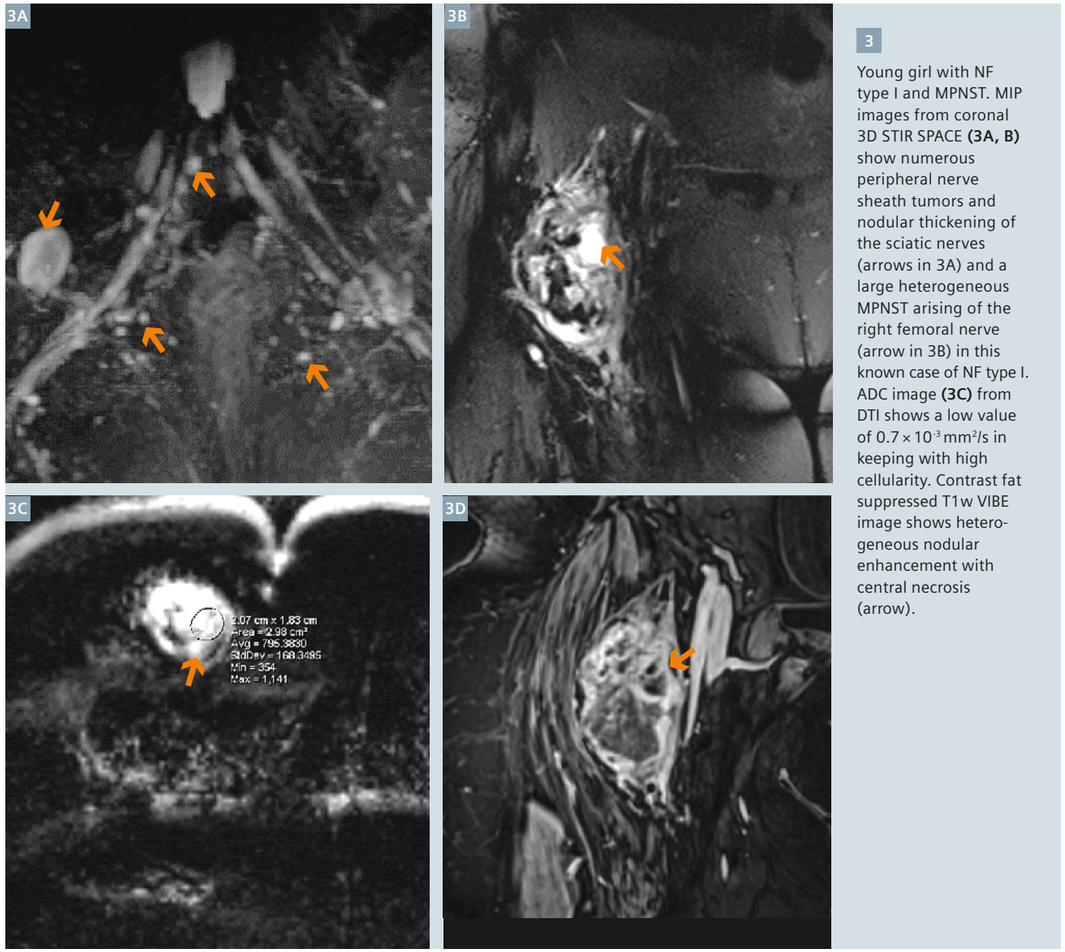

3

Young girl with NF type I and MPNST. MIP images from coronal 3D STIR SPACE **(3A, B)** show numerous peripheral nerve sheath tumors and nodular thickening of the sciatic nerves (arrows in 3A) and a large heterogeneous MPNST arising of the right femoral nerve (arrow in 3B) in this known case of NF type I. ADC image **(3C)** from DTI shows a low value of 0.7×10^{-3} mm²/s in keeping with high cellularity. Contrast fat suppressed T1w VIBE image shows heterogeneous nodular enhancement with central necrosis (arrow).

serve as important signs of incipient malignancy (Fig. 3). Perineurioma is another classic benign tumor, seen in young children in their adolescence showing uniform fascicular thickening and nerve thickening over a long segment, usually in a sciatic distribution. Due to compact fascicular thickening, it may show ADC values in the range of $1.0–1.2 \times 10^{-3}$ mm²/s, however, the clinical symptoms of slow motor loss and MRN imaging appearance are classic findings (Fig. 4).

Trauma

Traumatic peripheral nerve injuries are common in both children and adults, albeit the causes are different. About 80% peripheral nerve injuries in children occur in the upper extremity, and the most common causes include obstetric lesions (46.78 %) (Fig. 5) and iatrogenic (16.95 %), with predominant involvement of the brachial plexus and sciatic nerve [19].

Sunderland classified peripheral nerve injuries into five grades of increasing severity [20].

- Neurapraxia (Sunderland Grade I) is a mild form of neural insult leading to temporary impulse conduction block along the affected nerve segment. It is reversible and muscle denervation changes do not occur.
- Axonotmesis (Sunderland Grade II) is more severe than neuraplaxia involving physical disruption of the axon with preservation of outer covering layers of endoneurium, perineurium and epineurium. Wallerian degeneration follows such an insult, which later results in regeneration of the axon along its original course as the nerve coverings are preserved. Although the duration and severity of symptoms is worse, it usually carries an excellent prognosis similar to neurapraxia.
- Neurotmesis (Sunderland Grade III) refers to complete disruption of the axon and supporting connective tissue structures. There is loss of continuity of the nerve fibers, and the regenerating nerve fibers are no longer confined to the endoneurium. This complicates the regeneration process and may lead to dysfunctional distal end of the nerve.
- Grade IV injury results in neuroma -in-continuity (NIC), which encompasses perineurial disruption and entangled disorganized mass of regenerating nerve fibers.
- Sunderland grade V injury leads to end-bulb neuroma, also called stump neuroma with underlying discontinuity with the nerve (Sunderland Grade V) [17, 21].

On MR imaging, NIC appears as a heterogeneous mass with 'tail sign' which does not show enhancement on contrast administration (differentiating it from neurogenic tumor, which shows enhancement). Stump neuromas are seen as fusiform masses with an irregular outline showing decreased signal intensity on T1w images and increased signal intensity on T2w images [21]. MRN can clearly show abnormal nerve hyperintensity and/or enlargement with otherwise underlying nerve continuity in Grade I-III injuries, which undergo medical management, except that one might release superimposed nerve entrapment. Grade IV and V injuries show a focal neuroma and these can also be distinguished based on the presence of nerve continuity or discontinuity.

Infection / Inflammation

Infectious neuropathy may result from direct nerve involvement or immunologic response of the body towards the infectious agent. The most common and important of these is the Guillain-Barre Syndrome (GBS), also known as acute inflammatory demyelinating polyneuropathy (AIDP). Various microorganisms have been implicated as the trigger for the immune response in GBS (Campylobacter jejuni, Cytomegalovirus and Ebstein Barr virus, etc.). GBS is a clinical diagnosis classically presenting in the child after a recent mild infection with weakness, sensory loss, pain, and hypoflexia in the lower extremities. MR imaging is usually ordered in such cases to confirm the diagnosis and more importantly to rule out other spinal cord or nerve root pathologies that mimic AIDP. MRI findings may be normal in pediatric patients. Hyperintensity and nerve thickening

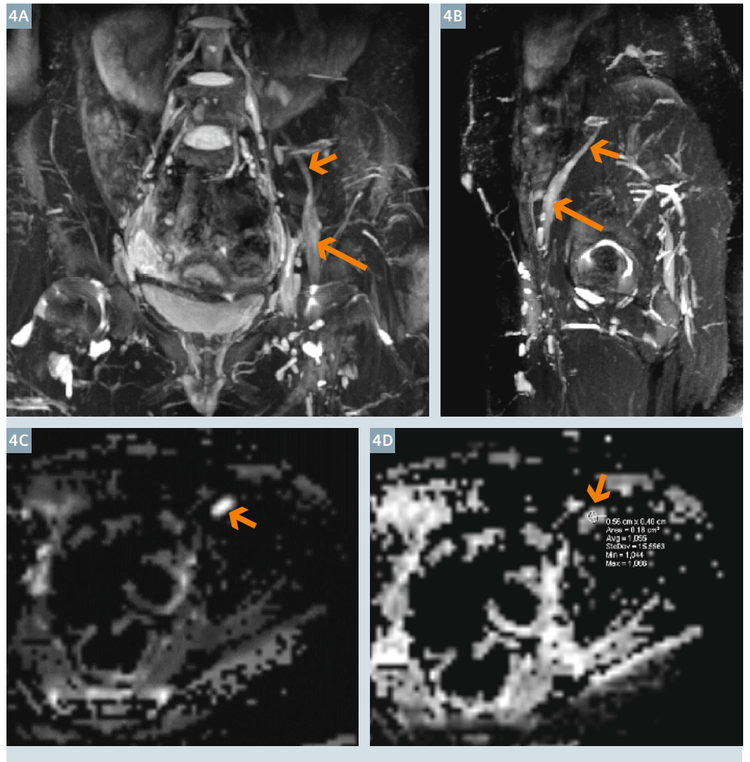

4

Young girl with gradual left leg weakness caused by a Perineurioma. MIP images from coronal and oblique sagittal reconstructed 3D STIR SPACE **(4A, B)** images show left femoral nerve (small arrows) fusiform enlargement by a perineurioma (long arrows). DTI images show ADC value of 1.1×10^{-3} mm²/sec.

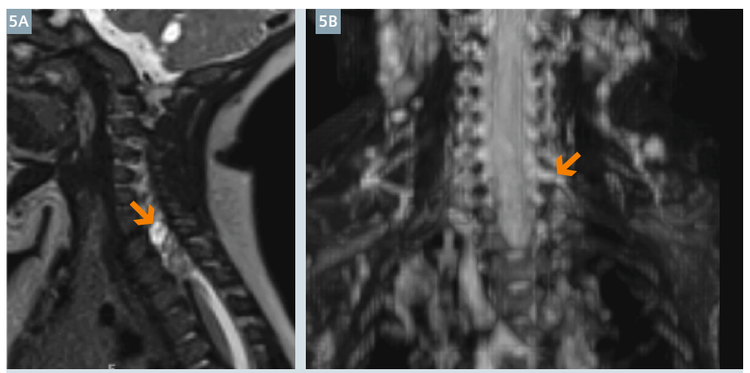

5

Left C7 nerve root avulsion in an infant from birth injury. Sagittal T2w SPACE **(5A)** image and MIP image from coronal 3D STIR SPACE **(5B)** show pseudomeningocele of the left C6-7 neural foramen with left C7 nerve root avulsion (arrows).

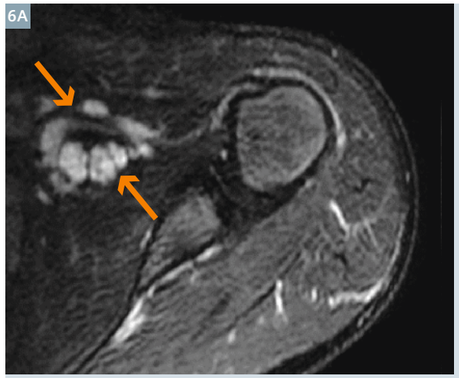

6

CIDP. Young boy with left arm weakness and mild sensory changes. Axial T2w SPAIR **(6A)** and T1w **(6B)** images show multifocal thickening and prominent fascicular appearance of all brachial plexus peripheral branch nerves (arrows). Sagittal fs PDw **(6C)** image shows most thickening of median nerve (long arrow) and less pronounced thickening of the musculocutaneous nerve (small arrow) and axillary nerve (medium arrow).

on MRN images may be seen in spinal nerve roots as a result of the inflammatory process, showing enhancement on contrast imaging. The anterior nerve roots show enhancement more frequently than posterior nerve roots, which is suggestive of GBS [22, 23].

Chronic inflammatory demyelinating polyneuropathy (CIDP) is also an immune mediated condition which presents similar to GBS and is differentiated from GBS on basis of course of the disease (progressive worsening for more than 2 months, while GBS is self-limiting, lower limb involvement > upper limbs and high CSF protein). MR imaging findings in CIDP are nonspecific showing mild to moderate diffuse enlargement with increased cross sectional area of the nerve, as with other hereditary neuropathies such as CMT. However, family history is generally insignificant, the lesions may be asymmetrical or unilateral (Fig. 6) as compared to CMT type IA [4, 24]. Multifocal motor neuropathy is another condition that affects the motor function predominantly and is more common in upper limbs as compared to the lower limbs. Multiple conduction blocks are noted on electrodiagnostic examinations and MRN of the extremity or plexus shows diffuse nerve thickening and/or enlargement, not limited to the entrapment sites. There is generally good response to IVIG treatment or cyclophosphamide therapy.

Conclusion

Imaging of nerves in children is challenging due to their small size and comparative rarity of neuropathies affecting them. MR Neurography is a powerful diagnostic tool even in pediatric population. With proper communication between the referring physician and the radiologist, the diagnostic value of MRN is enhanced leading to early diagnosis and proper patient care.

Acknowledgement

Thanks to Anshita Khanna, University of Toronto for literature search support.

References

1 Cortes C, Ramos Y, Restrepo R, Restrepo JA, Grossman JA, Lee EY. Practical magnetic resonance imaging evaluation of peripheral nerves in children: magnetic resonance neurography. Radiol Clin North Am. 2013;51(4):673-88.
2 Merlini L, Vargas MI, Anooshiravani M, Viallon M, Fluss J, Hanquinet S. Look for the nerves! MR neurography adds essential diagnostic value to routine MRI in pediatric practice: a pictorial overview. J Neuroradiol. 2011;38(3):141-7.
3 Merlini L, Viallon M, De Coulon G, Lobrinus JA, Vargas MI. MRI neurography and diffusion tensor imaging of a sciatic perineuroma in a child. Pediatr Radiol. 2008;38(9):1009-12.
4 Wadhwa V, Thakkar RS, Maragakis N, Hoke A, Sumner CJ, Lloyd TE, et al. Sciatic nerve tumor and tumor-like lesions – uncommon pathologies. Skeletal Radiol. 2012;41(7):763-74.
5 Chhabra A, Faridian-Aragh N. High-resolution 3-T MR neurography of femoral neuropathy. AJR Am J Roentgenol. 2012;198(1):3-10.
6 Chhabra A, Lee PP, Bizzell C, Soldatos T. 3 Tesla MR neurography-technique, interpretation, and pitfalls. Skeletal Radiol. 2011;40(10):1249-60.
7 Thawait SK, Chaudhry V, Thawait GK, Wang KC, Belzberg A, Carrino JA, et al. High-resolution MR neurography of diffuse peripheral nerve lesions. AJNR Am J Neuroradiol. 2011;32(8):1365-72.
8 Chhabra A, Soldatos T, Durand DJ, Carrino JA, McCarthy EF, Belzberg AJ. The role of magnetic resonance imaging in the diagnostic evaluation of malignant peripheral nerve sheath tumors. Indian J Cancer. 2011;48(3):328-34.
9 Dellon AL. Management of peripheral nerve problems in the upper and lower extremity using quantitative sensory testing. Hand Clin. 1999;15(4):697-715.
10 Chemali KR, Tsao B. Electrodiagnostic testing of nerves and muscles: when, why, and how to order. Cleve Clin J Med. 2005;72(1):37-48.
11 Pavone P, Pratico AD, Ruggieri M, Verrotti A, Castellano-Chiodo D, Greco F, et al. Acquired peripheral neuropathy: a report on 20 children. Int J Immunopathol Pharmacol. 2012;25(2):513-7.
12 Skre H. Genetic and clinical aspects of Charcot-Marie-Tooth's disease. Clin Genet. 1974;6(2):98-118.
13 Gaeta M, Mileto A, Mazzeo A, Minutoli F, Di Leo R, Settineri N, et al. MRI findings, patterns of disease distribution, and muscle fat fraction calculation in five patients with Charcot-Marie-Tooth type 2 F disease. Skeletal Radiol. 2012;41(5):515-24.
14 Yamashita T, Kwee TC, Takahara T. Whole-body magnetic resonance neurography. N Engl J Med. 2009;361(5):538-9.
15 Murphey MD, Smith WS, Smith SE, Kransdorf MJ, Temple HT. From the archives of the AFIP. Imaging of musculoskeletal neurogenic tumors: radiologic-pathologic correlation. Radiographics. 1999;19(5):1253-80.
16 Ferner RE, O'Doherty MJ. Neurofibroma and schwannoma. Curr Opin Neurol. 2002;15(6):679-84
17 Wadhwa V, Lee PP, Strome GM, Suh KJ, Carrino JA, Chhabra A. Spectrum of superficial nerve-related tumor and tumor-like lesions: MRI features. Acta Radiol. 2013.
18 Lim R, Jaramillo D, Poussaint TY, Chang Y, Korf B. Superficial neurofibroma: a lesion with unique MRI characteristics in patients with neurofibromatosis type 1. AJR Am J Roentgenol. 2005;184(3):962-8.
19 Uzun N, Tanriverdi T, Savrun FK, Kiziltan ME, Sahin R, Hanimoglu H, et al. Traumatic peripheral nerve injuries: demographic and electrophysiologic findings of 802 patients from a developing country. J Clin Neuromuscul Dis. 2006;7(3):97-103.
20 Sunderland S. The anatomy and physiology of nerve injury. Muscle Nerve. 1990; 13(9):771-84.
21 Chhabra A, Williams EH, Wang KC, Dellon AL, Carrino JA. MR neurography of neuromas related to nerve injury and entrapment with surgical correlation. AJNR Am J Neuroradiol. 2010;31(8):1363-8.
22 Byun WM, Park WK, Park BH, Ahn SH, Hwang MS, Chang JC. Guillain-Barre syndrome: MR imaging findings of the spine in eight patients. Radiology. 1998;208(1):137-41.
23 Yikilmaz A, Doganay S, Gumus H, Per H, Kumandas S, Coskun A. Magnetic resonance imaging of childhood Guillain-Barre syndrome. Childs Nerv Syst. 2010;26(8): 1103-8.
24 Koller H, Kieseier BC, Jander S, Hartung HP. Chronic inflammatory demyelinating polyneuropathy. N Engl J Med. 2005; 352(13): 1343-56.

Contact

Avneesh Chhabra, M.D.
Associate Professor Radiology
& Orthopaedic Surgery
Section Chief, Musculoskeletal Radiology
UT Southwestern Medical Center
5323 Harry Hines Blvd
Dallas, TX 75390-9178, USA
avneesh.chhabra@UTSouthwestern.edu
Adjunct Professor, Johns Hopkins University

3T MR Imaging of the Pediatric Cartilage Using 3D Dual Echo Steady State (DESS)

Shivani Ahlawat, M.D.[1]; Abraham Padua, Jr[2]; Thierry A G M Huisman, M.D.[3]; John A Carrino, M.D. MPH[1]

[1]The Russel H. Morgan Department of Radiology and Radiological Science, Johns Hopkins University School of Medicine, Baltimore, MD, USA
[2]Siemens Medical Solutions, Malvern, PA, USA
[3]Division of Pediatric Radiology, Russell H. Morgan Department of Radiology and Radiological Science, Bloomberg Children's Center, The Johns Hopkins Hospital, Baltimore, MD, USA

Introduction

Hyaline cartilage development is essential in pediatric musculoskeletal growth. Although in an adult patient, we focus solely on the articular cartilage, in the pediatric population, the articular, epiphysial and physial cartilage play an important role in skeletal maturation. The epiphysial and physial cartilage participate in enchondral ossification and contribute to a child's longitudinal growth while the articular cartilage buffers and transmits forces across joints. Although functionally and anatomically different, the three different types of cartilage in the pediatric population are histologically alike.

Magnetic resonance imaging (MRI) is the ideal modality for the assessment of pediatric* cartilage due to its lack of ionizing radiation and inherent excellent soft tissue contrast [1].

An optimal MRI sequence designed specifically for imaging hyaline cartilage should be able to accurately detect cartilage thickness and volume, characterize subtle morphological alterations as well as assess the adjacent bone. Three-dimensional (3D) MRI with isotropic, high resolution voxels is suitable for the pediatric population because it enables the radiologist to perform multiplanar reformats after a single sequence acquisition. This approach will also reduce scan time, which enhances the child's compliance.

3T MR scanners with multichannel dedicated coils allow obtaining image data with high signal-to-noise ratio (SNR) and contrast-to-noise ratio (CNR) [2]. Conventional spin echo and turbo spin echo sequences (T1, T2, and intermediate-weighted Proton Density sequences with or without fat suppression) as well as gradient echo techniques (incoherent GRE sequence, such as FLASH and coherent or steady state sequence, such as DESS) have been used for many years in cartilage imaging.

In this article, we will discuss the technical considerations as well as various clinical applications of Dual Echo Steady State (DESS) in imaging of the pediatric articular, epiphysial and physial cartilage on the 3T MAGNETOM Verio (Siemens Healthcare, Erlangen, Germany).

*Siemens disclaimer: MR scanning has not been established as safe for imaging fetuses and infants less than two years of age. The responsible physician must evaluate the benefits of the MR examination compared to those of other imaging procedures.

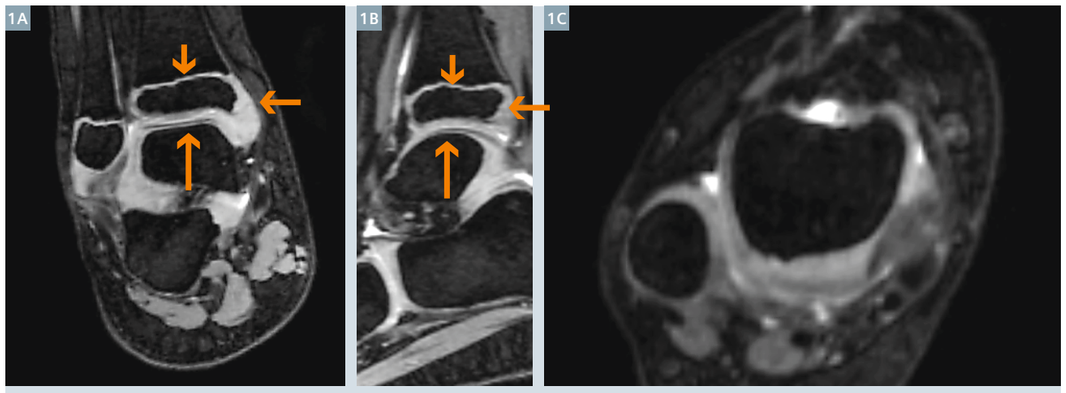

1 8-year-old boy with normal physial (short arrow), epiphysial (medium arrow) and articular cartilage (long arrow) on DESS images (TR 12.8 ms, TE 4.7 ms, SL 0.5 mm, FOV 9.4 × 9.4 cm, matrix 320 × 320, FA 45 degrees, acquisition time 6 minutes 18 seconds). Note the intermediate signal of the hyaline cartilage relative to the bright signal of the synovial fluid. Single 3D volumetric acquisition allows for multiplanar reformats for more convenient viewing of complex anatomical surfaces.

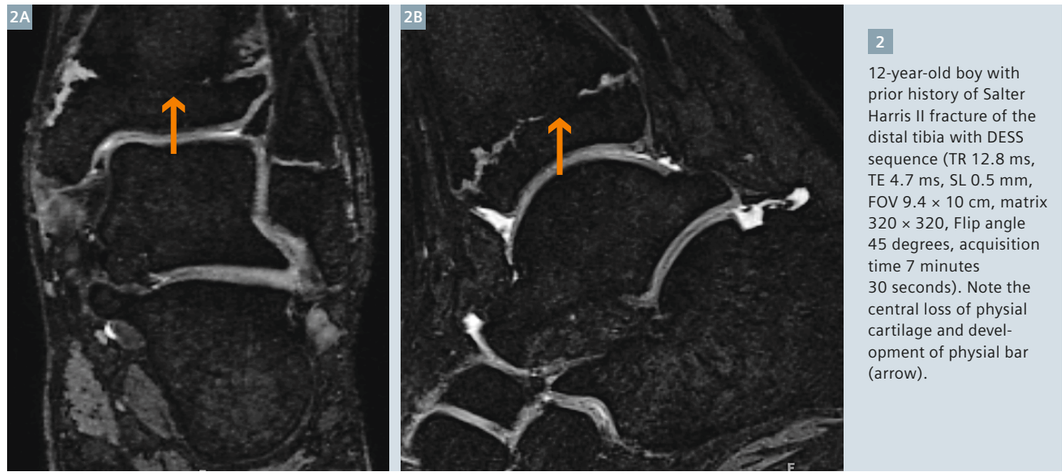

2 12-year-old boy with prior history of Salter Harris II fracture of the distal tibia with DESS sequence (TR 12.8 ms, TE 4.7 ms, SL 0.5 mm, FOV 9.4 × 10 cm, matrix 320 × 320, Flip angle 45 degrees, acquisition time 7 minutes 30 seconds). Note the central loss of physial cartilage and development of physial bar (arrow).

Technical considerations

Dual Echo Steady State (DESS) is a 3D coherent (steady state) gradient echo sequence. Steady state sequences (FISP, TrueFISP, DESS, PSIF, CISS) share two major characteristics. Firstly, a short repetition time (TR) prevents transverse magnetization to decay before the next radiofrequency (RF) pulse is applied. Secondly, the slice or slab selective RF pulse is evenly spaced. When phase-coherent RF pulses with the same flip angle are applied with a constant TR that is shorter than the T2 of the tissue, a dynamic equilibrium is achieved between transverse magnetization (TM) and longitudinal magnetization (LM) [3]. Once this equilibrium is reached, two types of echoes and therefore two types of MR images are produced. The first type is post excitation signal (S+ or FISP (fast imaging steady state precession)) that consists of free induction decay (FID) arising from the most recent RF pulse. The second type is an echo reformation that occurs prior to excitation (S– or PSIF (reversed FISP)) and results when residual echo is refocused at the time of the subsequent RF pulse [4, 5]. DESS combines S+ and S– signals into one. High T2 contrast is obtained due to the PSIF contribution; whereas, morphological images are obtained by the FISP contribution. The variable T2-weightings of both echoes allow the calculation of quantitative T2. Therefore, the DESS sequence combines morphological and functional analysis from the same data set with high resolution in a relatively short imaging time [6].

In DESS, two or more gradient echoes are acquired. Each of these group of echoes are separated by a refocusing pulse and the combined data results in higher T2*-weighting, creating high signal in cartilage and synovial fluid [7]. The most important parameter which needs to be kept in mind while acquiring a DESS is the flip angle (FA). According to Hardy et al. [8], the appropriate flip angle for the 3D DESS sequence is 60 degrees which allows for high SNR and CNR.

Although hyaline cartilage is intermediate signal intensity and synovial fluid is high signal intensity in both 2D fat suppressed turbo spin echo proton density and 3D DESS, slice thickness is thinner in 3D DESS suggesting that this technique may detect smaller cartilage defects than the 2D technique (Fig. 1). Water excited or fat suppressed 3D gradient echo imaging is recommended for measuring the exact cartilage thickness without partial volume artifacts, even though the contrast-to-noise ratio between cartilage and bone marrow is relatively poor [9]. Chemical shift artifact can affect the cartilage-bone interface and fat suppression helps to reduce this, of particular importance in the physial cartilage.

The disadvantages of 3D gradient echo imaging techniques are relatively long scan time. In addition, fat suppressed turbo spin echo proton density is superior for intra-articular and periarticular structures and is obtained in short imaging time, but it has the previously mentioned disadvantage of partial volume effects.

Clinical applications

3D DESS allows quantitative assessment of cartilage thickness and volume with good accuracy and precision [10]. Although there have been longitudinal studies in adults regarding accuracy of DESS sequence in assessing the articular cartilage, there are no large comparative studies in the pediatric population [11]. We will discuss the potential applications of the DESS technique in assessment of pediatric epiphsyial, physial and articular hyaline cartilage.

Congenital: Skeletal dysplasias affect the normal epiphysial cartilage zonal architecture [12, 13] and may manifest on MRI as disruptions in the zone of provisional calcification. Neonates with cartilage abnormalities, such as achondrogenesis and type II hypochondrogenesis, have shown a significant increase in the number and size of the epiphysial vascular channels [14, 15].

In the setting of tarsal coalition, DESS can potentially be useful in distinguishing fibrous from cartilaginous fusion. In addition the volumetric 3D acquisition allows for multiplanar reformats which can be useful in assessment of complex subtalar joint morphology.

Metabolic: Metabolic disturbances, such as rickets and scurvy, can result in abnormal epiphysial cartilage development.

Trauma: The physis is a relatively weak region and is easily damaged by trauma, infection, tumor invasion, ischemia, radiation, metabolic and hematologic disorders, electrical and thermal burns, and frostbite [11, 12, 16–22]. Traumatic physial injuries may be seen in the various types of Salter-Harris fractures [22]. Generally, the frequency of growth arrest is directly proportional to the increasing Salter-Harris number [17]. Angular deformity such as in Blount disease, altered joint mechanics, leg-length discrepancy, and long-term disability can also result from injury to the physis at weight-bearing sites, such as the knees [16, 17].

Vertical physial injuries crossing growth plates can result in transphysial vascular communication. This communication can lead to the formation of bony bridges (Fig. 2). The DESS is ideal for assessment of physial bridges due to isotropic acquisition which can be used to generate multiplanar reformations and axial maximum-intensity-projection maps of the physial plate, all of which show high-signal cartilage interrupted by a low-intensity physial bridge [16–18]. Metaphysial vascular injury can result in the arrest of endochondral ossification and thickening of the injured physes (as in gymnast's wrist) [17].

Osteochondritis dissecans (OCD) is an acquired disorder of bone in which there is fragmentation of the subchondral bone with varying degrees of articular cartilage involvement. The etiology is likely related to indirect trauma in most cases. The most common locations for OCD are the femoral condyles, talar dome and capitellum. In the growing child, irregular but normal epiphysial cartilage ossification must be distinguished from an OCD. The variants will have normal overlying cartilage and no associated marrow edema and are commonly located in the posterior lateral femoral condyle. Capitellar OCD is frequently found in young teenagers, particularly pitchers and gymnasts. OCD usually occurs in the anterolateral portion and must be distinguished from the normal pseudodefect in the posterior capitellum. Fluid signal at the bone-osteochondral lesion interface as well as a loose intra-articular body herald lesion instability.

Idiopathic: Legg Calve Perthes disease (LCP) is an idiopathic cause of hip pain and limp in preadolescent children due to osteonecrosis (or osteochondrosis) of the femoral epiphysis. In the avascular phase, DESS can be used to assess acetabular cartilage and labral hypertrophy (Fig. 3). In the revascularization and reparative phase, findings that suggest possible physial involvement by LCP disease include increased undulation of the growth plate (W- or M-shaped), deepening of the growth plate or 'cupping', epiphysial–metaphyseal osseous fusion (bone bridge or bar formation across the physis), or physial cystic change [23].

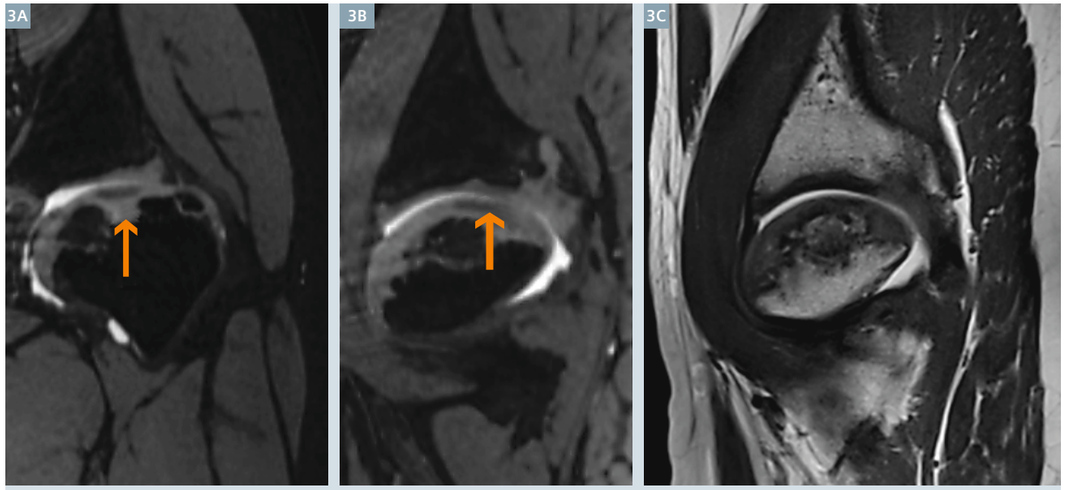

3 7-year-old boy with left hip Leff Calve Perthes disease with coronal and sagittal DESS images (TR 12.9 ms, TE 5 ms, SL 0.75 mm, FOV 24 × 24 cm, matrix 256 × 240, flip angle 25 degrees, acquisition time 4 minutes 20 seconds). Although there is coxa magna and plana, there is also formation of fibrocartilage (arrow) within the central femoral articular cartilage. The sagittal FSPD sequence (TR 5171 ms, TE 36 ms, SL 3.0 mm /3.3 sp, FOV 18 × 19 cm) does not demonstrate the cartilage signal heterogeneity to the same advantage.

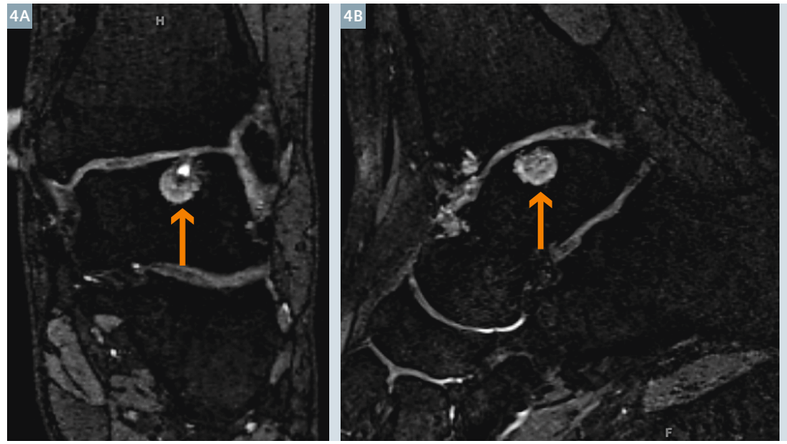

4 19-year-old young woman with remote history of septic arthritis on DESS sequence (TR 12.8 ms, TE 4.69 ms, SL 0.5 mm, FOV 9.4 × 10 cm, FA 45 degrees, acquisition time 6 minutes 18 seconds). The entire tibiotalar hyaline cartilage demonstrates diffuse intermediate grade thinning with large central lateral talar dome subchndral cyst (arrow).

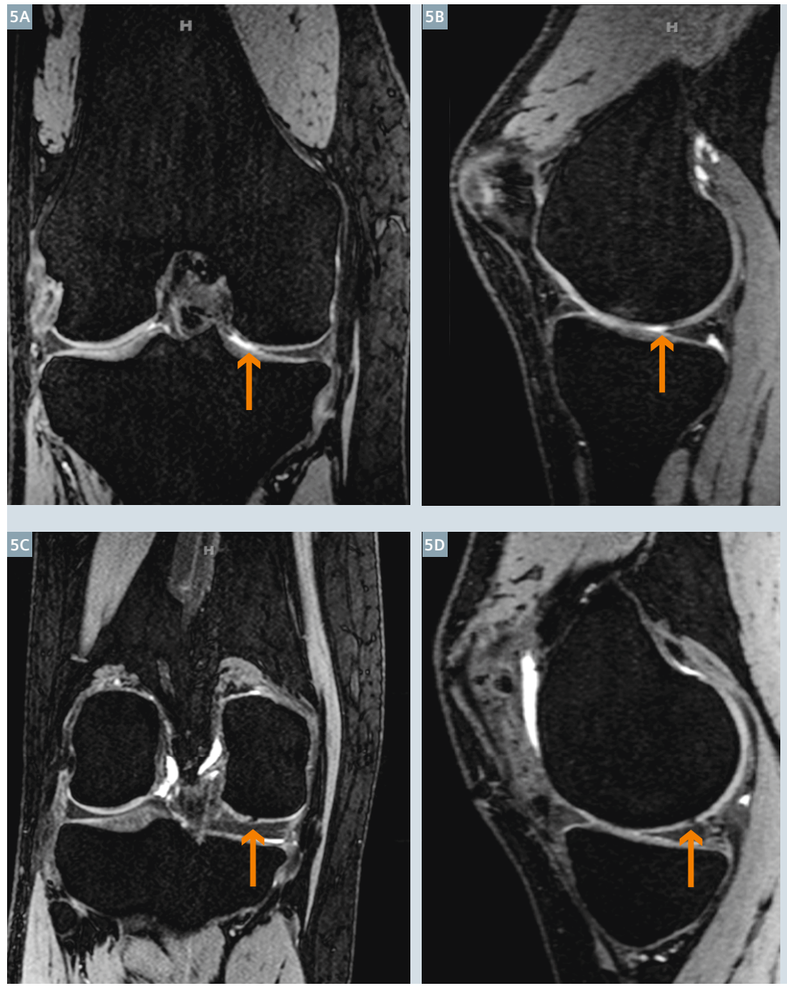

5 16-year-old girl with high grade defect in the right central medial femoral condyle (arrow) on the preoperative MRI with DESS sequence (TR 14.1 ms, TE 5 ms, SL 0.6 mm, FA 25 degrees, FOV 15 × 15 cm, matrix 512 × 512, acquisition time 3 minutes 36 seconds). The patient underwent autologous chondrocyte implantation of the high grade defect in the central medial femoral condyle. Postoperative MRI with DESS (TR 14.1 ms, TE 5 ms, SL 0.6 mm, FA 25 degrees, FOV 15 × 15 cm, matrix 512 × 512, acquisition time 3 minutes 36 seconds) shows repair cartilage tissue that is homogeneous in signal intensity and flush with native cartilage with small focus of hypointense fibrocartilage formation (arrow). Note normal subchondral bone plate and interval resolution of minimal subchondral edema noted on the preoperative MRI.

Inflammation/Infection: Hyaline cartilage damage can also result from inflammatory conditions such as juvenile idiopathic arthritis as well as infection (Fig. 4). Sequelae of osteochondral injury include total-thickness loss of articular and epiphysial cartilage, cartilage contour irregularity, and intrinsic signal heterogeneity.

Post-operative: MRI is also used to follow cartilage repair procedures, such as microfracture, osteochondral autografts and allografts, and autologous chondrocyte implantation. The DESS sequence can assess cartilage repair via evaluation of repair tissue signal characteristics, border integration, thickness relative to native cartilage, chondral clefts and changes within the subchondral bone plate (Fig. 5).

Conclusions

The physial, epiphysial and articular hyaline cartilage is affected in various congenital, post-traumatic, idiopathic and inflammatory conditions in children. 3D DESS techniques have many advantages in assessment of pediatric cartilage pathology including higher SNR, increased cartilage-to-fluid contrast and isotropic resolution, which helps to reduce partial volume effects. 3D DESS techniques are also of essential importance in the pediatric population due to the lack of ionizing radiation.

References

1 Gold GE, Chen CA, Koo S, Hargreaves BA, Bangerter NK. Recent advances in MRI of articular cartilage. AJR Am J Roentgenol 2009 Sep;193(3):628-638.
2 Kornaat PR, Reeder SB, Koo S, Brittain JH, Yu H, Andriacchi TP, et al. MR imaging of articular cartilage at 1.5T and 3.0T: comparison of SPGR and SSFP sequences. Osteoarthritis Cartilage 2005 Apr;13(4):338-344.
3 Chavhan GB, Babyn PS, Jankharia BG, Cheng HM, Shroff MM. Steady-State MR Imaging Sequences: Physics, Classification, and Clinical Applications1. Radiographics July-August 2008 July-August 2008;28(4):1147-1160.
4 Gyngell ML. The application of steady-state free precession in rapid 2DFT NMR imaging: FAST and CE-FAST sequences. Magn Reson Imaging 1988 Jul-Aug;6(4):415-419.
5 Bruder H, Fischer H, Graumann R, Deimling M. A new steady-state imaging sequence for simultaneous acquisition of two MR images with clearly different contrasts. Magn Reson Med 1988 May;7(1):35-42.
6 Welsch GH, Scheffler K, Mamisch TC, Hughes T, Millington S, Deimling M, et al. Rapid estimation of cartilage T2 based on double echo at steady state (DESS) with 3 Tesla. Magn Reson Med 2009 Aug;62(2):544-549.
7 Crema MD, Roemer FW, Marra MD, Burstein D, Gold GE, Eckstein F, et al. Articular Cartilage in the Knee: Current MR Imaging Techniques and Applications in Clinical Practice and Research. Radiographics January-February 2011 January-February 2011;31(1):37-61.
8 Hardy PA, Recht MP, Piraino D, Thomasson D. Optimization of a dual echo in the steady state (DESS) free-precession sequence for imaging cartilage. J Magn Reson Imaging 1996 Mar-Apr;6(2):329-335.
9 Gold GE, McCauley TR, Gray ML, Disler DG. Special Focus Session. Radiographics 2003 September 01;23(5):1227-1242.
10 Eckstein F, Hudelmaier M, Wirth W, Kiefer B, Jackson R, Yu J, et al. Double echo steady state magnetic resonance imaging of knee articular cartilage at 3 Tesla: a pilot study for the Osteoarthritis Initiative. Ann Rheum Dis 2006 Apr;65(4):433-441.
11 Wirth W, Nevitt M, Hellio Le Graverand MP, Benichou O, Dreher D, Davies RY, et al. Sensitivity to change of cartilage morphometry using coronal FLASH, sagittal DESS, and coronal MPR DESS protocols – comparative data from the Osteoarthritis Initiative (OAI). Osteoarthritis Cartilage 2010 Apr;18(4): 547-554.
12 Jaramillo D, Connoly SA, Mulkern RV, et al. Developing epiphysis: MR imaging characteristics and histologic correlation in the newborn lamb. Radiology 1998; 207:637–645.
13 Li X, Wang R, Li Y, Tang L, Xu A, Hu J. MRI characteristics and transverse relaxation time measurements in normal growing cartilage. J Huazhong Univ Sci Technolog Med Sci 2004; 24:411–413.
14 Cairns R. Magnetic resonance imaging of the growth plate: pictorial essay. Can Assoc Radiol J 2003; 54:234–242.
15 Gruber HE, Lachman RS, Rimoin DL. Quantitative histology of cartilage vascular canals in the human rib: findings in normal neonates and children, and in achondrogenesis II-hypochondrogenesis. J Anat 1990; 173:69–75.
16 Oeppen RS, Jaramillo D. Sports injuries in the young athlete. Top Magn Reson Imaging 2003; 14:199–208.
17 12. Li X, Wang R, Li Y, et al. Epiphysial and physial cartilage: normal gadolinium-enhanced MR imaging. J Huazhong Univ Sci Technolog Med Sci 2005; 25:209–211.
18 Sailhan F, Chotel F, Guibal AL, et al. Three-dimensional MR imaging in the assessment of physial growth arrest. Eur Radiol 2004; 14:1600–1608.
19 Ogden JA. The evaluation and treatment of partial physial arrest. J Bone Joint Surg Am 1987; 69:1297–1302.
20 Peterson HA. Partial growth plate arrest and its treatment. J Pediatr Orthop 1984; 4:246–258.
21 Ogden JA. Injury to the growth mechanisms. In: , Ogden JA, ed. Skeletal injury in the child, 2nd ed. Philadelphia, PA: Saunders, 1990: 97–173 .
22 Salter R, Harris W. Injuries involving the epiphysial plate. J Bone Joint Surg Am 1963; 45:587–622.
23. Dillman J and Hernandez R. MRI of Legg-Calve-Perthes disease. AJR 2009 193:5, 1394-1407.

Contact

John A. Carrino, M.D., M.P.H.
Associate Professor of Radiology
and Orthopaedic Surgery
The Russel H. Morgan
Department of Radiology
and Radiological Science
Johns Hopkins University
School of Medicine
601 North Caroline St. / JHOC 5165
Baltimore, MD
USA
carrino@jhmi.edu

Time-Resolved MR Angiography using TWIST for Evaluation of Peripheral Vascular Malformations in Children

Tanja Zitzelsberger, Ilias Tsiflikas, Jürgen Schäfer, Ulrich Kramer

University Hospital Tübingen, Department of Diagnostic and Interventional Radiology, Tübingen, Germany

Abstract

Vascular anomalies are classified into vascular tumors (infantile hemangioma) and vascular malformations. Vascular malformations are divided into slow flow and high flow subtypes. Magnetic resonance imaging (MRI) and contrast-enhanced dynamic magnetic resonance angiography (MRA) both help in classification and the assessment of extent and distribution. Nevertheless, digital subtraction angiography (DSA) remains the gold standard and is pivotal in the assessment of fine vascular details and treatment planning.

Introduction

Most patients with vascular anomalies are asymptomatic and do not require therapy. Nevertheless, a significant number do suffer from pain, swelling, functional impairment, or cosmetically severe deformity reducing quality of life.

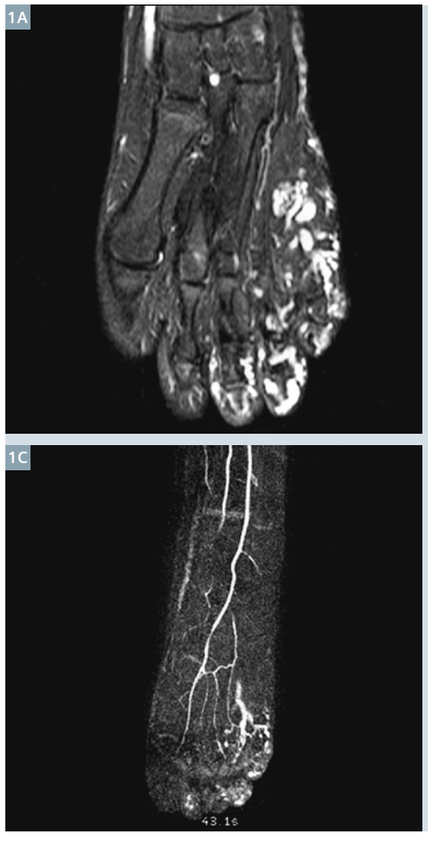

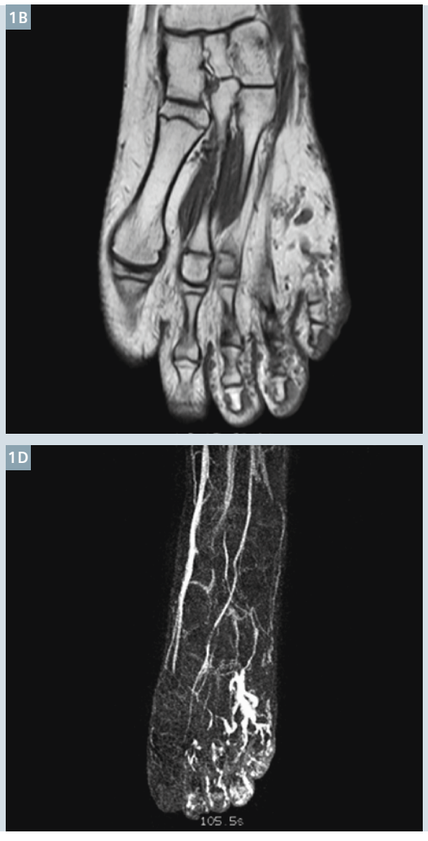

1 14-year-old male with arteriovenous malformation in the plantar soft tissues of the left lateral forefoot. Coronal STIR **(1A)** and T1-weighted **(1B)** images demonstrate a large number of prominent arteries and arterioles in the subcutaneous layer with fat interspersed within the lesion. Dynamic time-resolved MR angiography provides excellent depiction of hemodynamics of this vascular malformation **(1C, D)**. Note the early enhancing pattern as well as presence of dilated or early draining veins (as a consequence of arteriovenous shunting) on time-resolved MR angiography.

Vascular anomalies can present as a tiny lesion involving only the skin or the subcutaneous layer, or as a large lesion that involves deeper layers, including muscles, bones and even multiple other organs. Over the past decades, nomenclatures for vascular anomalies continued to cause confusion and create obstacles between the various medical subspecialities involved in the management of these patients (pediatricians, dermatologists, surgeons, interventional radiologists, angiologists, pathologists, etc.) potentially leading to an inaccurate diagnosis and mismanagement.

The understanding of vascular malformations was revolutionized in 1982, when Mulliken and Glowacki introduced a classification system for vascular malformations based on the biologic and pathologic features [2]. In 1996, the International Society for the Study of Vascular Anomalies (ISSVA) anticipated a classification that would encompass the clinical, histological and pathophysiological characteristics of vascular anomalies: Hemangiomas and vascular malformations. Hemangiomas are benign vascular tumors of infancy and childhood characterized by an initial rapid growth of endothelial cells and subsequent slow involution. By contrast, vascular malformations (VMs) delineate congenital lesions formed of dysplastic vascular channels without any endothelial proliferation or spontaneous regression. VMs are usually caused by an arrest of normal vascular development and failure of resorption of the embryologic primitive vascular elements.

Compared to hemangiomas, VMs present with a lower overall prevalence of 1.5% in the general population [1]. They can occur in every part of the body, but the most common anatomic locations – beside the craniofacial manifestations, where 60% of the lesions are found – are the pelvis and the extremities (flexor muscle of the forearm and the quadriceps muscle). VMs are already present at birth and usually grow proportionally to the child. They were further subdivided either within their origin (consisting of capillary, venous, arterial, lymphatic and fistulous networks) or within their flow patterns. In general, capillary, lymphatic and venous malformations or mixed lesions are classified as low-flow malformations, whereas any malformation with arterial component is classified as high-flow malformation, including congenital arteriovenous malformations (AVMs), arteriovenous fistula (AVF) and acquired vascular lesions [2]. Several genetic defects responsible for the inherited forms of vascular anomalies and associated syndromes have been identified over the last decade [3].

An accurate classification of the vascular anomalies and the evaluation of the full anatomical extent are critical since the treatment options and morbidity are significantly different for the various groups of vascular malformations.

Diagnosis

MRI and ultrasonography (US) are the non-invasive techniques of choice for the evaluation of vascular anomalies. US, including Doppler Imaging, is primarily used as the initial diagnostic tool. It identifies the flow pattern of these vascular anomalies and divides them into slow- or high-flow lesions. US does not require any sedation of the patient. Because of the lack of radiation, high soft-tissue contrast, and the capability of dynamic contrast-enhanced images to reflect the hemodynamic of the anomalies, MRI and dynamic contrast-enhanced MR-Angiography (MRA) are, along with the clinical history and a physical examination, decisive in the evaluation of vascular anomalies, especially in children. Dynamic MRA enables the identification of the extent of involvement and provides a pre-procedural road map. Recent advances such as phased-array coils and parallel imaging techniques have made faster scanning with high temporal resolution possible. T1-weighted turbo spin echo (TSE) sequences define anatomic location, T2-weighted TSE sequences show the flow voids and vascular structures, and short tau inversion recovery (STIR) sequences are very useful in detecting the extent of the lesion over a dark background of surrounding structures. Furthermore, MRI can be used to distinguish vascular tumors from cystic lesions.

In general, evaluation of vascular anomalies requires delineation of its components:
(1) Localization, size and tissue involvement;
(2) Origin, orientation and course of feeding arteries; and
(3) Origin, size and course of draining veins.

Within the last few years continuous improvement in hard- and software, particularly time-resolved MRA, has led to increased acceptance as a practical alternative to DSA for the diagnosis and determination of appropriate treatment of vascular anomalies. Time-resolved MRA can be used accurately to distinguish between the different types of vascular anomalies [4].

MR imaging

Patients with suspected or known vascular anomalies were studied using a 3D time-resolved MRA, incorporating Generalized Autocalibrating Partially Parallel Acquisitions (GRAPPA) and echo sharing schemes, Time Resolved Imaging with Stochastic Trajectories (TWIST). Examinations were performed on a 1.5T MR imaging system (MAGNETOM Avanto, Siemens Healthcare, Erlangen, Germany). For signal reception we used either a multi-channel phased-array surface coil or dedicated flex extremity coils.

For morphological imaging, all scans consisted of T1-weighted as well as fat-suppressed T2-weighted images. Axial images were obtained by using 3–6 mm section thickness, 1–2 mm intersection spacing, and variable fields-of-view depending on the region-of-interest. After intravenous administration of single dose Gadobutrol (Gadovist®, Bayer HealthCare, Germany), post-contrast images were performed in axial and sagittal and/or coronal plane.

Time-resolved MRA using TWIST

The TWIST sequence divides the *k*-space into two regions. The central region A (low frequencies) defines the contrast in the image and the peripheral region B (high frequencies) adds detail information in the

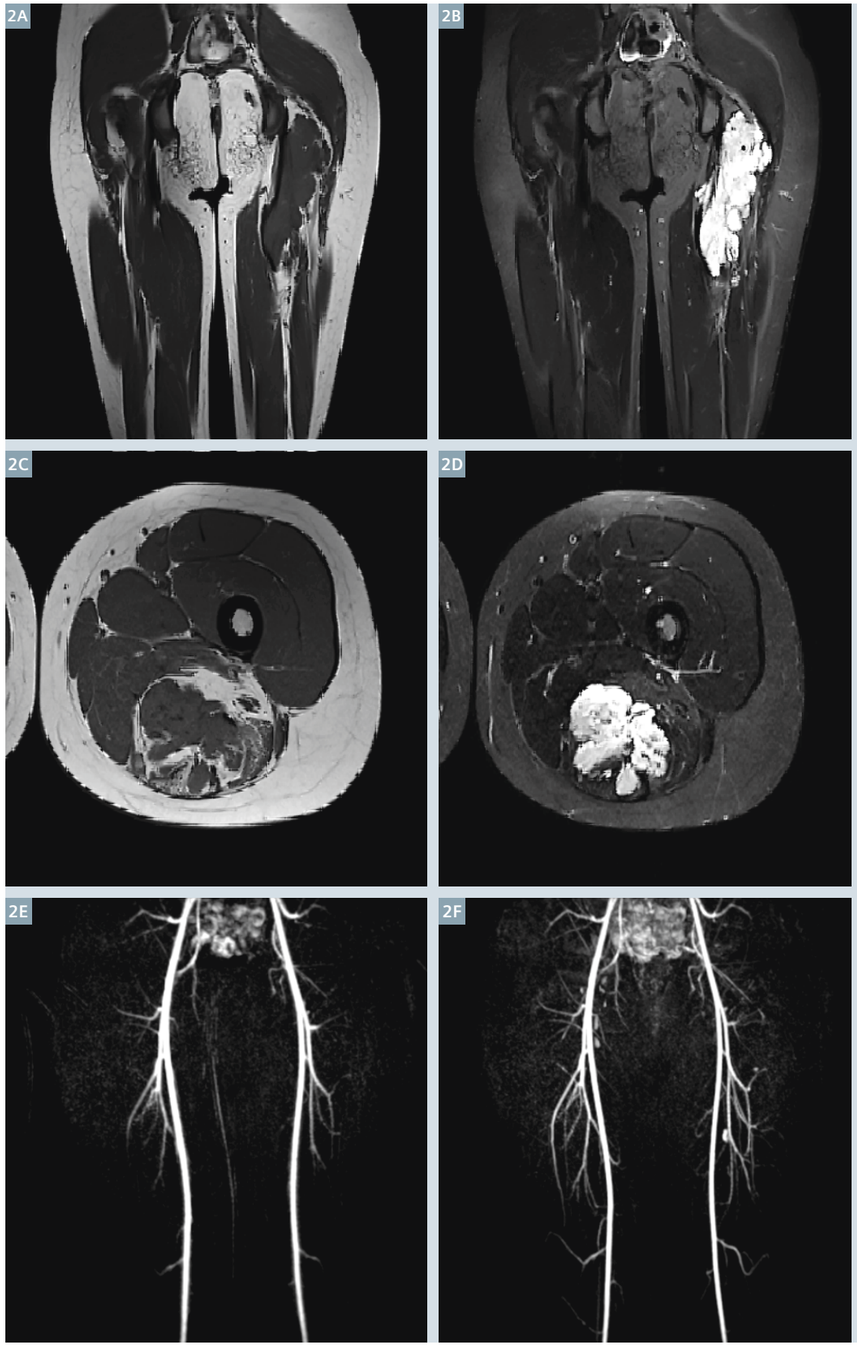

2

9-year-old girl with recurred clinical symptoms caused by a hemangioma of the left proximal thigh. She underwent prior sclerotherapy several years before. She currently suffers from local pain and limited exercise tolerance. On MR images there is no involvement of the skin or subcutaneous tissues. Coronal and axial T1-weighted **(2A, C)** and T2-weighted STIR **(2B, D)** images show a well-defined lobulated mass within the quadratus femoris as well as the gluteus maximus muscle. No perilesional edema is identified. On time-resolved MR angiography **(2E, F)** neither early enhancement nor arteriovenous shunting can be seen.

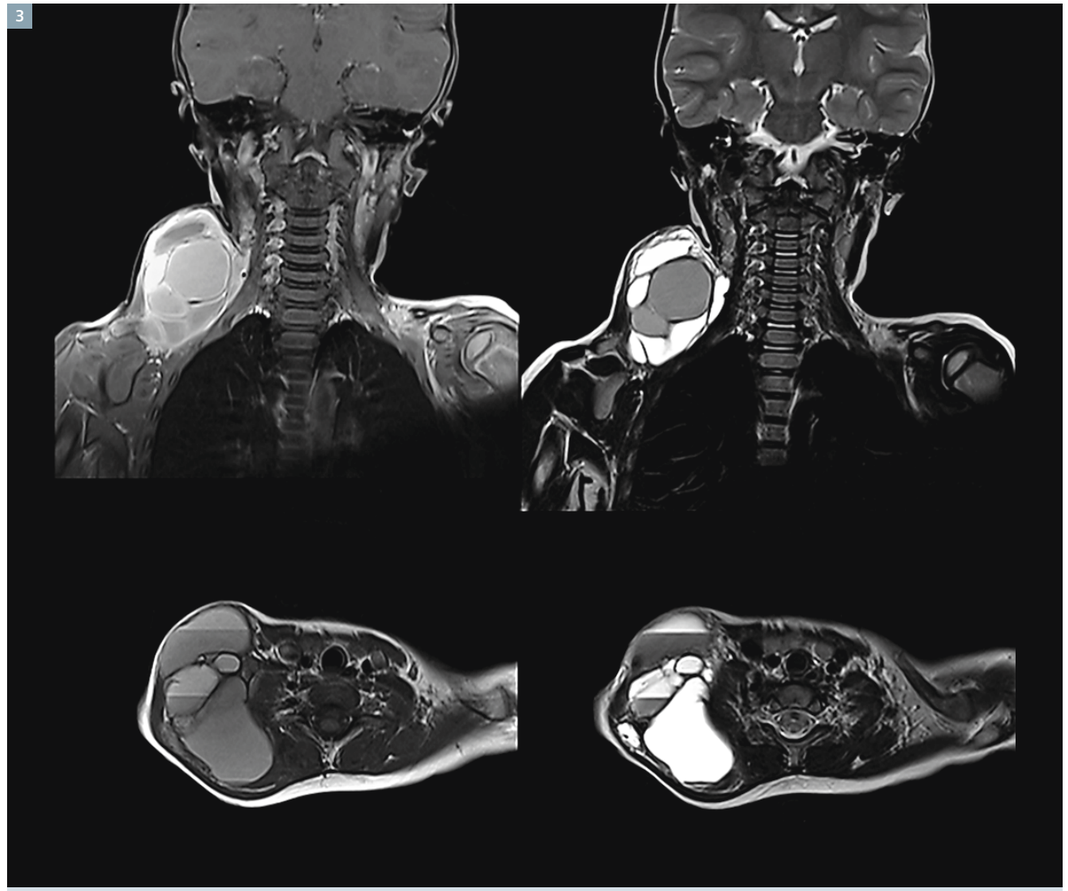

3 3-year-old boy with macrocystic lymphatic malformation in the right head and neck area. Images show well-defined, multilobulated and septated lesion predominantly involving the subcutaneous tissue. The increased signal intensity in T1-weighted images is most likely related to high proteinaceous component. The lesion is highly hyperintense on STIR images; internal fluid-fluid levels due to hemorrhage in some of the cysts can be found. Contrast-enhanced images reveal rim and septal enhancement and lack of filling of lymph-filled spaces. There was no enhancement on arterial or early venous contrast-enhanced MR angiography (not shown).

images. While region A is completely sampled in every measurement iteration, region B is undersampled by a factor of *n* (which can be varied by the operator). Due to a larger under-sampling factor the time difference for two subsequent acquisitions of the central region become smaller, which results in a higher temporal resolution in A. The *k*-space trajectory within region B follows a spiral pattern in the k_y-k_z plain with every trajectory in B slightly different, depending on the under-sampling factor *n*. During reconstruction, the missing data points in region B for a particular time frame t_i will be copied from the corresponding *k*-space trajectories in other time frames. The following sequence parameters were used: repetition time (TR) 2.3–3.5 ms, echo-time (TE) 0.8–1.3 ms (depending on patient adjustment), flip angle (FA) 25°, in-plane resolution 1.1 × 0.8 mm², slice thickness 1–3 mm. In our study we used a value of 15% for size A, and an under-sampling factor of 25% for region B.

Recently, time-resolved MRA has been observed to perform better than conventional MRA in classifying VMs and visualization of arterial feeders and draining veins [5]. Time-resolved MRA may potentially be employed as an initial diagnostic modality for these

4

Diffuse arteriovenous malformation of the right hand soft tissue in a 9-year-old girl. Clinical photograph shows a mass with the cutaneous aspect of a vascular anomaly **(4A)**. Coronal T2 STIR, T1-weighted as well as contrast-enhanced T1-weighted images with fat suppression **(4B)** show septated mass involving the subcutaneous tissue, the muscles and bones of the right thumb as well as forefinger. Early and late arterial phases during dynamic time-resolved MR angiography (**4C**: temp. resolution 2 sec) show multiple small prominent arteries with a few arterial aneurysms.

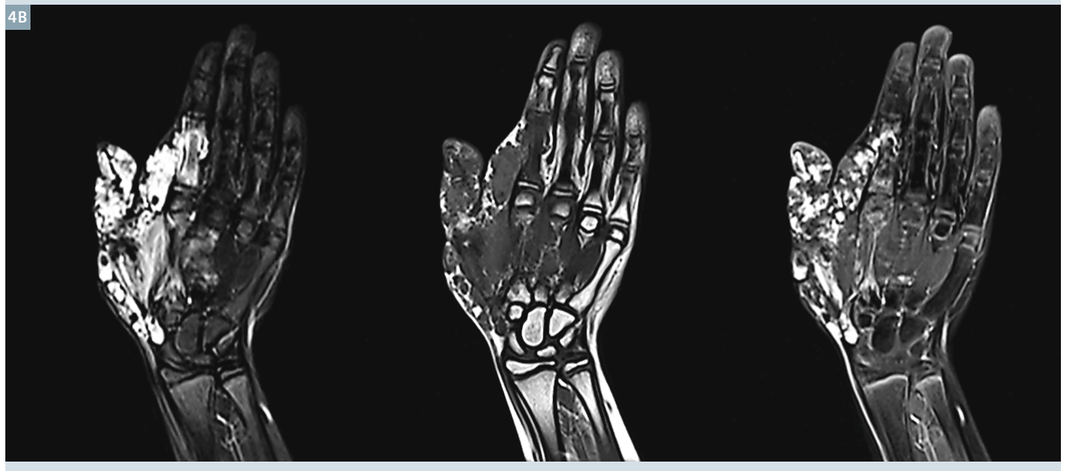

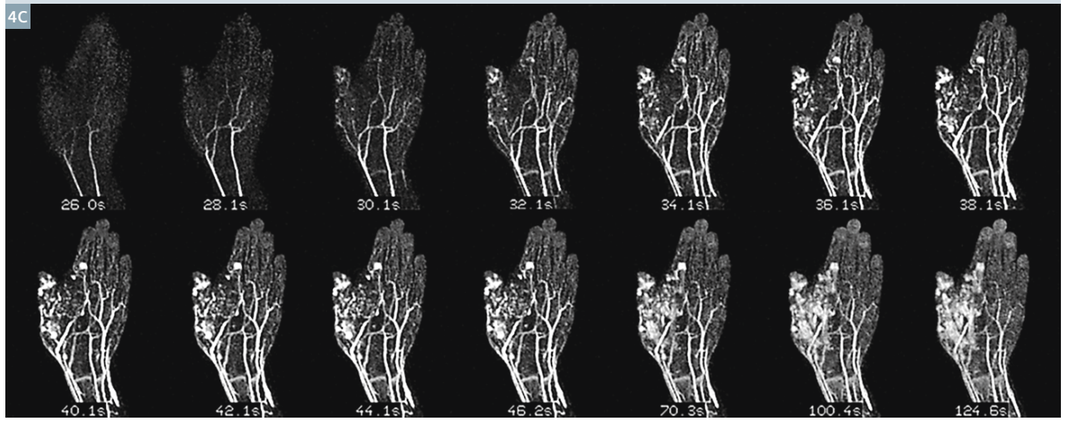

lesions. It also appears to be helpful in guiding treatment of these lesions by determining their extent. The drawback of time-resolved MRA is an under-estimation of shunt volumes in vascular malformations, which can be confidently evaluated on DSA.

Discussion

The TWIST technique provides information on the hemodynamics of vascular malformations, demonstrating the early filling of the lesion during the arterial phase of the acquisition as well as – if existing – the feeding artery. The use of parallel imaging techniques in association to the variable rate *k*-space sampling allows a reduction of acquisition time, improving the temporal resolution while maintaining and even improving the spatial resolution. In our study protocol the temporal resolution varied from 1.4 to 4.8 sec/frame and the spatial resolution ranged from 1.1 × 0.8 × 1.0 mm to 1.1 × 1.1 × 3.0 mm.

We used a high acceleration factor of 3 for parallel imaging in most applications. Thus, we have been able to achieve detailed anatomical and hemodynamic information similar not only to conventional high-spatial resolution MRA but also to that achieved with DSA, but without the risks associated with ionizing radiation exposure, iodizing contrast agents, or catheterization itself.

Clinical implication

Historically, diagnosis, treatment planning and follow up of VMs were based on ultrasound examination and invasive DSA for confirmation and interventional guidance. In the last decade MRI has become the modality of choice for the assessment and precise classification [6]. Time-resolved MRA allows characterization between VMs and their subtypes as well as extent of the lesion, tissue involvement and flow characteristics.

Conclusion

Vascular anomalies can show a variety of clinical manifestations. Therefore it is very important to categorize these lesions and to determine their extent. MRI and DSA are pivotal in the imaging of vascular anomalies. The primary role of MRI is to assess the extent, distribution and subtype, whereas DSA shows promise in delineating the vascular details of complex lesions and in decision-making regarding feasibility of sclerotherapy or embolization therapy. The understanding of clinical behavior and imaging features of vascular anomalies is essential in their accurate distinction, which might have a direct impact on their clinical management. In our experience, MR imaging and especially time-resolved MRA is a highly accurate tool for the evaluation of vascular anomalies prior to therapy decisions and a reasonable alternative to more invasive DSA.

References

1 Legiehn GM, Heran MK (2008) Venous malformations: classification, development, diagnosis and interventional radiologic management. Radiol Clin North AM 46: 545-597.

2 Mulliken JB, Glowacki J. (1982) Hemangiomas and vascular malformations in infants and children: a classification based on endothelial characteristics. Plast Reconstr Surg 69: 412-422.

3 Duffy K (2010) Genetics and syndroms associated with vascular malformations. Pediatr Clin North Am 57:1111-1120.

4 Rinker b. Karp NS, Margiotta M et al (2003) The role of magnetic resonance imaging in the management of vascular malformations of the trunk and the extremities. Plast Reconstr Surg 112: 504-510.

5 Kramer U, Ernemann U, Fenchel M et al (2011) Pretreatment evaluation of peripheral vascular malformations using low-dose contrast-enhanced time-resolved 3D MR angiography: initial results in 22 patients. AJR 196: 702-711.

6 Lee BB, Laredo J, Lee SJ et al (2007) Congenital vascular malformation: general diagnostic principle. Phlebology 22: 253-257.

Contact

Ulrich Kramer, M.D.
University Hospital Tübingen
Department of Diagnostic and Interventional Radiology
Hoppe-Seyler-Str. 3
72076 Tübingen
Germany
ulrich.kramer@med.uni-tuebingen.de

Fetal Cardiovascular MRI

Mike Seed, M.D.[1]; Christopher K. Macgowan, Ph.D.[2]

[1]Departments of Pediatrics and Diagnostic Imaging, Hospital for Sick Children, Toronto and University of Toronto, Canada
[2]Department of Physiology and Experimental Medicine, Hospital for Sick Children, Toronto and University of Toronto, Canada

Background and rationale

Intrauterine growth restriction (IUGR) is associated with changes in fetal cerebral, peripheral and placental vascular resistance resulting in circulatory redistribution commonly referred to as 'brain-sparing physiology' [1]. This is routinely identified through detection of velocity waveform changes in the cerebral and umbilical arteries using Doppler ultrasound [2]. However, animal studies suggest that chronic fetal hypoxia results in a reduction in fetal oxygen consumption (VO_2) that tends to normalize blood flow distribution, but which is nevertheless associated with delayed fetal growth and development [3, 4]. The detection of chronic IUGR might therefore be improved by the identification of reduced fetal VO_2 in the setting of normal Doppler findings. This could be particularly useful towards the end of the pregnancy, when the potential benefits of delivery from in utero hypoxia and starvation outweigh the risks of premature birth [5]. Late onset IUGR is currently difficult to detect because the typical Doppler changes seen in early onset intra-uterine growth restriction are frequently absent [6], and late gestation ultrasound measurements of fetal growth are less accurate.

Fetal VO_2 can be calculated when the oxygen content of blood in the umbilical artery and vein, and placental blood flow are known [7]. This has been achieved in human fetuses using invasive cordocentesis and ultrasound [8]. However, ultrasound measurements of vessel flow are prone to inaccuracy [9], and the risks associated with direct cordocentesis make it unsuitable for routine clinical use. We sought to develop cardiovascular magnetic resonance (CMR) techniques to assess fundamental elements of fetal cardiovascular physiology including oxygen delivery (DO_2), oxygen consumption (VO_2), and the distribution of blood flow and oxygen content in the major vessels of the fetal circulation. We present here our preliminary findings in the normal human fetal circulation.

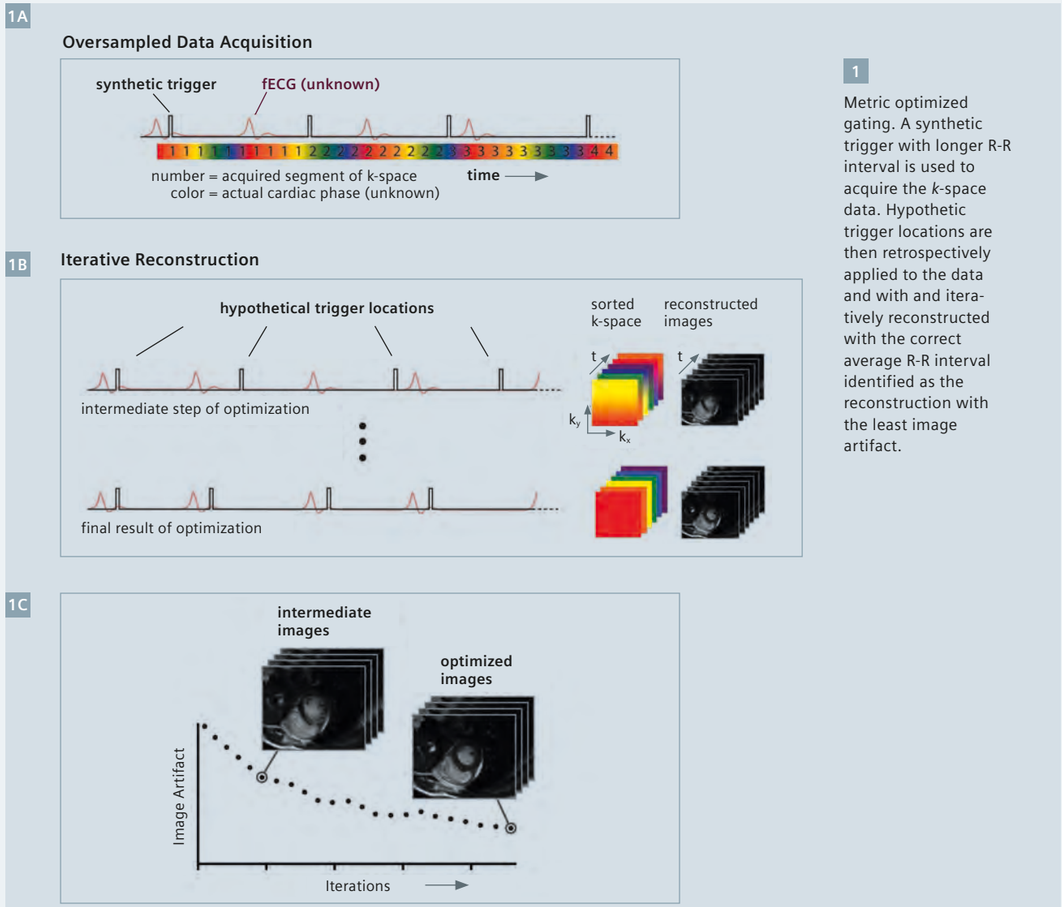

1 Metric optimized gating. A synthetic trigger with longer R-R interval is used to acquire the *k*-space data. Hypothetic trigger locations are then retrospectively applied to the data and with and iteratively reconstructed with the correct average R-R interval identified as the reconstruction with the least image artifact.

Theory

Techniques for measuring blood flow using phase-contrast (PC) MRI [10] and oxygen content using quantitative T2 MRI [11, 12] are well established, but imaging fetal* vessels requires modification of the existing techniques. Specific challenges include the small size of the vessels, the virtually constant movement of the fetus, and difficulty detecting the fetal electrocardiogram for cardiac triggering.

The latter can be overcome with alternatives to ECG gating such as self-gating [13] and cardiotocographic gating [14], which have both been shown to be feasible in fetal animal models. Alternatively, a retrospective technique can be used that acquires temporally oversampled data and then iteratively sorts the data using hypothetical ECG trigger times until artifact in the associated images is minimized [15]. This approach, which is illustrated in Figure 1, is termed metric optimized gating (MOG) and has been used successfully for PC MRI and steady state free precession (SSFP) cine imaging [16, 17].

Regarding fetal oximetry, a novel approach to myocardial T2 mapping with non-rigid motion correction has been developed by Giri et al., which holds promise for improving fetal MR oximetry in the presence of small fetal movements [18, 19]. This approach, currently available as a work-in-progress from Siemens**, may improve T2 accuracy by aligning target vessels across images used to construct a T2 map.

For fetal MRI, short scan times are essential to reduce artifact from gross fetal motion. As a result, there is a practical limit to the spatial resolution and signal-to-noise ratio that can be achieved. However, in our experience PC MR and T2 mapping techniques perform well in the majority of late gestation fetuses, whose vessel sizes are similar to neonates and whose body motion is partly restricted by the uterine walls.

Assuming a normal hematocrit, the PC MRI and T2 data may be used to calculate fetal DO_2 and VO_2 [7]. This requires calculation of the oxygen content, C, of umbilical venous (UV) blood, which is given by the equation:

$$C_{UV} = [Hb] \times 1.36 \times Y_{UV}$$

where Y_{UV} is the oxygen saturation of blood in the UV, and 1.36 is the amount of oxygen (ml at 1 atm) bound per gram of hemoglobin.

Fetal DO_2 can then be calculated from the product of UV flow (Q_{UV}) and C_{UV}. To calculate fetal VO_2, the arterio-venous difference in oxygen content (ΔC) between the UV and umbilical artery (UA) must be calculated, as follows:

$$\text{Fetal } VO_2 = Q_{UV} \times \Delta C_{UV\text{-}UA}$$

Because of the small size of the UA, the T2 in the descending aorta (DAo) is used for this calculation.

If it is assumed that the majority of the flow in the superior vena cava (SVC) is venous return from the brain then fetal cerebral VO_2 can also be approximated:

$$\text{Fetal cerebral } VO_2 = Q_{SVC} \times \Delta C_{AAo\text{-}SVC}$$

Fetal CMR methodology and protocol

Safety – The American College of Radiologists recommends fetal MRI only be used when alternative imaging techniques, namely ultrasound, are considered inadequate by the responsible imaging physician [20]. Contrast agents should be avoided due to the risk of toxicity to the fetus and where possible fetal MRI should be avoided in the first trimester. We follow the Siemens recommendation to limit the specific absorbtion rate (SAR) to 2 watts per kilogram ('normal mode'). A recent review reports that there is no evidence that MRI poses any risk to the mother or fetus [21].

Field strength – Fetal cardiovascular MRI can be performed on 1.5T and 3T systems. 1.5T systems are less prone to SSFP banding artifacts from field inhomogeneity. However, the increased SNR available at 3T makes PC imaging more robust, and facilitates MOG reconstruction. An important consideration is the effect of field strength on the relationship between T2 and blood oxygenation, with shorter T2 values encountered at 3T [22].

Patient positioning and coil selection – A body-matrix coil placed on the maternal abdomen, as close to the fetal thorax as possible, provides the best signal for fetal imaging. The addition of a second coil may help to improve signal across the whole field-of-view, particularly if the mother is in a lateral decubitus position, which many women find most comfortable in later on in pregnancy.

Gating – For MOG, an artificial gating trace is used in place of the actual fetal waveform. On Siemens systems this may be controlled using the IDEA command tool menu to define an R-R interval. For most fetuses an R-R interval of 545 ms, which corresponds to a heart rate of 110 beats per minute, will ensure that every heartbeat is oversampled.

Sequences – With the exception of the T2 mapping WIP**, the sequence parameters shown in Table 1 are based on commercially available Siemens

cardiac MRI sequences, and represent a possible approach to fetal CMR at 1.5T. For PC vessel flow quantification, we use a minimum of eight voxels over the vessel area and a temporal resolution of 50 ms. Adequate spatial resolution is also required for T2 measurements to avoid partial volume artifacts [23]. We use an interval of ~4 seconds (8 cardiac cycles) between T2 preparation pulses for T2 mapping to ensure adequate recovery of magnetization. Figure 1 shows how we orient the PC and T2 acquisitions for the target vessels.

Maternal hyperoxygenation – Investigators have used a trial of maternal hyperoxygenation (MH) to enhance fetal hemodynamic assessment, and maternal oxygen therapy has been proposed as a treatment for cardiac ventricular hypoplasia and IUGR. MH does not appear to be associated with any risk to the fetus or mother. One approach is to use a non-rebreather mask with 12 L/min of oxygen to administer an FiO_2 of 60–70%. Previous studies suggest oxygen should be given for 5–10 minutes prior to and during imaging [24].

Post processing

Flow – The MOG technique currently requires transfer of the raw data from the MRI to a computer for offline reconstruction using stand-alone software developed at our institution (MATLAB, Mathworks, USA). This software is available from our laboratory upon request. To quantify flow from the resulting PC MRI reconstructions, commercially available software is used (Q-flow, Medis, Netherlands).

Fetal weight – Flows are indexed to fetal weight based on a high-resolution 3D SSFP breath-hold acquisition covering the whole fetus to calculate the fetal volume. We use a combination of thresholding and other tools in Mimics (Materialise, Belgium) to segment the fetus. Fetal volume is converted to fetal weight using the conversion proposed by Baker (fetal weight (g) = 120 + fetal volume (ml) × 1.03) [25]. The same 3D SSFP acquisition can be used to calculate the volume and weight of individual fetal organs including the fetal brain, where brain weight (g) = brain volume × 1.04 [26].

Table 1:

Sequence	Type	Gating	Resp. comp.	Parallel Imaging factor	NSA	TE (ms)	TR (ms)	Slice thick (mm)	Matrix size	FOV (mm)	Temp. resol. (ms)	Scan time(s)
3D-SSFP	3D	–	Breath-hold	2	1	1.74	3.99	2	256 × 205 × 80	400	–	13
Static SSFP	2D	–		–	1	1.3	6.33	4	320 × 211	350	1336	24 (15 slices)
Cine SSFP	2D	MOG	–	2	1	1.26	3.04	5	340 × 310	340	46	55 (10 slices)
Phase contrast§	2D	MOG	–	–	1	3.15	6.78	3	240 × 240	240	54	36
T2 mapping†	2D	PG	–	2	1	1.15††	3.97††	6	224 × 181	350	4000	12

§ Velocity encoding sensitivity tailored according to vessel: 150 cm/s for arteries, 100 cm/s for veins and 50 cm/s for umbilical vein. Number of segments per cardiac cycle = 4

† T2 mapping used 4 T2 preparation times, tailored to span the expected T2 of a given vessel (0 ms, 0.33*T2, 0.66*T2, and 1.00*T2), with 4000 ms of magnetization recovery between successive T2 preparations.

†† Rapid imaging of the T2-prepared magnetization was performed using a single-shot SSFP sequence with the indicated TE/TR values.

NSA: number of signal averages, **TE**: echo time, **TR**: repetition time, **FOV**: field-of-view, **PG**: pseudo-gating (based on estimated R-R interval), **MOG**: metric optimized gating (R-R interval 545 ms)

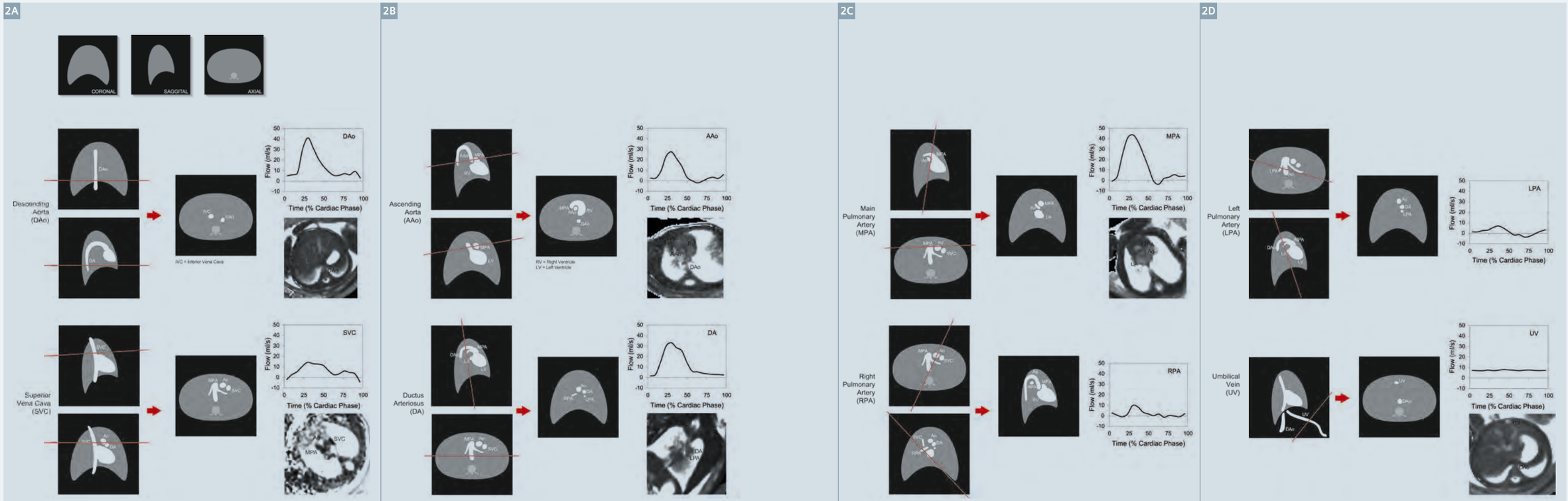

2 Slice prescriptions for fetal cardiovascular MRI. Orientation of slices for phase contrast and T2 mapping of the major fetal vessels based on 3-plane static SSFP survey of the fetal thorax showing representative flow curves and T2 maps.

Table 2:

	CVO	MPA	AAO	SVC	DA	PBF	DAO	UV	FO
Mean flow (ml/min/kg)	471	270	187	138	187	90	254	136	120
95th % CI	(376,595)	(174,376)	(120,261)	(82,200)	(97,205)	(18,182)	(181,338)	(97,205)	(9,255)
Modeled mean flow (% CVO)		57	40	29	41	16	52	29	27
Y (%)		58	63	48			57	82	

Mean flows and oxygen saturations (Y) in each of the major vessels in the human late gestation fetal circulation by MRI.

CVO: combined ventricular output, **MPA**: main pulmonary artery, **AAO**: ascending aorta, **SVC**: superior vena cava, **DA**: ductus arteriosus, **PBF**: pulmonary blood flow, **DAO**: descending aorta, **UV**: umbilical vein, **FO**: foramen ovale.

Table 3:

	DO_2	VO_2	CVO_2
Mean	20.4	6.4	3.6
SD	3.5	1.7	0.8

Mean fetal oxygen delivery (DO_2), oxygen consumption (VO_2) and cerebral oxygen consumption (CVO_2) in the late gestation human fetus by MRI (ml/min/kg).

T2 mapping – Regions- of-interest covering the central 50% of the vessel area are used for measuring T2. We currently convert the T2 values to saturations using the relationship described by Wright et al. for adult blood [11]. The accurate conversion of the T2 of blood to oxygen saturation is dependent on hemoglobin concentration [Hb]. We assume a fetal [Hb] of 15g/dL at 36-37 weeks [27].

Results

Tables 2 and 3 show the mean vessel flows and ranges of flows in 30 subjects (mean gestational age – 37 weeks, SD 1.2) by phase contrast MRI. We also present preliminary mean oxygen saturations, fetal DO_2 and VO_2 for eight subjects based on our preliminary experience with fetal vessel T2 mapping. Figure 3 represents the mean flows and oxygen saturations across the circulation. The findings are in keeping with previous estimations made regarding the human fetal circulation based on results of invasive measurements in fetal lambs and human ultrasound and cordocentesis results [7, 8].

Discussion

Interpretation of fetal cardiovascular MRI is currently limited to a few preliminary observations. Understanding the findings requires knowledge of normal fetal cardiovascular physiology. The normal fetal circulation operates in parallel with shunts at the foramen ovale and ductus arteriosus resulting in blood bypassing the fetal lungs. This is tolerated in the fetal circulation because gaseous exchange occurs at the placenta. The fetus exists in a relatively low oxygen environment, but also has lower oxygen consumption than the newborn due to lower demands for thermoregulation [7].

In fetal lambs, the oxygen saturation of blood in the left side of the fetal heart is approximately 10% higher than the right due to a remarkable streaming mechanism where oxygenated blood returning from the placenta is preferentially directed across the foramen ovale via the left liver and ductus venosus. This is presumably to ensure a reliable source of oxygen to the developing brain and coronary circulation. The less well-oxygenated blood returning from the SVC and lower body is preferentially routed towards the tricuspid valve and then on to the ductus arteriosus and pulmonary circulation. As pulmonary vascular resistance in the third trimester is inversely proportional to the oxygen content of the blood in the pulmonary arteries, a high pulmonary vascular resistance is maintained in the fetal lamb. Pulmonary vascular resistance is also high in the human fetus, although there is higher pulmonary blood flow compared with lambs [7]. There is also higher flow in the SVC in the human, likely reflecting the larger brain size, and lower flow in the umbilical vein, probably made possible by the higher hematocrit present in human fetuses. In fetal lambs exposed to chronic hypoxia there is an adaptive response where a 20% increase in hematocrit increases the oxygen carrying capacity of fetal blood [4]. Interestingly, T2 is inversely proportional to hematocrit, so that chronic hypoxia may result in a further reduction in the T2 of blood resulting from polycythemia [28].

The term 'brain-sparing' refers to an important mechanism in fetal circulatory physiology. This acute response to fetal hypoxia has been well studied in animal models and observed in human fetuses and is characterized by a reduction in the vascular resistance of cerebral and coronary vessels and increase in peripheral and pulmonary vascular resistance [1]. The result is a dramatic increase in cerebral and coronary blood flow, so that oxygen delivery to the brain and heart is maintained despite a fall in the oxygen content of the blood supplied to those organs. We have noted SVC flows greater than 250 ml/min/kg, or 50% of the CVO in fetuses with antenatal and postnatal evidence of placental insufficiency [29].

Limitations of this work include the absence of any attempt as yet to validate this T2 mapping technique for fetal blood in fetal vessels and our current dependence on an estimation of fetal hematocrit. Fetal hemoglobin may differ from adult hemoglobin in terms of its magnetic properties, and the small size of the fetal vessels of interest may render our T2 measurements subject to partial volume artifacts. With further investigation and a larger sample size we aim to gain a better understanding of these factors and show that oximetry can be successfully combined with the more established flow quantification.

Conclusion

We have speculated about the clinical significance of our preliminary observations regarding the distribution of flow in fetuses with CHD and IUGR [26, 30, 29], and hope that with more experience and development, fetal CMR may gain acceptance amongst clinicians as an additional tool to help guide obstetric management in these and other fetal conditions.

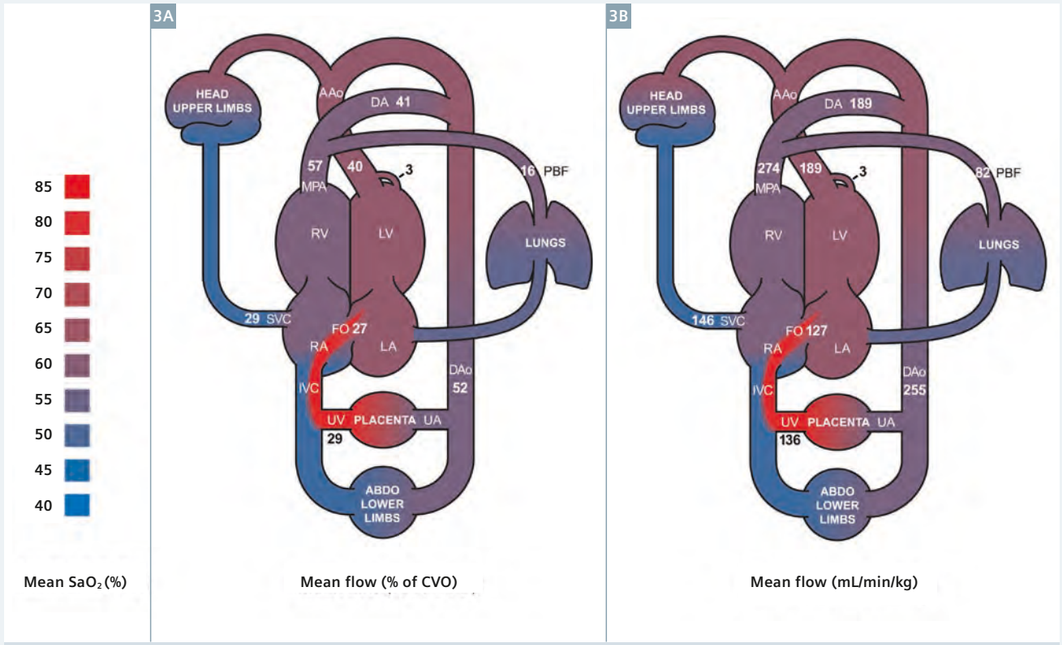

3 Mean flows and oxygen saturations in the late gestation human fetus by MRI. Flows as % of the combined ventricular output **(3A)** and in ml/min/kg **(3B)**.
AAo: ascending aorta, **DA**: ductus arteriosus, **MPA**: main pulmonary artery, **RV**: right ventricle, **LV**: left ventricle, **SVC**: superior vena cava, **FO**: foramen ovale, **LA**: left atrium, **PBF**: pulmonary blood flow, **RA**: right atrium, **UV**: umbilical vein, **UA**: umbilical vein, **DAo**: descending aorta.

References

1 Cardiovascular responses to hypoxemia and acidemia in fetal lambs. Cohn, HE, et al. 1974, Am J Obstet Gynecol, Vol. 120, pp. 817-824.
2 Doppler ultrasound assessment of cerebral blood flow in the human fetus. Wladimiroff, JW, Tonge, HM and Stewart, PA. 1986, BJOG: An International Journal of Obstetrics and Gynecology, Vol. 93, pp. 471-475.
3 Hypoxic regulation of the fetal cerebral circulation. Pearce, W. 2006, Vol. 100, pp. 731-738.
4 Metabolic and Circulatory Adaptations to Chronic Hypoxia in the Fetus. Richardson, BS and Bocking, AD. 3, 1998, Comparative Biochemistry and Physiology, Vol. 119A, pp. 717-723.
5 Neurodevelopment following fetal growth restriction and its relationship with antepartum parameters of placental dysfunction. Baschat, AA. 2011, Ultrasound Obstet Gynecol, Vol. 37, pp. 501-514.
6 Longitudinal changes in uterine, umbilical and fetal cerebral Doppler indices in late-onset small-for-gestational age fetuses. Oros, D, et al. 2, 2011, Ultrasound in Obstetrics & Gynecology, Vol. 37, pp. 191-195.

7 Rudolph, AM. Congenital Diseases of the Heart: Clinical-Physiological Considerations. 3rd. Chichester : Wiley Blackwell, 2001.

8 Oxygen uptake of the human fetus at term. Acharya, G and Sitras, V. 2009, Acta Obstetricia et Gynecologica, Vol. 88, pp. 104-109.

9 Measurement of blood flow by ultrasound: accuracy and sources of error. Gill, RW. 1985, Ultrasound Med Bio, Vol. 7, pp. 625-42.

10 Cardiovascular Flow Measurement with Phase-Contrast MR Imaging: Basic Facts and Implementation. Lotz, J, et al. 2002, Radiographics, Vol. 22, pp. 651-671.

11 Estimating Oxygen Saturation of Blood in Vivo with MR Imaging at 1.5T. Wright, GA, Hu, BS and Macovski, A. 3, 1991, Journal of Magnetic Resonance Imaging, Vol. 1, pp. 275-283.

12 In vivo MRI measurement of blood oxygen saturation in children with congenital heart disease. Nield, LE, Xiu-Ling, LQ and Valsangiacomo, ER. 2005, Pediatr Radiol, Vol. 35, pp. 179-185.

13 Self-gating MR imaging of the fetal heart: comparison with real cardiac triggering. Yamamura, J, et al. 2011, Eur Radiol, Vol. 21, pp. 142-149.

14 Cardiac MRI of the fetal heart using a novel triggering method: Initial results in an animal model. Yamamura, J, et al. 2012, Journal of Magnetic Resonance Imaging, Vol. 35, pp. 1071-1076.

15 Metric Optimized Gating for Fetal Cardiac MRI. Jansz, M, Seed, M and van Amerom, JVP. 2010, Magn Reson Med, Vol. 64, pp. 1304-1314.

16 Feasibility of quantification of the distribution of blood flow in the normal human fetal circulation using CMR: a cross-sectional study. Seed, M, et al. 2012, J Cardiovasc Magn Reson, Vol. 14, p. 79.

17 Dynamic imaging of the fetal heart using metric optimized gating. Roy, CW, et al. 2013, Magn Reson Med, Vol. epub.

18 T2 quantification for improved detection of myocardial edema. Giri, S, et al. 11, 2009, Journal of Cardiovascular Magnetic Resonance, p. 56.

19 Myocardial T2 mapping with respiratory navigator and automatic nonrigid motion correction. Giri, S, et al. 5, 2012, Vol. 68, pp. 1570-1578.

20 ACR Guidance Document on MR Safe Practices: 2013. Expert panel on MR Safety. 2013, Journal of Magnetic Resonance Imaging, Vol. 37, pp. 501-530.

21 Gowland, P. Safety of Fetal MRI Scanning. [ed.] D Prayer. Fetal MRI. Berlin Heidelberg: Springer-Verlag, 2011, pp. 49-54.

22 Blood Relaxation Properties at 3T – Effects of Blood Oxygen Saturation. Lee, T, et al. 2003. Proc.Intl.Soc.Mag.Reson.Med.11.

23 Partial volume effects on vascular T2 measurements. Stainsby, JA and Wright, GA. 3, 2005, Magnetic Resonance in Medicine, Vol. 40, pp. 494-499.

24 Changes in human fetal oxygenation during maternal hyperoxia as estimated by BOLD MRI. Sorensen, A, et al. 2013, Prenatal Diagnosis, Vol. 33, pp. 141-145.

25 Fetal weight estimation by echo-planar magnetic resonance imaging. Baker, P, Johnson, I and Gowland, P. 1994, Lancet, Vol. 343, pp. 644-5.

26 Fetal circulation in left-sided congenital heart disease measured by cardiovascular magnetic resonance: a case-control study. Al Nafisi, B, et al. 2013, J Cardiovasc Magn Reson. In Press.

27 Fetal haemoglobin measurement in the assessment of red cell isoimmunisation. Nicolaides, KH, et al. 1988, The Lancet, Vol. 331, pp. 1073-1075.

28 Magnetic relaxation in blood and blood clots. Bryant, RG, et al. 1, s.l.: 1990, 1990, Magn Reson Med, Vol. 13, pp. 133-44.

29 Assessment of late-onset fetal growth restriction by phase contrast MR. van Amerom, JFP, et al. Salt Lake City: s.n., 2013. ISMRM. Vol. Abstract 5928.

30 MRI shows limited mixing between systemic and pulmonary circulations in fetal transposition of the great arteries – a potential cause of in utero pulmonary vascular disease. Porayette, P, et al. 2014. Pediatric Radiology.

*Siemens disclaimer: MR scanning has not been established as safe for imaging fetuses and infants less than two years of age. The responsible physician must evaluate the benefits of the MR examination compared to those of other imaging procedures.

**WIP, the product is currently under development and is not for sale in the US and other countries. Its future availability cannot be ensured.

Christopher K. Macgowan

Mike Seed

Contact

Mike Seed MBBS, MRCPCH, FRCR
Division of Cardiology
Hospital for Sick Children
555 University Avenue
Toronto, Ontario M5G 1X8
Canada
mike.seed@sickkids.ca

http://www.sickkids.ca/Research/fetalMRI/index.html

The entire editorial staff at Monash Medical Centre and at Siemens Healthcare extends their appreciation to all the radiologists, technologists, physicists, experts and scholars who donate their time and energy – without payment – in order to share their expertise with the readers of MAGNETOM Flash.

MAGNETOM Flash – Imprint

Publisher:
Siemens AG
Medical Solutions
Business Unit Magnetic Resonance,
Karl-Schall-Straße 6, D-91052 Erlangen,
Germany

Guest Editor:
Professor Michael Ditchfield, M.D.
Professor and Head of Paediatric Imaging
Monash Children's and Monash University,
Clayton, Australia

Editor-in-chief: Antje Hellwich
(antje.hellwich@siemens.com)

Editorial Board: Wellesley Were;
Ralph Strecker; Sven Zühlsdorff, Ph.D.;
Gary R. McNeal, MS (BME);
Peter Kreisler, Ph.D.

Production: Norbert Moser, Siemens AG,
Medical Solutions

Layout: independent Medien-Design
Widenmayerstrasse 16, D-80538 Munich,
Germany

Printer: G. Peschke Druckerei GmbH,
Schatzbogen 35, D-81829 Munich,
Germany

We welcome your questions and comments about the editorial content of MAGNETOM Flash. Please contact us at magnetomworld.med@siemens.com.

Manuscripts as well as suggestions, proposals and information are always welcome; they are carefully examined and submitted to the editorial board for attention. MAGNETOM Flash is not responsible for loss, damage, or any other injury to unsolicited manuscripts or other materials. We reserve the right to edit for clarity, accuracy, and space. Include your name, address, and phone number and send to the editors, address above.

MAGNETOM Flash is also available on the internet:

www.siemens.com/magnetom-world

On account of certain regional limitations of sales rights and service availability, we cannot guarantee that all products included in this brochure are available through the Siemens sales organization worldwide. Availability and packaging may vary by country and is subject to change without prior notice. Some/All of the features and products described herein may not be available in the United States.

The information in this document contains general technical descriptions of specifications and options as well as standard and optional features which do not always have to be present in individual cases, and which may not be commercially available in all countries. Due to regulatory reasons their future availability cannot be guaranteed. Please contact your local Siemens organization for further details.

Siemens reserves the right to modify the design, packaging, specifications, and options described herein without prior notice.
Please contact your local Siemens sales representative for the most current information.

Note: Any technical data contained in this document may vary within defined tolerances. Original images always lose a certain amount of detail when reproduced.

Not for distribution in the US

Global Business Unit

Siemens AG
Medical Solutions
Magnetic Resonance
Henkestraße 127
DE-91052 Erlangen
Germany
Phone: +49 9131 84-0
www.siemens.com/healthcare

Local Contact Information

Asia/Pacific:
Siemens Medical Solutions
Asia Pacific Headquarters
The Siemens Center
60 MacPherson Road
Singapore 348615
Phone: +65 6490 6000

Canada:
Siemens Canada Limited
Healthcare Sector
1550 Appleby Lane
Burlington, ON L7L 6X7, Canada
Phone +1 905 315-6868

Europe/Africa/Middle East:
Siemens AG, Healthcare Sector
Henkestr. 127
91052 Erlangen, Germany
Phone: +49 9131 84-0

Latin America:
Siemens S.A., Medical Solutions
Avenida de Pte. Julio A. Roca No 516, Piso
C1067 ABN Buenos Aires, Argentina
Phone: +54 11 4340-8400

USA:
Siemens Medical Solutions USA, Inc.
51 Valley Stream Parkway
Malvern, PA 19355-1406, USA
Phone: +1 888 826-9702

Global Siemens Headquarters

Siemens AG
Wittelsbacherplatz 2
80333 Muenchen
Germany

Global Siemens Healthcare Headquarters

Siemens AG
Healthcare Sector
Henkestraße 127
91052 Erlangen
Germany
Phone: +49 9131 84-0
www.siemens.com/healthcare

Order No. A91MR-1000-107C-7600 | Printed in Germany | CC MR 1966 041420. |

www.siemens.com/magnetom-world